

**Fuel Efficient Balance of Plant and Power Split
Control Strategies for Fuel Cell Vehicles**

by

Miriam A. Figueroa-Santos

A dissertation submitted in partial fulfillment
of the requirements for the degree of
Doctor of Philosophy
(Mechanical Engineering)
in the University of Michigan
2021

Doctoral Committee:

Associate Research Scientist Jason B. Siegel, Co-chair
Professor Anna G. Stefanopoulou, Co-Chair
Professor James Freudenberg
Assistant Professor Youngki Kim
Dr. Denise M. Rizzo, US Army CCDC

Miriam A. Figueroa-Santos

miriamaf@umich.edu

ORCID iD: 0000-0001-5553-6652

© Miriam A. Figueroa-Santos 2021

DEDICATION

To my friends and family for all their love and support. To my grandfather Victor M. Santos and Ruben R. Franco for always believing I can accomplish anything.

ACKNOWLEDGMENTS

The work presented in this dissertation would not have been possible without various people's guidance and support. First, I would like to thank the committee chair, Prof. Anna G. Stefanopoulou, for all the love, advice, help, and mentoring throughout my studies. Secondly, I would like to thank committee co-chair Dr. Jason Siegel for his constant guidance, advice, help, and support. I want to thank the committee member, Prof. Youngki Kim, for his mentoring and guidance. I also want to thank the committee member, Dr. Denise Rizzo, for her mentoring. Finally, I would like to thank the committee member Prof. James Freudenberg for his teachings and advice.

I will also like to thank Katerina Freudenberg for all the love and support throughout my difficult times. I want to thank my labmates at the Powertrain Control Laboratory (PCL): Shima Nazari, Shankar Mohan, Hector Perez, Niket Prakash, Bryan Maldonado, Mitchell Bieniek, Di Chen, Suhak Lee, Tomas Poloni, Peyman Mohtat, Saravanan Durairasan, Chunan Huang, Sravan Pan-nala, Vivian Tran, Valentin Sulzer, Andrew Weng, Omar Ahmed, Eunjeong Hyeon, and Joe Drallmeier for all the guidance and moral support. I will also like to thank the faculty, staff, and students from the Walter E. Lay Automotive Engineering Laboratory for the beautiful memories and experiences during lunchtime.

I would also like to thank the Mechanical Engineering Department at the University of Michigan, the National Science Foundation Graduate Research Fellowship Program, the Automotive Research Center, and the Science, Mathematics, and Research for Transformation Scholarship for funding this work. I want to thank the people at Ground Vehicle Systems Center for teaching me the different methodologies and systems used there.

Last but not least, I will like to thank my friends Fanny Pinto, Valentina Vil-lasmil, Angela Wu, Kenny Lai, Ahmet Mazacioglu, Giancarlo Reyes, Francia Rugamas, and others for their constant love and support throughout this chapter in my life. I will also like to thank my parents, David Figueroa and Maria Santos, my sister Isaura Figueroa, and the rest of the family that has supported me throughout this experience.

TABLE OF CONTENTS

DEDICATION	ii
ACKNOWLEDGMENTS	iii
LIST OF FIGURES	vii
LIST OF TABLES	x
ABSTRACT	xii
CHAPTER	
1 Introduction	1
1.1 Background	1
1.2 Fuel Cell Vehicle	4
1.3 Fuel Cell Operation	6
1.4 Balance of Plant (BOP)	8
1.5 Power Split	10
1.5.1 Rule-based Control (RBC) Strategies	11
1.5.2 Dynamic Programming (DP)	12
1.5.3 Pontryagin’s Minimum Principle (PMP)	13
1.5.4 Equivalent Consumption Minimization Strategy (ECMS)	13
1.5.5 Model Predictive Control (MPC)	14
1.5.6 Machine Learning	15
1.6 Battery Sizing and Lithium Ion Battery Chemistries	15
1.7 Thesis Organization and Contributions	15
2 Fuel Cell System Modeling	19
2.1 Introduction	19
2.2 0-D Semi-empirical Liquid-cooled Stack Fuel Cell Model	21
2.2.1 Fuel Cell Voltage Subsystem	21
2.2.2 Membrane Hydration Subsystem	23
2.2.3 Cathode Subsystem	25
2.2.4 Anode Subsystem	27
2.3 Empirical Fit for Liquid-cooled Stack Voltage Subsystem	28
2.4 Balance of Plant (BOP) Components and Fuel Cell Net Efficiency for Liquid-cooled Fuel Cell	29
2.4.1 Balance of Plant (BOP) Component for Liquid-cooled Fuel Cell	29

2.4.2	Fuel Cell Net Efficiency for the Liquid-cooled Stack	31
2.5	Air-cooled and Liquid-cooled Fuel Cell Behavior	32
2.6	Empirical Model for Air-cooled Stack	32
2.7	Conclusion	34
3	Thermal Control Loop in an Air-cooled FC Powered Robot	36
3.1	Introduction	36
3.2	Fuel Cell Vehicle Model for Hybrid Electric Vehicle	37
3.2.1	Battery Model Parameterized for the Packbot	38
3.2.2	Air-cooled Fuel Cell System	39
3.3	Optimal Power-split Problem	42
3.4	Reference-based Control Strategy	44
3.5	Results	45
3.6	Conclusion	48
4	Sizing Effect on Power Split of Medium-size Fuel-cell Military Vehicle	49
4.1	Simulation Models	50
4.1.1	Vehicle and Motor Model	52
4.1.2	Battery Models for NMC and LFP Chemistry	54
4.1.3	Fuel Cell Parameters for Liquid Cooled Operation	56
4.2	Dynamic Programming (DP) Formulation	58
4.3	Equivalent Consumption Minimization Strategy	59
4.4	DP and ECMS Performance Comparison	60
4.5	Battery Sizing Analysis Results with NMC	62
4.6	Battery Sizing Comparison between NMC and LFP	65
4.7	Conclusion	66
5	Co-optimization of Speed Trajectory and Power Management for a Fuel-cell/Battery Electric Vehicle	68
5.1	Introduction	68
5.2	Vehicle and Powertrain Model	70
5.2.1	Point-mass Longitudinal Dynamics	71
5.2.2	Lumped Efficiency Parameters for Fuel Cell System	71
5.2.3	Battery Model	72
5.2.4	Motor Model	72
5.3	Optimal Control Problem Formulation	73
5.3.1	System Dynamics	73
5.3.2	Simplification of Control Modes	74
5.3.3	Co-optimization	78
5.3.4	Sequential Optimization	80
5.4	Case Study - Lightweight Military Ground Robot	81
5.4.1	Optimization Set-up	82
5.4.2	Optimization Results	84
5.5	Conclusion	91
6	State of Charge Estimation for LFP Chemistry Cells	92

6.1	Introduction	92
6.2	Experimental Setup and Force Behavior	95
6.3	Simulation Model	98
6.3.1	Cell Swelling Force Model (F-SOC)	98
6.3.2	Terminal Voltage Model (OCV-SOC)	100
6.4	Voltage Model Parameterization	101
6.5	SOC Estimation Model	102
6.5.1	Voltage Only Observer Design	103
6.5.2	Voltage and Force Observer Design	103
6.5.3	SOC Estimation Error during Switching	105
6.5.4	Bias Influence in SOC Estimation	107
6.6	Simulation Results without Model Mismatch in F-SOC and OCV-SOC	108
6.7	Simulation Results with Inflection Point Mismatch in F-SOC and OCV-SOC	111
6.8	Experimental Data Results Using F-SOC and OCV-SOC	114
6.9	Conclusions	116
7	Conclusion and Future Work	118
7.1	Results and Conclusions	118
7.2	Future Work	120
	APPENDIX A Supplemental Material	122
A.1	Detailed Computation for DP Implementation	122
A.2	Voltage Hysteresis State H Function	123
A.3	Discrete Terminal Voltage Model	124
A.4	Force and OCV Function Values That Represent Average Data	125
	BIBLIOGRAPHY	126

LIST OF FIGURES

FIGURE

1.1	Fuel cell vehicle (FCV) in the transportation sector	2
1.2	Fuel cell (FC), lithium-nickel-manganese-cobalt-oxide (NMC), and lithium ion iron phosphate (LFP) specific energy and power comparison	3
1.3	Example of a fuel cell hybrid vehicle powertrain	5
1.4	Toyota Mirai fuel cell system implemented since 2015	7
1.5	Schematic of simple proportional-integral control implementation.	12
1.6	Dynamic programming (DP) and Pontryagin’s Minimum Principle (PMP) schematic .	14
1.7	Summary of the different military vehicles with the corresponding components analyzed for this thesis	16
2.1	Length scales and computational domains for PEMFC modeling	20
2.2	Impact of the fuel cell temperature, relative humidity and operating pressure on fuel cell polarization curve	22
2.3	15kW Hydrogenics HD 15 liquid-cooled fuel cell stack	29
2.4	15kW Hydrogenics HD 15 stack polarization curve data compared to fuel cell voltage subsystem model.	30
2.5	10 kW Aeristech data and compressor model fit.	31
2.6	Static efficiency curve for two 15kW Hydrogenics stacks.	31
2.7	Ballard 1200 ACS air-cooled fuel cell stack	33
2.8	The fuel cell polarization curve and power under different temperatures for Ballard 1020 ACS air-cooled fuel cell	34
3.1	Packbot robot powered by a Ballard 1200 ACS air-cooled fuel cell and lithium-ion battery pack.	38
3.2	The steady state fuel cell polarization, power, and system net power for different temperatures for Ballard 1020 ACS air-cooled FC	41
3.3	Schematic of the optimal coordination of the FC/battery power split and the thermal/cooling system	42
3.4	Block diagram of the reference-based FC/battery power-split and the thermal/cooling system	44
3.5	Comparison of fuel cell power and efficiency between the results obtained with offline optimal control strategy and the two PI controllers for the two terrain cases considered in this study (flat pea gravel terrain 3.5a, and hill terrain 3.5b).	46
3.6	Comparison of fuel cell current, airflow, SOC, and fuel cell temperature results from offline optimal control strategy and the two PI controllers for the flat pea gravel and hill terrain case considered in this study.	47

4.1	Speed and grade profile from the highway driving and hilly terrain cycle that will be used for the power split analysis of the medium-size vehicle.	51
4.2	Power from silent watch profile that will be used for the power split analysis of the medium-size vehicle	52
4.3	Motor UQM HD220 Efficiency Map used to obtain our load profile.	54
4.4	The open-circuit voltage and internal resistance of the battery as a function of battery SOC.	55
4.5	Voltage or polarization curve at $65^{\circ}C$ used for our fuel cell system analysis.	56
4.6	Dynamic Programming formulation for medium size military vehicle	59
4.7	Lookup table of fuel cell current as a function of equivalence factor and load power obtained from the equivalence factor minimization strategy.	60
4.8	Battery size comparison for Hilly terrain drive cycle.	62
4.9	Hydrogen consumption comparison for Hilly terrain drive cycle.	64
5.1	A simple schematic of a fuel-cell/battery powered electric vehicle.	70
5.2	The static efficiency of the fuel-cell system	72
5.3	Elevation and grade of the considered driving environment	83
5.4	Comparison of energy consumption obtained by co-optimization and sequential optimization for various times traveled on Churchville-B road	85
5.5	Histograms of normalized occurrence of powertrain operation obtained by co-optimization and sequential optimization on Churchville-B road for two drive cycles	86
5.6	Comparison of vehicle and powertrain operation obtained by co-optimization and sequential optimization over Churchville-B road for travel times of 329 and 795 seconds	87
5.7	Comparison of energy consumption obtained by co-optimization and sequential optimization for various times traveled on Convoy road	88
5.8	Histograms of normalized occurrence of powertrain operation obtained by co-optimization and sequential optimization on the Convoy cycle for two driving times	89
5.9	Comparison of vehicle and powertrain operation obtained by co-optimization and sequential optimization over the Convoy cycle for travel times of 1259 and 2579 seconds	90
6.1	Measured voltage and force for the 20 Ah A123 lithium ion iron phosphate battery cycled under low current rate $C/20$	93
6.2	Drift in the force sensor can be observed by comparing the force vs. SOC for two $\frac{C}{20}$ cycles which were conducted two months apart with three cycles done in between them with the same battery.	96
6.3	A piecewise linear approximation of the (a) open circuit voltage and (b) cell swelling force was fit to the experimental measured values for the A123 Lithium Iron Phosphate Battery Cell.	97
6.4	Comparison of open loop simulation model results (denoted by the color orange) and experimental measurement of voltage, temperature, force, and SOC obtained from the 20 Ah battery during the Dynamic Stress Test (DST) inside an environmentally controlled chamber set at $25^{\circ}C$ ambient conditions.	99
6.5	Simulation (without bias in the force measurement) for the Switch Observer V&F developed in our previous work [119].	106

6.6	Simulation assuming accurate modeling using Switch Observer V&F Bias observer with an emulated bias of 3 N and 10 % (0.1) initial SOC error.	109
6.7	Simulation of the impact of model mismatch in the inflection points of the force vs. SOC curve.	112
6.8	Experimental validation of the developed observer (Switch Observer V&F Bias) with 10% (0.1) initial SOC error.	115

LIST OF TABLES

TABLE

1.1	Different electric vehicles (EV) charges comparison	2
2.1	Identified parameters for one cell voltage model from the 15kW Hydrogenics HD 15 stack.	29
3.1	Hydrogen Consumption & Root Mean Square Error (RMSE)	45
3.2	PI controller Gains	48
4.1	Medium size military vehicle performance requirements.	50
4.2	Medium size military vehicle specifications.	50
4.3	Vehicle and motor model parameters for medium size military vehicle.	53
4.4	Discretization of optimization variables in Dynamic Programming	59
4.5	Chosen equivalence factors for the three drive cycles	60
4.6	DP and ECMS performance comparison for all drive cycles	61
4.7	Battery Size Comparison for Hilly terrain drive cycle with NMC	65
4.8	Battery Size Comparison for Hilly terrain drive cycle	66
5.1	Possible Control Actions.	78
5.2	Vehicle parameters and constraints.	82
5.3	Discretization of optimization variables in Dynamic Programming.	83
5.4	Average computation time.	84
6.1	Battery Equivalent Circuit Parameters and its values.	101
6.2	Control weights for the different sensors using the simulated data.	108
6.3	Comparison of the RMSE index for different initial estimate error and different sensors using the simulated data.	111
6.4	Estimation Weights for the different sensors using the simulated data with and without model mismatch.	113
6.5	Comparison of the RMSE index for different initial estimate error and different sensors using the simulated data with and without model mismatch.	114
6.6	Control Weights for the different sensors for data validation: V_t , terminal voltage; V & F Bias, fusion of both sensors.	114
6.7	Comparison of the RMSE index for different initial estimate error and different sensors for data validation.	116
A.1	Voltage hysteresis state H function parameters and its values.	123

A.2	Parameter values for the PWL OCV–SOC function in Equation (A.3) without model mismatch.	125
A.3	Parameter values for the OCV–SOC function in Equation (6.7).	125
A.4	Parameter values for the F–SOC function that represent average data.	125

ABSTRACT

Fuel cell (FC) systems with on-board hydrogen storage offer long range, fast refueling, with low audible and thermal signatures. These attributes make fuel cell vehicles (FCVs) the best option for fleet vehicles with high utilization and stringent environmental requirements. A FC system consists of the stack, which performs the electrical conversion of hydrogen to electricity, the balance of plant (BOP) components including pumps, ejectors, and blowers which are responsible for supplying reactants (hydrogen and air) at the correct rates, humidification, and thermal management hardware. Fuel cells (FCs) are typically hybridized with a battery to recuperate the braking energy and improve the system durability by reducing the a) transient and high current spikes, b) idling conditions with high open circuit potential, and c) the number of startup and shutdown cycles. At the vehicle level satisfying driver's torque/power demand is achieved by choosing the power split between the fuel cell and battery. Low hydrogen consumption and vehicle efficiency can be achieved through load preview and simultaneous optimization of vehicle speed and power split to regulate battery state of charge and fuel cell thermal management as this thesis shows.

This dissertation presents control strategies to address the above challenges for different size and weight of fuel cell vehicles motivated by the diversity of powertrains managed in the defense industry. Air-cooled stacks are considered for small power systems such as ground robots. To this end, an air-cooled fuel cell system model with a fan as a BOP component is considered. The optimization of the lumped thermal dynamic addresses the FC bulk temperature taking into account the parasitic loss of the electric fan that supplies air for the reaction and cooling simultaneously. We analyze prior work that used an offline numerical optimization method called General Purpose Optimal Control Software (GPOPS) to solve the optimal fan flow and fuel cell current for this combined BOP and powersplit optimization strategy. We show that the optimal FC temperature and current setpoints depend on the drive cycle, but their values does not change substantially within the cycle. Given the intra-cycle invariance of the setpoints, we develop two proportional-integral (PI) controllers to achieve the power split and the BOP.

Secondly, a large fuel cell vehicle (FCV) with multiple kW of power uses a liquid cooling hardware strategy and imposes low parasitic losses hence the optimization emphasis shifts on the power split strategy. A dynamic programming and equivalent minimization consumption control strategies are developed and compared for different battery sizes and battery cell chemistries.

Thirdly, co-optimization and sequential optimization of the velocity profile and the power split

were compared and developed for a liquid-cooled FC with battery for a Small Multipurpose Equipment Transport (SMET) vehicle in terms of energy consumption, operating modes, and computational cost. Last but not least, the importance of accurate SOC estimation for the battery utilization is addressed by combining voltage and force measurements to improve SOC estimation for an efficient, scalable, and safe fuel cell vehicle system.

CHAPTER 1

Introduction

1.1 Background

Alternatives to the traditional internal combustion engine (ICE) are required to decarbonize the transportation, which accounts for almost 30% of all greenhouse gas emissions in the United States of America (USA) [145] and nearly 20% in the rest of the world. Fuel cell vehicles (FCVs) are examples of such alternatives to the internal combustion engine vehicles. Fuel cells (FCs) convert chemical energy contained in hydrogen into electricity. Fuel cell (FC) achieve the range and recharge convenience of ICEs. If combined with batteries they provide the power and agility of standalone batteries [109]. Widespread adoption of FCVs is limited due to the lack of hydrogen distribution and refueling infrastructure and associated high cost. Despite the low volumetric energy density of compressed hydrogen storage on-board the vehicle various systems have demonstrated a range of 500 miles [128, 129]. Hydrogen is currently produced mostly by natural gas that is plentiful in the USA, but it also produces emissions (kgCO_2/kWh). The decarbonization of the grid makes electrolysis the greener means of hydrogen production. If all petrol cars in the USA, however, were replaced by fuel cell vehicles, an estimated 1.4 to 2.1 TW would be required to produce the needed hydrogen from intermittent renewables. This is far greater than the current total USA electricity generating capacity of 1.2 TW [21] requiring integration of solar and wind power generation and upgraded grid transmission and control that will allow control of the electrolysis demand.

The current state of the art for light-duty fuel cell vehicles is the Toyota Mirai, Honda Clarity, and the Hyundai Nexo. They each have a range of 350 miles and can be refueled in 3-5 minutes [60]. A popular alternative vehicle configuration that will rely on renewable electric energy generation is the battery electric vehicle (BEV). Examples of the state of the art for battery electric vehicles (BEVs) are currently the Tesla Model 3 and S, Nissan Leaf, GM Bolt, among others, which have a range of 100-351 miles [56] and recharge depends on the type of charger as shown in Table 1.1 and obtained from [70] and [165]. The limitations of BEVs compared to FCVs is

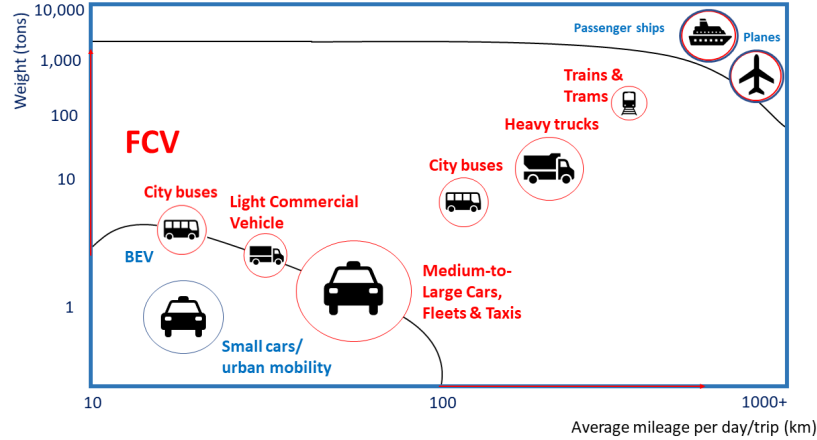


Figure 1.1: Fuel cell vehicle (FCV) in the transportation sector. Figure adapted from [29]. Circle size represents the relative annual energy consumption of this vehicle type.

Table 1.1: Different electric vehicles (EV) charges comparison. Information obtained from [70] and [165].

Charger	Standard type	AC/DC	Charging time	BEV Power
Tesla	Type 3	DC	20 min	50-100 kW
Mennekes	Type 2	AC	13 hours	4-19.2 kW
J1772	Type 1	AC	35 hours	1.4-1.9 kW

their longer charging time and shorter mileage range, but they have lower cost and their fuel infrastructure has been better established [129]. As Fig. 1.1 summarizes, most of the small cars will be BEVs, except robotic or autonomous vehicles that can and should operate with much higher utilization to become cost-effective, requiring multiple fast re-fueling events per day [60]. Applications such as shared-services, taxis, buses, among others, can benefit by using fuel cells because they operate 24/7 and there is no time to recharge. Medium-duty vehicles (MDV) that operate continuously and in a fleet configuration with depot refueling would also benefit from transitioning to FC powertrains.

While fuel cell light-duty vehicles (LDVs) are commercially produced (though not with extensive success), the development of heavy-duty fuel cell vehicles in long-haul trucks is accelerating. The United States Department of Energy (DOE) in their efforts to implement FCVs, determined a target of \$60/kW, a power density of 1.7 KWh/L, and a durability target 30,000 hours for heavy-duty vehicles [60] which are the current focus for most USA R&D efforts.

One of the factors affecting the overall cost of the fuel cell vehicle are the durability and cost of the fuel cell system [60]. The fuel cell system's durability and cost can be improved by optimizing the balance of plant (BOP) components such as air compressors, fuel processors, sensors,

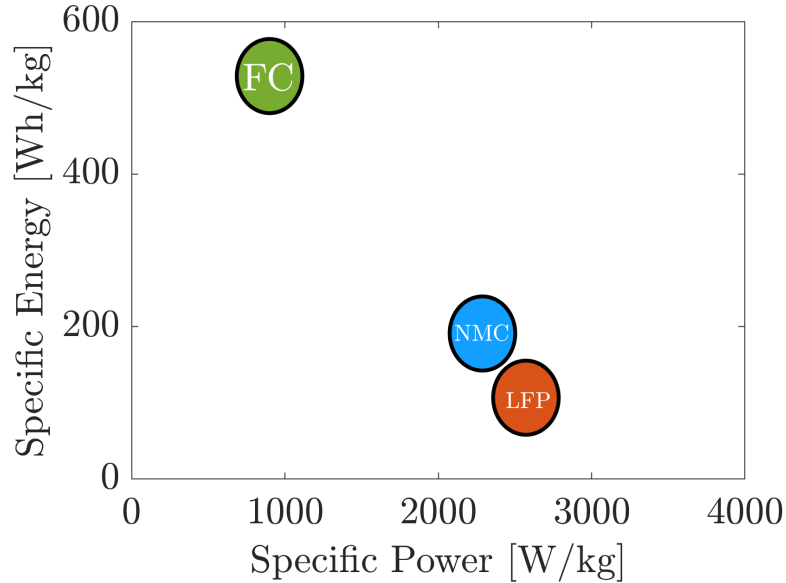


Figure 1.2: Fuel cell (FC), lithium-nickel-manganese-cobalt-oxide (NMC), and lithium ion iron phosphate (LFP) specific energy and power comparison. Fuel cell information obtained from [146] and NMC and LFP information obtained from [106].

and water and heat management that affect fuel cell performance. Great progress has been made toward achieving the Department of Energy’s (DOEs) targets for reduction in stack component cost, including reducing the Pt in the catalyst. However, this attention has not been directed toward the balance of plant components, which is projected to reach 60% of the total cost by 2025 [61]. Therefore, optimal control of the power split sizing of the FC, battery, and the pumps, fans, and blowers would enable component downsizing and system simplification but require careful coordination to protect the fuel cell from overheating or reactant starvation.

A final aspect to consider when optimizing the fuel cell hybrid electric vehicle performance is the type of energy source the fuel cell should be combined with. Fuel cells are always connected with another energy source, as shown in Fig. 1.3, to meet stringent vehicle cold startup and transient response requirements and improve system durability [8]. Even though fuel cell degradation is mitigated by hybridization, hybridization affects the total cost of ownership [84] which limits the further implementation of fuel cell vehicles. Although fuel cell and batteries are the typical configuration, supercapacitor configurations for FCVs were investigated due to the high power density, fast transient response, longer life cycle, and high-frequency rate of charging and discharging [49]. A combination of the fuel cell, battery, and supercapacitor has also been proposed at a very high cost to take advantage of both good qualities of the two energy sources or support highly energetic equipment on-board vehicles. In this thesis, we focused on the FC and battery hybrid configuration following the commercial trends for small to medium-size vehicles.

Besides choosing the battery and fuel cell configuration, the question of which battery chemistry should be chosen to operate the fuel cell vehicles formulates. Among various cathode materials for lithium ion (Li-ion) batteries, two chemistries are widely used, namely, lithium-nickel-manganese-cobalt-oxide (NMC) and lithium ion iron phosphate (LFP). Especially, NMC has been considered a good candidate for electric vehicles (EV) applications for its high specific energy [82]. On the other hand, LFP has been considered for unmanned air vehicles (UAV), hybrid electric vehicles (HEV), EV and are promising for FCV owing to its fast charging capability, high power density, and long cycle life [178]. As shown in Fig.1.2, NMC has higher specific energy while LFP has higher specific power. Therefore, the question of which chemistries to use in fuel cell vehicles (eg., LFP or NMC) arises and needs to be answered.

1.2 Fuel Cell Vehicle

An example of a fuel cell vehicle (FCV) powertrain is shown in Fig. 1.3, highlighting at the top the power splitting and energy management between a battery and the fuel cell. The dynamic response of the fuel cell (FC) and its ability to follow the load required to power a vehicle depends on managing the air and hydrogen paths that supply the reactants along with the thermal and humidification requirements. This management is denoted as balance of plant (BOP) and has been the subject of numerous publications. Textbook material with publicly-available simulation [120] and commercial software can be found in [3]. Past control investigations focused on avoiding starvation in the cathode and anode that lead to fuel cell degradation [126]. Combination of fuel cell with batteries can provide load-leveling and allows the system to operate at lower cathode stoichiometric ratios (lower reactant flows), thus reducing the parasitic losses associated with the air compressor [139] and the humidification of the air path, promoting self-balancing of the hydrogen system. Although the balance of plant has been addressed in the past, the influence of cooling and battery sizing during start-up, shutdown, and storage periods across a wide range of environmental conditions is still the frontier in the control and optimization efforts in FCVs.

The problem of how much power is required from the fuel cell and the battery is still relevant, especially, if the FC is used as the battery range extender. This power split has to maintain the efficient operation of its components from driving from point A to point B and ideally deplete its battery or the hydrogen storage depending on the availability of electricity or hydrogen supply at points. In commercial range extenders or plug-in hybrids with internal combustion engines the preference is to deplete the battery due to the cost of electricity and the high environmental burden of fossil fuel combustion. In this thesis, the power split is formulated with a terminal depleted battery, but we may explore the depleted hydrogen option later as a case study.

The torque demand is known as the load profile and depends on the vehicle velocity trajectory,

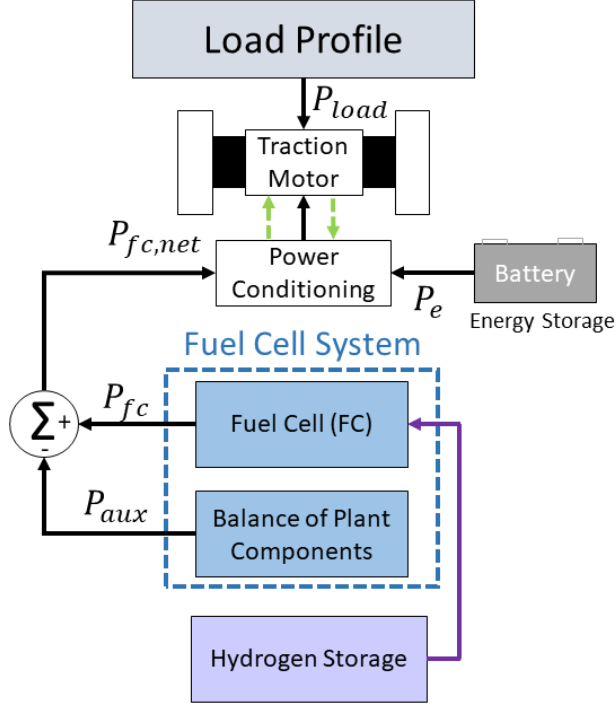


Figure 1.3: Example of a fuel cell hybrid vehicle powertrain. Figure based on [120].

as shown in Fig. 1.3. The load profile is converted to electrical power through the motor (P_{load}). Then, the power split of the battery power and fuel cell for an FCV is determined by:

$$P_{fc,net} = P_{load} - P_e \quad (1.1)$$

where P_e is the power required by other onboard energy sources such as batteries and $P_{fc,net} = P_{fc} - P_{aux}$ is the fuel cell's net stack power where P_{aux} is the power for the auxiliary components managing the BOP and P_{fc} is the fuel cell stack power. In the following section, the fuel cell's reactions that produce P_{fc} are explained. A schematic of how the power flow occurs in an FCV is shown in Fig. 1.3. Further terms can be added to this power split rule, such as DC/DC converter power, depending on the fuel cell vehicle configuration and components. The battery power is given by:

$$P_b = n_s n_p I_b V_t \quad (1.2)$$

where n_p is the number of battery cells in parallel in a module, n_s is the number of battery modules in series for forming a stack, I_b is the battery current, and V_t is the terminal voltage of a battery cell.

Another aspect that needs to be considered in the fuel cell vehicle is that the range of the

state of charge of the battery and size depends on whether the fuel cell vehicle is either a hybrid vehicle where the battery is used as load leveling for the FC or a plug-in hybrid vehicle where the battery is depleted and the FC is used as a range extender. A smaller battery is used for a hybrid car and the state of charge is usually controlled in a narrow range of 70-40%. The battery absorbs the fast transient and can be recharged through regenerative braking to improve the overall vehicle efficiency and FC durability. For this configuration the power battery is used as discussed in chapter 5. For a plug-in hybrid vehicle, a bigger battery is used or a FC range extender, and the battery is completely depleted by the end of the trip with the expectation that the battery can be charged overnight to minimize the hydrogen used. The range for the state of charge is 80-20% for the plug-in hybrid vehicle. In this chapter, most of the control strategies discussed are for fuel cell vehicles with a hybrid configuration.

Last but not least, fuel cell models need to be scalable to address military vehicles' needs. Military vehicles' power demand ranges from 300 W in robots to 250 kW in heavier vehicles. The military vehicles are required to operate at extreme environmental conditions that can affect fuel cell operation, such as startup from sub-zero temperatures and operation at dry ambient conditions. This thesis aims to develop a model of the polymer electrolyte membrane fuel cell (PEMFC) that accounts for the parasitic losses of the balance of plant to study the sizing effect on the fuel cell system performance combined with batteries to power the vehicle. The power-split for the fuel cell and battery for various vehicle sizes and drive cycles will be analyzed in this thesis to address if the fuel cell models' developed in this thesis fit the military vehicle operating conditions' needs.

1.3 Fuel Cell Operation

The fuel cell is composed of membrane separator and two electrodes. The anode is known as the electrode where hydrogen gas is provided and reacted in the fuel cell, and the cathode as the electrode that has oxygen flow through the fuel cell, as shown in Fig. 1.4. The separator is composed of a membrane, two catalyst layers, and two gas diffusion layers, as shown in Fig. 1.4. The catalyst layer could be a part of the electrode or membrane, depending on the manufacturing process. The multilayered assembly that consists of the two electrodes and the membrane is called the membrane electrode assembly (MEA) [122]. The MEA is between the collector or electrode plates. The primary reaction in the fuel cell is the hydrogen, which is fed through the anode, and it separates into protons and electrons in the catalyst layer [89]. The protons flow through the membrane until it reaches the cathode, and the electrons flow through the external circuit producing electricity. The electrons and protons react with the oxygen in the cathode, producing water, as

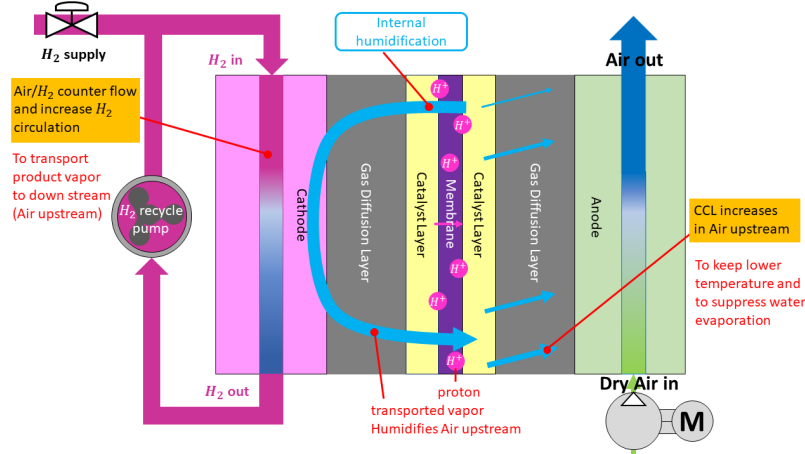


Figure 1.4: Toyota Mirai fuel cell system implemented since 2015. Figure reproduced from [166].

shown in Fig. 1.4. Therefore, the overall reaction occurring in the fuel cell is:



The overall chemical reaction produces heat, and heat transfer occurs within the fuel cell's solid components, reactant gases, and cooling medium. The heat produced affects the water transport within the catalyst layers, gas diffusion layers, membrane, and the fuel cell's overall performance. Therefore, heat removal is required to avoid the probable decrease in the overall performance by fuel cell degradation due to overheating [16]. To further understand the fuel cell reactions and the heat produced, the MEA components' properties and mutual interdependence are explained.

- Membrane → The membrane is responsible for the proton transport from the anode to the cathode. The membrane also does water transport from the cathode and anode. Therefore, the membrane should have high proton conductivity, be chemically and mechanically stable in the fuel cell environment, and provide a barrier for mixing fuel and reactant gases. The material typically used for the membrane consists of a fluorocarbon backbone to which sulfonic acid groups ($SO_3^- H^+$) are attached. The thickness of the membrane varies from 50 to 175 microns [122]. Thin membrane have low resistance but can degrade and have high crossover. Acceleration of membrane degradation occurs when high temperatures ($T_{fc} \in [85-120^\circ C]$) and low humidity ($\phi \in [30-10\%]$) values are present in the fuel cell [170]. Beyond the degradation, the high temperatures and low humidity values affect proton transport and water transport, causing a drop in the power or electricity produced by the fuel cell through either flooding or drying of the fuel cell.
- Catalyst Layer → The catalyst layer is responsible for the electrochemical reactions to take

place. The most common catalyst in proton-exchange membrane (PEM) fuel cells is platinum [89]. Higher temperature causes platinum dissolution and deposition in the membrane affecting the water transport [103].

- Gas Diffusion Layer (GDL) → The primary role for the GDL is to facilitate the gas transport from the channels to the catalyst layer. The gas diffusion layer is also responsible for conducting the heat generated by the electrochemical reactions in the catalyst layer to the collector or separator plates while providing mechanical support to the MEA. The GDL provides water transport from the catalyst layer to the electrodes and gas flow from the electrodes to the catalyst. The gas diffusion layer must be porous, electrically, thermally conductive, and rigid to allow the water transport and gas flow. The most common materials for the gas diffusion layer are carbon fiber-based materials such as carbon fiber papers and woven carbon fabrics or cloths [89]. At high temperatures, the hydrophobicity of the GDL decreases increasing the water retention and thus prone to flooding [103].

From the discussion of the MEA components, the temperature and heat generated by operating the fuel cell affect fuel cell performance. The balance of plant components controls the temperature, heat rejection, and humidification in the fuel cell to obtain efficient fuel cell performance. The balance of plant components are explained in the next section.

1.4 Balance of Plant (BOP)

The balance of plant components (BOP) are responsible for cooling the fuel cell stack, providing enough reactants, and allowing the humidification of reactants before they enter. The BOP also allows adequate recirculation for hydrogen and water to allow efficient fuel cell operation. The BOP usually consist of a compressor for the air delivery system and a pump/heat-exchanger/fan for the cooling system. They also include a pump for hydrogen recirculation and water pumps or humidifiers for membrane humidification. The BOP components for liquid-cooled stacks are shown in Fig. 1.4. The combination of the BOP with the fuel cell is known as the fuel cell system.

The fuel cell system can be broken into four subsystems to improve the performance of the fuel cell, such as improving the electrochemical reactions in the stack to prevent fuel starvation and high stack temperatures and maintain stack voltage at a fixed continuous operation [126]:

- Reaction subsystem → In this subsystem, hydrogen and air are provided to the fuel cell. This subsystem is divided into the hydrogen or fuel loop. The hydrogen loop is responsible for delivering hydrogen to the fuel cell, and the air loop is responsible for providing air to the fuel cell:

- Hydrogen or fuel loop → The hydrogen flows at the anode through a fuel processor such as a gas or methanol steam reformer or directly from a hydrogen tank. This hydrogen is fed in the fuel cell through a pump. The Toyota Mirai gives an example of the BOP responsible for the fuel loop. In the Toyota Mirai, the hydrogen is obtained from two hydrogen tanks, and through a pump and pressure regulator, it goes through 3 fuel injectors, and it is fed to the fuel cell [9]. The hydrogen that flowed through the anode is drained using a valve and a liquid-gas separator and later recirculated through a pump to the fuel cell. An example of this system is shown in Fig. 1.4. The challenge with this hydrogen loop is to provide hydrogen at a certain stoichiometric ratio to ensure the efficient performance of the fuel cell. High hydrogen rates result in higher power density and greater stack efficiency but lower net power from the fuel cell due to the BOP's higher power requirement. High hydrogen rates can help by having more frequent purging from the anode side, but it can cause dehydration on the cell and, consequently, fuel cell degradation.
- Air loop → The air is provided to the cathode through a blower or fan or a compressed air tank. After passing the blower, the air is supplied through a valve to the fuel cell. In the Toyota Mirai, the BOP components used for the air loop is an air compressor and air pressure regulating valve to provide air to the fuel cell stack [9]. An example of this system is shown in Fig. 1.4. The challenge with this air loop is the airflow control at a certain stoichiometric ratio to ensure the fuel cell's efficient performance. High airflow rates result in higher power density and greater stack efficiency but lower net power from the fuel cell due to the higher power requirement from the balance of plant components. Increased airflow rates also produce more water, causing mass transport limitation and fuel cell degradation by water accumulation in the gas diffusion and catalyst layers.
- Thermal subsystem → The thermal subsystem is the most important subsystem. Almost half of the energy produced is in the heat of reaction. The main goal of this system is to maintain the temperature in the optimum operating range to keep the humidity level in the membrane. As was previously shown, a higher temperature than the operating range can cause dehydration, shrinkage, wrinkles, and even rupture in the membrane. Fans or blowers are used to cool the fuel cell system for air-cooled fuel cells and pump/heat-exchanger/fan or radiator for liquid-cooled fuel cells. In the Toyota Mirai, a radiator with two fans, a water pump, heater, heater core, rotary valve, and the 3-way valve is used for the cooling system [9].
- Water management subsystem → The subsystem's primary goal is to maintain the mem-

brane hydrated and efficient water distribution within the fuel cell to avoid dehydration or flooding. The fuel cells are internally humidified through direct water injection to reduce the BOP price. The Toyota Mirai uses an internal humidifier [166] as shown in Fig. 1.4.

- Power electronics and energy sources subsystem → This subsystem balances the fuel cell power to satisfy load demands without abrupt transients or changes in fuel cell power demand to avoid fuel cell degradation. Therefore power electronics are used to control the fuel cell power drawn to power up the vehicle. The most commonly used power electronic to regulate the fuel cell voltage is DC/DC converters. Fuel cells, unfortunately, have a slow dynamic response, and therefore it cannot sustain the abrupt changes during startup and transient of the vehicle. Consequently, it has to be combined with other energy sources such as batteries or supercapacitors or a combination of both. In the Toyota Mirai, the fuel cell system is combined with a battery [9]. For the 2021 Toyota Mirai in [147] the battery consists of a lithium ion 1.24 kWh battery.

1.5 Power Split

Different control strategies have been used to determine the optimal power split required for an FCV. The overall hydrogen consumption of the fuel cell vehicle needs to be minimized to achieve efficient fuel cell and vehicle operation. Generally, the cost function consists of minimizing the hydrogen consumption over an entire trip:

$$J = \int \dot{m}_f dt = \frac{I_{fc} n_{fc} M_{H_2}}{2F} \quad (1.4)$$

where J is the cost, \dot{m}_f is the hydrogen consumption, $M_{H_2} = 2.016 \times 10^{-3} \frac{kg}{mol}$ is the hydrogen molar mass, and $F = 96,485 \frac{C}{mol}$ is the Faraday's constant. The cost function can have other terms to minimize and weights to penalize these terms. The limitation of these strategies is that the driving cycle of the vehicle needs to be known beforehand. Other formulations consist of defining an instantaneous cost function, which is updated with time. The limitation with the instantaneous cost function is that the models and formulation need to be as simple as possible to avoid the high computational cost. In the following sections rule-based control strategies such as proportional-integral control and fuzzy logic control will be discussed and the role of these strategies in determining the power split required for an FCV will be explained. Optimal control strategies such as dynamic programming, Pontryagin's Minimum Principle, equivalent consumption minimization strategy, model predictive control, and machine learning are also explained.

1.5.1 Rule-based Control (RBC) Strategies

Rule-based strategies consist of rules based on experience with the goal to obtain an efficient power split between the fuel cell and an energy source storage such as battery or capacitor. These rules are easy to implement but it is hard to determine whether they are optimal or not since they aim at maintaining a desired battery state of charge and not necessarily minimizing the overall energy consumption. The key point here is that the usefulness of consuming battery energy at a given point in time depends on future energy (hydrogen) used later to supplement this energy. The instantaneous conditions for the power split are thus hard to decide. Examples of rule-based strategies are proportional-integral control, as shown in Fig. 1.5.

A proportional-integral (PI) controller is a feedback control loop that consists in calculating the error ($e(t) = r - y(t)$) between a reference value $r = SOC_{ref}$ and the output of the system $y(t) = SOC$. The SOC_{ref} is based on rules derived heuristically and aims to balance the use of battery to offset the use of FC and hence hydrogen. These rules are often expressed via IF-THEN rules and membership functions, which define certain situations and conditions that would enable either one or two energy sources between the main and the auxiliary energy sources. The IF-THEN rule-based method has become popular due to the easy implementation of simple rules without having to understand the complexity of the problem completely [126]. Many researchers have implemented fuzzy logic controllers in FCV [160]. Once the rules guide to a fixed or slowly varying reference battery state of charge, the remaining tuning relies on classical control techniques.

A proportional-integral controller was implemented in [154] for a full hybrid power system. The system included a PEMFC Horizon H-100, lithium-ion battery pack, and DC/DC unidirectional and bidirectional converter. The system's states consist of the inductor current and the DC/DC converter's output voltage. The fuel cell model consisted of an equivalent electrical circuit with a variable double layer capacitor to display the transient characteristics. As typically done in such power split controllers, the fuel cell operating temperature was kept constant at 60°C, but the optimal temperature setpoint was not investigated. The PI controller gains are tuned through the converter's frequency response analysis using a linearized model at the nominal operating point. Another example of a PI controller that controls the DC bus voltage for a hybrid source for automotive application with experimental validation can be found in [14].

Besides using the PI controller for the state of charge regulation or control, it can be used for the fuel cell's airflow control to avoid starvation, which damages the stack and limits the power drawn from the fuel cell. In [33] a decoupled controller for a fuel cell hybrid system with batteries is experimentally validated. A classical control strategy is used for the fuel cell current demanded and battery beside the PI controller's airflow control. Mahjoubi used two proportional-integral controllers to control the airflow and temperature to avoid oxygen starvation and the drop of system efficiency while extending fuel cell lifetime [87].

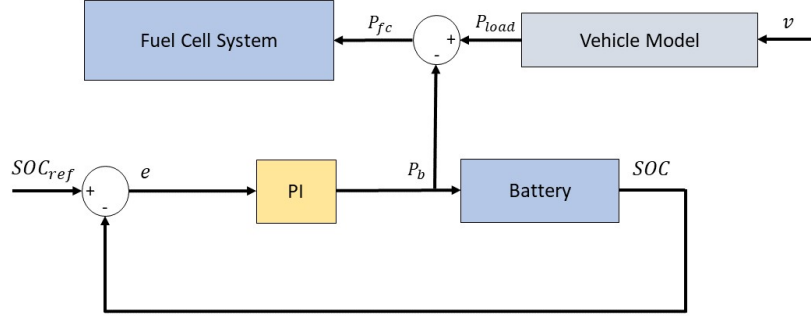


Figure 1.5: Schematic of simple proportional-integral control implementation.

PI control has also been used to maintain the fuel cell current in the presence of load disturbance [31]. Two PI controllers were developed to obtain the power split by controlling the fuel cell's efficiency and the state of charge (SOC) of a fuel cell/battery passenger vehicle [13]. The double PI controller reduced hydrogen consumption by 1.4% compared to a simple PI controller that only controls the SOC of the battery. PI control has also been combined with heuristic control strategies such as fuzzy control to achieve the power split of a fuel cell and battery configuration with temperature control [149]. Despite the popularity of the PI controller, tuning the PI controller gains when the reference state of charge varies can be challenging.

Due to their low computational load, rule-based strategies can be easily implemented in real time in a FCV. The Toyota Mirai power split can be deduced from [9] and the modeling work of [30]. The Mirai strategy consists of a set of basic rules where the fuel cell is turned off during braking and idling. During driving conditions, the energy management is achieved through a load-following strategy that maintains the battery state of charge. Despite having a strong load following energy management, [30] showed in simulations lower fuel cell degradation compared to a more load-leveling strategy. In subsequent sections, we discuss how the battery state of charge can be defined based on an equivalent consumption minimization strategy.

1.5.2 Dynamic Programming (DP)

Dynamic Programming (DP) is a numerical method that finds the optimal control sequence that minimizes a given cost function, in this case hydrogen consumption given constraints and a desired final battery state of charge. Since the optimal decision at every instant depends on the future demands and constraints, DP starts from the final step and propagates backward assuming knowledge of the entire load trajectory. Different papers applying DP have been developed with schemes similar to Fig. 1.6. In the literature, DP has been widely used to achieve the best performance in consideration of hydrogen fuel consumption [177, 79] and other objectives such as fuel life or degradation [35, 40, 64]. Especially, in [64], the authors show that the optimal solution obtained

from DP could lead to a 4.1% reduction in hydrogen consumption by including thermal management and fuel cell degradation in the fuel cell modeling, showing the importance of including these factors in the optimal power split formulation. In [35], lookup tables based on experimental testing of an actual fuel cell (FC) test-bench are developed. The fuel cell power include the auxiliary power of the components used, such as water pumps, air conditioning, and compressor. The operating temperature of the fuel cell is not specified. It is shown with simulations that the weighted DP improves hydrogen consumption compared to a state machine control algorithm for a fuel cell battery vehicle.

1.5.3 Pontryagin's Minimum Principle (PMP)

Even though DP gives the optimal solution, its computational time exponentially increases as the number of states increases. Therefore, PMP can be an alternative solution to solve the control problem on FCVs. PMP consists of solving a set of conditions necessary for optimality. In [175], PMP used fuel cell power as an input (P_{fc}) and state of charge (SOC) as a state. A schematic of the PMP formulation can be found in Fig. 1.6. The cooling system is composed of a compressor and other auxiliary components. A comparison between PMP to a rule-based energy management strategy was performed with respect to lower hydrogen consumption. In [80] an SOC and battery current constraint was applied to PMP and they compared results to PMP without these constraints. They also studied how these constraints applied to PMP affected battery lifetime and battery energy loss. They showed that with the constraints applied the energy loss was reduced by 5.6% and battery lifetime by 0.417%. Zhengh also applied PMP to obtain the power split of a FCV vehicle but it included a fuel cell system lifetime factor in the fuel cell system cost besides a SOC constraint [173]. They showed that the combination of the lifetime factor and SOC constraint increases the fuel cell consumption compared to SOC constraint only.

1.5.4 Equivalent Consumption Minimization Strategy (ECMS)

The ECMS has been proven to be equivalent under certain conditions to Pontryagin's minimum principle. The equivalent consumption minimization strategy is a heuristic method that consists of reducing the global minimization problem into an instantaneous minimization problem. It is solved at each instant, only using a weighted value of the electric energy and on the actual energy flow in the powertrain. An ECMS, which was first proposed in [112] for hybrid electric vehicles, has been applied to fuel cell electric vehicles. In [148], ECMS is used to find the optimal energy management for an agricultural tractor consisting of fuel cells and lithium ion batteries for minimizing the hydrogen consumption of the vehicle. In [172], energy management using ECMS was used for a fuel cell hybrid vehicle using batteries and a supercapacitor. The ECMS only considered

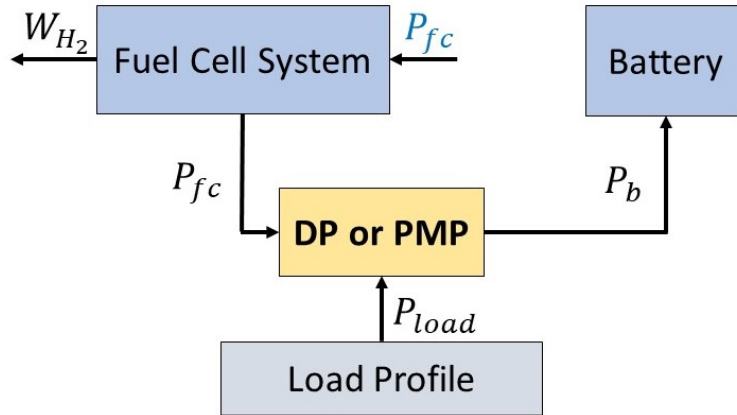


Figure 1.6: Dynamic programming (DP) and Pontryagin's Minimum Principle (PMP) schematic. In the dynamic programming (DP) and Pontryagin's Minimum Principle (PMP) formulation in [35] and [175], fuel cell power is used as an input (P_{fc}) and state of charge (SOC) as a state.

an optimum power of the fuel cell and battery by adding a penalty factor in terms of the battery SOC and fuel cell's mean efficiency. Fuel cell and battery degradation are not considered and the simulation tool is not specified. More importantly, the FC system assumes a constant power of 11 kW for the total power of the auxiliary components, namely an air-conditioner and a compressor. The fuel cell model consists of lookup tables, but the operating temperature is not specified pointing to the need for more comprehensive effort and experimentation for this promising work.

Notably, ECMS can be formulated in consideration of different factors besides the weighted electric energy. An example can be found in [54] where a battery and fuel cell-powered locomotive used an ECMS with a dynamic factor that considered the influence of recycling the braking energy of the battery to obtain the power split.

1.5.5 Model Predictive Control (MPC)

MPC uses model prediction to satisfy constraints on the input and output variables and measurements to adjust the actions [133]. MPC was used for buses and other applications that depend on the dynamic response of fuel cell and batteries [51]. Many comparisons of the performance of a battery charge control, fuel cell dynamics [81] and fuel cell thermal dynamics [168] were performed. These constraints were applied to avoid fuel cell degradation [44, 58]. The simulation results explored these constraints and their effect on hydrogen consumption, including auxiliary component losses for the cooling system.

1.5.6 Machine Learning

Machine learning consists of tools that detect patterns in data and these patterns are used to predict future behavior or perform decisions under uncertainty. Machine learning method has been used, despite requiring large amounts of data, because of the excellent performance of trained models on the FCV. In [83] machine learning was used to obtain a set of rules to improve the energy consumption economy of FCVs. Reinforcement learning was used in [55] for the dynamic energy management of an FCV with batteries. The reinforcement learning method consists of an agent observing the behavior of the data and updating the values of the parameters of the model through a reward function. One experiment where the reward function only accounts for charge sustaining SOC is included in [55]. It was possible to show that on different driving cycles reduced hydrogen consumption was achieved compared to the first experimental formulation. Reinforcement learning has also been used to improve the lifetime of the battery and efficiency of the power system by limiting the state of charge variation in a fuel cell and battery system configuration [127]. In [171] reinforcement learning was used to optimize the energy efficiency of FCVs and slow down the aging of (PEMFC). Another example of reinforcement learning with the promise of future online implementation can be found in [159]. In [159] the optimal energy management problem of plug-in hybrid fuel cell and battery systems was implemented.

1.6 Battery Sizing and Lithium Ion Battery Chemistries

Besides determining the optimal power split required for an FCV, battery sizing is another critical problem to achieve an optimal fuel cell operation since it affects the weight of the vehicle and therefore the fuel consumption. Contrary, the battery sizing is affected by a drive cycle [155], a control policy [144], and hardware architecture [143] making it challenging to find an optimal size. Furthermore, studies have shown that battery sizing should be obtained in consideration of various factors, including fuel cell consumption, start/stop periods, system cost, and battery/FC degradation [155, 91].

1.7 Thesis Organization and Contributions

From the previous summary and literature review discussed in section 1.5, the following gaps are identified:

- a) The importance of taking into account the parasitic losses from the BOP components and strategies with fixed temperature and humidity setpoints. Models and methods to address these sizing and set-point selection challenges are developed and analyzed in Chapter 3.

- b) There is a lack of studies for the right sizing of batteries and FCs. Flexible methods of varying complexity for integrating and optimizing a hybrid FCV power split are in Chapter 4.
- c) The choice of the right battery chemistry and its ability to act as a power source with limited energy influences the power split in a hybrid FCV and increases the importance of high battery utilization and accurate SOC. This deeper understanding and a novel methodology for improving SOC accuracy so that small batteries can be used with high confidence is shown in Chapter 6.
- d) The emergence of highly automated and connected vehicles that are able to modify their velocity profile while performing a mission motivates the work in Chapter 5 where the power split and the vehicle velocity are co-optimized.

Therefore, the contributions and thesis organization are as follows: In Chapter 2, a 0D fuel cell model and the assumptions to capture the behavior for a 15 KW Hydrogenics liquid-cooled stack is explained. An empirical fuel cell model for a Ballard 1200 ACS air-cooled stack is described. An explanation of the reasoning behind modeling both the air-cooled and liquid-cooled fuel cell for the different military vehicles under study in this thesis, as shown in Fig. 1.7 is given. The balance of plant components used and modeled for the air-cooled and liquid-cooled fuel cell are also explained. The analysis has been done to address if the fuel cell models' developed in this thesis fit the military vehicle operating conditions' needs.




Chapter	Vehicle	Power	Weight	Power Split	Airpath	Cooling	Vehicle Optimization	Sizing
III	Packbot robot 	230 W	24 kg	✓	✓	✓		
V	SMET 	30 kW	454 kg	✓	○	○	✓	
VI	Medium size 	270 kW	11113 kg	✓	○	○		✓

Figure 1.7: Summary of the different military vehicles with the corresponding components analyzed for this thesis. Checkmarks mean the analysis has been investigated. Circles represent that the component's load has been taken into account but not its overall behavior.

In Chapter 3, a pseudospectral optimization method is applied to obtain an optimal power split while considering the fuel cell's thermal dynamics to avoid stack overheating and minimize the hydrogen consumption for a hybrid electric vehicle. A dual-loop proportional plus integral (PI) control strategy is proposed to regulate the airflow by following a fuel cell temperature reference for future online implementation. In contrast, another PI controller regulates the fuel cell current by tracking a reference battery state of charge (SOC). The PI controllers track the optimal temperature setpoint from the pseudospectral results and a linear reference for the SOC while achieving 96% of the optimum hydrogen consumption fuel savings with complete preview information. The work has been accepted to be presented and published in the Modeling, Estimation, and Control Conference (MECC 2021).

In Chapter 4, the performance of dynamic programming and equivalent minimization consumption for a plug-in hybrid fuel cell medium-sized battery vehicle is compared when the equivalent factor has been well tuned for a known duty cycle. The power density of this application dictates a liquid cooling system that can maintain optimum FC temperature independently of the air supply. Since the power required to operate a radiator and fan for a liquid cooling system is a fraction of the power generated, the losses from the thermal subsystem are ignored. The resulting system consists of one input (fuel cell's current) and one state (the state of charge of the battery). The control strategies' performance is compared under different battery sizes to study battery sizing on fuel cell operation and hydrogen consumption. The effect of battery chemistry on battery power and how it affects the power split is also investigated.

In Chapter 5, co-optimization and sequential optimization were compared for a hybrid fuel cell liquid-cooled with battery SMET vehicle in terms of energy consumption, operating modes, and computational cost. Using Pontryagin's Minimum Principle (PMP) with distance, vehicle speed, and state of charge (SOC) as states, we find that the co-optimization can be formulated with one discrete variable describing vehicle operation and another continuous variable for power distribution. The reformulation is done to reduce computation while implementing Dynamic Programming. The sequential optimization consists of two stages. The first stage consisted of solving the cost function in terms of distance to obtain an optimal speed profile. The second stage takes the obtained speed profile and solves the minimum hydrogen consumption cost function in terms of distance. The contribution of this work is to answer if co-optimization is beneficial compared to sequential optimization. This contribution helps us understand the tradeoff between system accuracy and optimality between co-optimization and sequential optimization. The work is published in [68].

In Chapter 6, a LQE based on a moving window of past F measurements was applied and developed to improve SOC estimation on a lithium iron phosphate battery. The voltage–SOC relation for the lithium iron phosphate battery is flat (low slope), making SOC estimation using measured

voltage difficult. The developed observer consists of combining voltage and force measurements to improve SOC estimation. The observer's voltage model consists of a double resistance-capacitance pair equivalent circuit model using current as input and state of charge (SOC), and the resistance-capacitance pairs voltages (V_1 , V_2) as states. The force model uses a Force-SOC model consisting of a static piecewise-linear function model that uses current as input and state of charge (SOC, z) as the state [37]. The methodology's contribution is to improve the SOC estimation by adding the force measurement while addressing the non-monotonic F-SOC relationship that can cause convergence to a wrong SOC value. The novel switching estimation gain is based on determining the operating region corresponding to the actual SOC, which helps obtain convergence to the correct SOC value. The DST profile is used for the observer's simulation and experimental validation. The developed observer's performance improved SOC estimation compared to the classical voltage observer based on voltage measurements. The work is published in [37].

In Chapter 7, the conclusion and future work will be explained.

CHAPTER 2

Fuel Cell System Modeling

2.1 Introduction

There are different ways to model the fuel cell behavior, and they can be classified into three categories [22]: empirical, semi-empirical, and physical models. Empirical models consist of using simple models (such as polynomials) to match experimental data. Due to the dependence on the experimental data's operating conditions, the empirical models typically have limited predictive capability around the experimental operating conditions where data for fitting was collected. These models are excellent for interpolating between operating conditions in the training data sets but often fail to extrapolate well. The empirical models' advantage is that it provides simple means for simulating and comparing the system's performance under different operating conditions. Semi-empirical models combine equations for conservation of species and charge with empirical models for rate kinetics and transport such as diffusion. These models can capture the transport phenomena (such as mass transport of the reactants and water across the cell). Due to the underlying physics, these models have better predictive ability than purely empirical models. They cannot operate outside of the range they were designed or validated. Due to the empirical equations, approximations of the transport phenomena within the cell are still present. Lastly, physical models use partial differential equations that describe the 3-D micro-structure in the fuel cell. These models are more realistic and accurate but require high computational cost and time methods such as computational fluid dynamics (CFD) to be solved.

The fuel cell models are classified as 0-D, 1-D, 1+1D, 2D, or 3D models. 3D models consist of modeling the transport equations in all directions (x , y , and z) as shown in Fig. 2.1. These models precisely capture the fuel cell model transport behavior, but it comes with a high computational cost. Examples of 3D models can be found in [50],[86],[158]. 2D models have been developed to reduce the computational cost and capture the transport equations. These models are solved across the x and y (or x and z) dimensions, as shown in Fig. 2.1. Examples of 2D models can be found in [151], [94], [102]. In 1+1D, the transport equations are solved and analyzed without completely

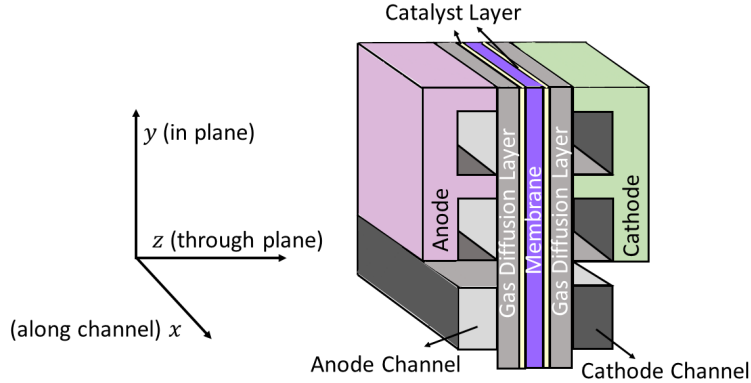


Figure 2.1: Length scales and computational domains for PEMFC modeling. 1-D models usually consist of capturing transport behavior across the x dimension. 2-D models consist of analyzing the transport behavior across x and y (or x - z) dimensions. Lastly, 3-D models consist of studying transport behavior across all dimensions (x , y , and z).

solving the equations on both dimensions (x and y) to reduce the computational cost further. In 1-D models, the transport analysis across one dimension (x) of the fuel cell is modeled and studied. The x -direction in Fig. 2.1 is often two orders of magnitude smaller than the y and z dimensions. The aspect ratio of x against y and z can be leveraged by analyzing the physics to decouple x -direction transport in the GDL from y - z transport in the channel. Examples of 1D models can be found in [138], [93], [164]. In 0-D models, the analysis of the parameters over the spatial domain is not considered. Examples of 0-D models can be found in [121], [109], [72]. Therefore, since the computational complexity scales with the N -dimensions, a 3-D semi-empirical model could be much more computationally costly than the 0-D physics-based model making 0-D based models more ideal for control applications.

The fuel cell model can further be divided into fuel cell system modeling and stack modeling. The fuel cell stack model captures the reactions occurring within the anode, cathode, and MEA. The fuel cell system model represents the balance of plant components' behavior and how it affects the fuel cell. A 0-D semi-empirical liquid-cooled stack model is developed in this thesis. The 0-D fuel cell stack model will be divided into the cathode, anode, membrane hydration, and fuel cell voltage subsystem. The fuel cell voltage subsystem's parameterization for a 15 kW Hydrogenics liquid-cooled stack is described and used. The airpath subsystem for the 15 kW Hydrogenics liquid-cooled stack is also presented. An empirical model for an air-cooled stack model (for a Ballard 1200 ACS) onto which an augmented semi-empirical thermal model that includes fan power consumption for future study of the energy optimization is also described.

2.2 0-D Semi-empirical Liquid-cooled Stack Fuel Cell Model

The fuel cell model developed for the liquid-cooled stack will be divided into the fuel cell stack and compressor (airpath subsystem) models. The input for the fuel cell model is the fuel cell current, and the output is the stack power, while for the compressor, the input is the same, but the output will be the compressor power. The fuel cell stack model consists of four subsystems: the cathode, anode, membrane hydration, and fuel cell voltage subsystem. The fuel cell voltage subsystem explains how to model the fuel cell's reactions through a voltage vs. current density function called polarization curve. In the cathode subsystem, the mass transport equations describe how the airflow affects the fuel cell's voltage. The anode subsystem consists of mass transport equations to know how the hydrogen supplied to the fuel cell changes its operation. The membrane hydration subsystem describes how the relative humidity and the fuel cell's temperature affect the hydration of the membrane in the fuel cell which impacts proton conductivity, gas crossover rate, and fuel cell performance. Each subsystem is explained in the following subsections.

2.2.1 Fuel Cell Voltage Subsystem

All the electrochemical reactions occurring in the fuel cell can be described by a voltage versus current (or current density) relationship called polarization as shown in Fig. 2.2. The polarization curve consist of the following terms:

$$V_{fc} = V_0 - v_{act} - v_{ohm} - v_{conc} \quad (2.1)$$

where V_{fc} is the voltage of a single cell in a fuel cell and V_0 is the fuel cell's theoretical potential given as a function of fuel cell temperature (T_{fc}):

$$V_0(T_{fc}) = 1.256 - 2.26 \times 10^{-4} T_{fc} \quad (2.2)$$

The value of 1.256 V is used since the theoretical potential of fuel cells for different chemistries varies from 0.8-1.5 V [109], and 1.25 V is a typical value for PEMFC operation on hydrogen [43]. The polarization losses consist of the terms v_{act} , v_{ohm} , and v_{conc} . The activation loss or activation overvoltage (v_{act}) captures the behavior from oxidation and reduction reactions in the anode and cathode and is given as $v_{act} = \frac{RT_{fc}}{F} \operatorname{asinh} \left(\frac{i_{loss} + i}{2i_{oc}} \right)$. The ohmic losses (v_{ohm}) is a term that captures the resistance of the membrane to the transfer of protons and electrons denoted as $v_{ohm} = iR_{mb}$. The concentration loss or concentration overvoltage (v_{conc}) is the limiting current density due to mass transport limitations resulting in a drop in the reactants and is written as $v_{conc} = B_c \log \left(1 - \frac{i}{i_{max}} \right)$.

The polarization curve formulation used in our fuel cell model is given by:

$$V_{fc} = V_0(T_{fc}) + \frac{RT_{fc}}{nF} \log \left(\frac{p_{H_2} \sqrt{p_{O_2}}}{p_v} \right) - \frac{RT_{fc}}{F} \operatorname{asinh} \left(\frac{i_{loss} + i}{2i_{oc}} \right) - iR_{mb} + B_c \log \left(1 - \frac{i}{i_{max}} \right) \quad (2.3)$$

The universal gas constant is $R=8.3145 \text{ J/molK}$, $F=96,485 \text{ C/mol}$ is the Faraday constant, and $n=2$ is the number of moles of hydrogen. The current density loss due to hydrogen crossover is given by i_{loss} , i_{oc} is the exchange current density, R_{mb} is the membrane resistance of the fuel cell, B_c is the mass transport loss coefficient, and i_{max} is the limiting current density.

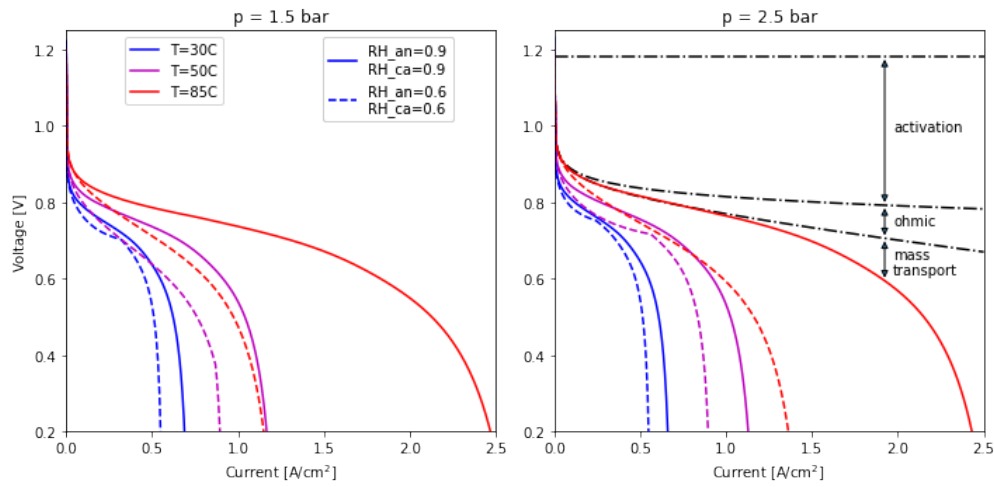


Figure 2.2: Impact of the fuel cell temperature, relative humidity and operating pressure on fuel cell polarization curve. Figure obtained from [38].

Various conditions affect the polarization curve and the performance of the fuel cell. As shown in Fig. 2.2, the fuel cell voltage decreases as the current drawn from the fuel cell increases and depends in a nonlinear way on cell temperature, humidity, and the pressures (such as the partial pressure of hydrogen (p_{H_2}), oxygen (p_{O_2}), and water vapor (p_v)). In section 2.2.2 the membrane hydration model and the relationship between R_{mb} and relative humidity are explained. To understand the relationship between relative humidity and temperature with the partial pressure of oxygen and water vapor, the mass transport equations are explained in section 2.2.3 for the cathode. In section 2.2.4 the mass transportation equation are explained for the anode to understand how the temperature and relative humidity affects the partial pressure of hydrogen.

2.2.2 Membrane Hydration Subsystem

The membrane resistance depends highly on temperature and membrane hydration as shown by the following equations:

$$R_{mb} = \frac{\delta_{mb}}{\sigma_{mb}} \quad (2.4)$$

where δ_{mb} is the membrane thickness and σ_{mb} is a function of membrane water content (λ_{mb}) and fuel cell temperature given as:

$$\sigma_{mb} = b_1 \exp \left(b_2 \left(\frac{1}{303} - \frac{1}{T_{fc}} \right) \right) \quad (2.5)$$

where b_1 is provided as a function of membrane water content:

$$b_1 = b_{11} \lambda_{mb} - b_{12} \quad (2.6)$$

where b_2 , b_{11} , b_{12} , are constants and determined empirically. The membrane water content (λ_{mb}) is given as:

$$\frac{d\lambda_{mb}}{dt} = K_{mb} (N_{v,ca,mb} - N_{v,an,mb}) \quad (2.7)$$

where $K_{mb} = EW/(\rho_{mb}\delta_{mb})$ is the membrane water uptake, EW is the equivalent weight of the membrane, ρ_{mb} is the membrane dry density, and δ_{mb} is the membrane thickness. The water flux out of the membrane and into the anode GDL ($N_{v,an,mb}$) is given by:

$$N_{v,an,mb} = 2 \frac{D_w (\lambda_{mb}, T_{fc}) (\lambda_{mb} - \lambda_{an})}{\delta_{mb}} - \frac{i_{fc} n_d}{F} \quad (2.8)$$

where D_w is the diffusion in the membrane and λ_{an} is the water content at the membrane interface with the anode GDL. The λ_{an} is given as:

$$\lambda_{an} = (1 - s_{ctl,an}) \lambda_{T,a} + s_{ctl,an} \lambda_{max} \quad (2.9)$$

where $\lambda_{max} = 22$ is the water content of a liquid equilibrated membrane, $\lambda_{T,a}$ is the membrane water uptake isotherm, and $s_{ctl,an}$ is the catalyst liquid saturation given as follows:

$$s_{ctl,an} = \frac{\max(N_{l,an,0})}{N_{L,max}} \quad (2.10)$$

where $N_{l,an}$ is the rate of water accumulation in the GDL condensing into the liquid phase given as:

$$N_{l,an} = N_{v,an,mb} - N_{v,an} \quad (2.11)$$

The maximum liquid water flux the catalyst layer can handle before becoming completely saturated is denoted by $N_{L,max}$ and is given by the following equation:

$$N_{L,max} = N_{L0} \left(\exp \left[N_{L1} \left(\frac{1}{303} - \frac{1}{T_{fc}} \right) \right] \right) \quad (2.12)$$

where N_{L0} and N_{L1} are tunable parameters. The same set of equations currently explained can be used for the cathode to obtain the water flux out of the membrane and into the cathode GDL ($N_{v,ca,mb}$) but with a slight change of sign to change the coordinated axis and with water generation as shown by the denoted equations:

$$\frac{i_{fc}}{2F} - N_{v,ca,mb} = N_{v,ca} + N_{L,ca} \quad (2.13)$$

$$N_{v,ca,mb} = 2 \frac{D_w (\lambda_{mb}, T_{fc}) (\lambda_{ca} - \lambda_{mb})}{\delta_{mb}} - \frac{i_{fc} n_d}{F} \quad (2.14)$$

The relative humidity affects the diffusion in the membrane D_w which is also a function of the activity in membrane given by the following equations:

$$a_{mb} = \frac{a_{an} + a_{ca}}{2} \quad (2.15)$$

$$a_i = \frac{p_{v,i}}{p_{sat,i}} \quad (2.16)$$

where i could be cathode (ca) or anode (an). The diffusion in the membrane equations can be found in [135]. The partial pressure of water vapor at the inlet of the cathode and anode is given by:

$$p_{v,i,in} = \phi_{i,in} p_{sat}(T_{fc}) \quad (2.17)$$

where $\phi_{i,in}$ is the relative humidity at the inlet of the cathode ($i = ca$) and anode ($i = an$). Therefore, the relative humidity will influence the water content in the membrane through the activities in the cathode and anode affecting the diffusion in the membrane. To obtain the partial pressure of water in the cathode and anode the mass transport equations need to be solved. The membrane hydration affects also the mass transport equations in the cathode and the anode through the following terms:

$$W_{v,ca,mb} = N_{v,ca} M_v A_{fc} n_{fc} \quad (2.18)$$

$$W_{v,an,mb} = N_{v,an} M_v A_{fc} n_{fc} \quad (2.19)$$

where $W_{v,ca,mb}$ is the mass flow rate between the GDL and the cathode and $W_{v,an,mb}$ is the mass flow rate between the GDL and the anode. The molar mass of water vapor is $M_v = 18e^{-3}$ kg/mol, A_{fc} is the fuel cell active area, and n_{fc} is the number of fuel cells in the stack. Most of the parameters

values presented in this section can be found in [135] and [122]. In the following section the mass transport equations for the cathode and the relationship with partial pressure of oxygen and water vapor are explained.

2.2.3 Cathode Subsystem

In the cathode subsystem, the behavior of the airflow inside the fuel cell is captured through the mass transport or mass continuity equations as shown by the following (some of these equations can be found on [122]):

$$\frac{dm_{O_2,ca}}{dt} = W_{O_2,in} - W_{O_2,out} - W_{O_2,rect} \quad (2.20)$$

$$\frac{dm_{N_2,ca}}{dt} = W_{N_2,in} - W_{N_2,out} \quad (2.21)$$

$$\frac{dm_{v,ca}}{dt} = W_{v,in} - W_{v,out} + W_{v,gen} - W_{v,ca,mb} \quad (2.22)$$

where $W_{O_2,in}$ is the mass flow rate of oxygen entering the cathode, $W_{O_2,out}$ is the mass flow rate of oxygen leaving the cathode, and $W_{O_2,rect}$ is the rate of oxygen reacted in the fuel cell. The mass flow rate of nitrogen entering the cathode is given by $W_{N_2,in}$ and $W_{N_2,out}$ is the mass flow rate of nitrogen leaving the cathode. The mass flow rate of water entering the cathode is given by $W_{v,in}$, $W_{v,out}$ is the mass flow rate of water leaving the cathode, and $W_{v,gen}$ is the water generated at the fuel cell. $W_{O_2,in}$, $W_{N_2,in}$, and $W_{v,in}$ are given by the following equations:

$$W_{O_2,in} = \frac{W_{in}y_{O_2,in}M_{O_2}}{y_{O_2,in}M_{O_2} + y_{v,in}M_v + (1 - y_{O_2,in} - y_{v,in})M_{N_2}} \quad (2.23)$$

$$W_{N_2,in} = \frac{W_{in}(1 - y_{O_2,in} - y_{v,in})M_{N_2}}{y_{O_2,in}M_{O_2} + y_{v,in}M_v + (1 - y_{O_2,in} - y_{v,in})M_{N_2}} \quad (2.24)$$

$$W_{v,in} = \frac{W_{in}y_{v,in}M_v}{y_{O_2,in}M_{O_2} + y_{v,in}M_v + (1 - y_{O_2,in} - y_{v,in})M_{N_2}} \quad (2.25)$$

where W_{in} is the airflow entering the cathode, $y_{O_2,in}$ is the oxygen mole fraction at the cathode inlet, $y_{v,in}$ is the water vapor mole fraction at the cathode inlet, $M_{O_2} = 32e^{-3}$ kg/mol is the molar mass of oxygen, $M_{N_2} = 28e^{-3}$ kg/mol is the molar mass of nitrogen, and $M_v = 18e^{-3}$ kg/mol is the molar mass of water vapor. $y_{O_2,in}$ and $y_{v,in}$ are given by the following equations:

$$y_{O_2,in} = \frac{p_{O_2,in}}{p_{in}} \quad (2.26)$$

$$y_{v,in} = \frac{p_{v,in}}{p_{in}} \quad (2.27)$$

where p_{in} is the inlet pressure, $p_{v,in}$ is the water vapor pressure at the cathode inlet, and $p_{O_2,in}$ is the oxygen pressure at the cathode inlet. The pressures are calculated with the following equations:

$$p_{v,in} = \phi_{in} p_{sat}(T_{fc}) \quad (2.28)$$

$$p_{O_2,in} = 0.21(p_{in} - p_{v,in}) \quad (2.29)$$

$$p_{in} = \frac{W_{in}}{K_{in}} + p_{ca} \quad (2.30)$$

where ϕ_{in} is the relative humidity at the cathode inlet, K_{in} is the manifold pressure constant at the inlet, and P_{ca} is the cathode pressure. The saturated pressure ($p_{sat}(T_{fc})$) is given as a function of fuel cell temperature (obtained from [11]) as:

$$p_{sat}(T_{fc}) = \exp\left(\frac{-5800}{T_{fc}} + 1.39 - 0.05T_{fc} + 0.42e^{-4}T_{fc}^2 - 0.14e^{-7}T_{fc}^3 + 6.55 \log(T_{fc})\right). \quad (2.31)$$

$W_{O_2,rct}$ and $W_{v,gen}$ are calculated as:

$$W_{O_2,rct} = \frac{M_{O_2} n_{fc} I_{fc}}{4F} \quad (2.32)$$

$$W_{v,gen} = \frac{M_v n_{fc} I_{fc}}{2F}. \quad (2.33)$$

$W_{O_2,out}$, $W_{N_2,out}$, and $W_{H_2O,out}$ are given by the following equations:

$$W_{O_2,out} = \frac{W_{out} y_{O_2,ca} M_{O_2}}{y_{O_2,ca} M_{O_2} + y_{v,ca} M_v + (1 - y_{O_2,ca} - y_{v,ca}) M_{N_2}} \quad (2.34)$$

$$W_{N_2,out} = \frac{W_{out} (1 - y_{O_2,ca} - y_{v,ca}) M_{N_2}}{y_{O_2,ca} M_{O_2} + y_{v,ca} M_v + (1 - y_{O_2,ca} - y_{v,ca}) M_{N_2}} \quad (2.35)$$

$$W_{v,out} = \frac{W_{out} y_{v,ca} M_v}{y_{O_2,ca} M_{O_2} + y_{v,ca} M_v + (1 - y_{O_2,ca} - y_{v,ca}) M_{N_2}} \quad (2.36)$$

where W_{out} is the airflow leaving the cathode, $y_{O_2,ca}$ is the oxygen mole fraction at the cathode inlet, and $y_{v,ca}$ is the water vapor mole fraction at the cathode inlet. $y_{O_2,ca}$ and $y_{v,ca}$ are calculated as:

$$y_{O_2,ca} = \frac{p_{O_2,ca}}{p_{ca}} \quad (2.37)$$

$$y_{v,ca} = \frac{p_{v,ca}}{p_{ca}} \quad (2.38)$$

where $p_{v,ca}$ is the partial water vapor pressure and $p_{O_2,ca}$ is the oxygen partial pressure. The airflow leaving the cathode W_{out} is obtained from the following equation:

$$W_{out} = K_{out}(p_{ca} - p_{amb}) \quad (2.39)$$

where K_{out} is the manifold pressure constant at the cathode outlet. For the saturated case, we solve the mass continuity equations assuming $\frac{dm_{v,ca}}{dt} = 0$ and $p_{v,ca} = p_{sat}(T_{fc})$. By solving the mass transport equations, the p_{ca} , p_{O_2} , $p_{v,ca}$, and p_{in} are obtained. The p_{O_2} and $p_{v,ca}$ affect the voltage of the fuel cell as shown in Eq. 2.3. The partial pressure of hydrogen also affects the voltage of the fuel cell. The mass transport equations in the anode and the relationship with hydrogen partial pressure is explained in the following section.

2.2.4 Anode Subsystem

In the anode subsystem, the behavior of the hydrogen inside the fuel cell is captured through the mass transport or mass continuity equations as shown by the following equations (some of these equations can be found on [122]):

$$\frac{dm_{H_2,an}}{dt} = W_{H_2,in} - W_{H_2,out} - W_{H_2,ret} \quad (2.40)$$

$$\frac{dm_{v,an}}{dt} = W_{v,an,in} - W_{v,an,out} - W_{v,an,mb} \quad (2.41)$$

where $W_{H_2,in}$ is the mass flow rate of hydrogen entering the anode, $W_{H_2,out}$ is the mass flow rate of hydrogen leaving the anode, and $W_{H_2,ret}$ is the rate of hydrogen reacted in the fuel cell. The mass flow rate of water entering the anode is given by $W_{v,in}$ and $W_{v,out}$ is the mass flow rate of water leaving the anode. $W_{H_2,in}$ and $W_{v,in}$ are given by the following equations:

$$W_{H_2,in} = \frac{W_{an,in} y_{H_2,in} M_{H_2}}{y_{H_2,in} M_{H_2} + y_{v,an,in} M_v} \quad (2.42)$$

$$W_{v,an,in} = \frac{W_{an,in} y_{v,an,in} M_v}{y_{H_2,in} M_{H_2} + y_{v,an,in} M_v} \quad (2.43)$$

where $W_{an,in}$ is the hydrogen flow entering the anode, $y_{H_2,in}$ is the hydrogen mole fraction at the anode inlet, $y_{v,an,in}$ is the water vapor mole fraction at the anode inlet, $M_{H_2} = 2e^{-3}$ kg/mol is the molar mass of hydrogen, and $M_v = 18e^{-3}$ kg/mol is the molar mass of water vapor. $y_{H_2,in}$ and

$y_{v,an,in}$ are given by the following equations:

$$y_{H2,in} = \frac{p_{H2,in}}{p_{an,in}} \quad (2.44)$$

$$y_{v,an,in} = \frac{p_{v,an,in}}{p_{an,in}} \quad (2.45)$$

where $p_{an,in}$ is the inlet pressure in the anode and $p_{v,an,in}$ is the water vapor pressure at the anode inlet. The pressures are calculated with the following equations:

$$p_{v,an,in} = \phi_{an,in} p_{sat}(T_{fc}) \quad (2.46)$$

where $\phi_{an,in}$ is the relative humidity at the anode inlet. $W_{H2,rcf}$ is calculated as:

$$W_{H2,rcf} = \frac{M_{H2} n_{fc} I_{fc}}{2F} \quad (2.47)$$

$W_{H2,out}$ and $W_{v,an,out}$ are given by the following equation:

$$W_{H2,out} = \frac{W_{an,out} y_{H2,an} M_{H2}}{y_{H2,an} M_{H2} + y_{v,an} M_v} \quad (2.48)$$

$$W_{v,an,out} = \frac{W_{an,out} y_{v,an} M_v}{y_{H2,an} M_{H2} + y_{v,an} M_v} \quad (2.49)$$

where $W_{H2,out}$ is the hydrogen leaving the anode, $y_{H2,an}$ is the hydrogen mole fraction at the anode outlet, and $y_{v,an}$ is the water vapor mole fraction at the anode outlet. $y_{H2,an}$ and $y_{v,an}$ are calculated as:

$$y_{H2,an} = \frac{p_{H2,an}}{p_{an}} \quad (2.50)$$

$$y_{v,an} = \frac{p_{v,an}}{p_{an}} \quad (2.51)$$

By solving the mass transport equations, the p_{H2} is obtained. The p_{H2} affects the voltage of the fuel cell as shown in Eq. 2.3.

2.3 Empirical Fit for Liquid-cooled Stack Voltage Subsystem

The 15kW Hydrogenics HD 15 liquid-cooled fuel cell stack (shown in Fig. 2.3) behavior will be modeled in this work. This liquid-cooled fuel cell is designed to operate at low pressure, quiet operation, rapid response to load changes, and high fuel efficiency [4].

The polarization curve parameters are obtained by using experimental data at 60° C as shown



Figure 2.3: 15kW Hydrogenics HD 15 liquid-cooled fuel cell stack. Figure from [4].

in Fig. 2.4. The fitting was done using the `lsqcurvefit` command in Matlab which solves nonlinear curve-fitting (data-fitting) problems in least-squares sense. The oxygen, hydrogen, and water vapor pressures values used to obtain the polarization curve parameters where $p_{O_2} = 0.21 \cdot (p_{ca} - p_v)$ bar, $p_{H_2} = 120$ kPa, and $p_{v,ca} = p_{sat}(T_{fc})/1000$ kPa where the cathode pressure varies between $p_{ca} = 103$ to 120 kPa depending on the airflow rate and current. The relative humidity in the cathode inlet is assumed to be 1. The parameters of the polarization model are provided in Table 2.1. The current density is given as I_{fc}/A_{fc} where $A_{fc} = 523 \text{ cm}^2$ is the stack active area.

Table 2.1: Identified parameters for one cell voltage model from the 15kW Hydrogenics HD 15 stack.

Parameters	Values
i_{loss}	8.72 mA/cm ²
i_{oc}	0.17 μ A /cm ²
B_c	0.1028 V
i_{max}	1.4508 A/cm ²
R_{mb}	0.1548 Ω cm ²

2.4 Balance of Plant (BOP) Components and Fuel Cell Net Efficiency for Liquid-cooled Fuel Cell

2.4.1 Balance of Plant (BOP) Component for Liquid-cooled Fuel Cell

The BOP components for a liquid cool system can consist of compressor, radiator and fan. The compressor is the airpath component and the radiator and fan are the cooling system components.

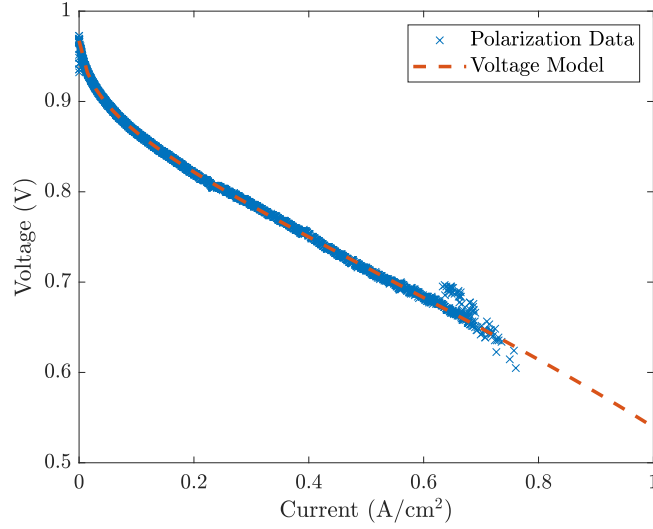


Figure 2.4: 15kW Hydrogenics HD 15 stack polarization curve data compared to fuel cell voltage subsystem model.

From the BOP, the compressor accounts up to 93.5% of the total auxiliary power consumption. The power consumption of other auxiliary components is not significant [174]. Previous work addressing control of the fuel cell system with the compressor [122],[79] has shown the impact on transient performance and energy consumption. For the 15kW Hydrogenics stack HD 15, the 10 kW aeristech compressor is within the operating range of our fuel cell [1]. We assume 2 fuel cell stacks will be operated by one 10 KW compressor for the cathode air supply. For the radiator fan, a SPAL 12V axial fan is within the operating range of the 15kW Hydrogenics stack HD 15 and its operation is around 266 W. The radiator power with one fan is around 0.5 kW [153]. From the balance of plant components is pretty obvious that the compressor is not negligible in terms of power while the radiator and fan are negligible except at low load conditions. In this thesis, the cooling system is assumed well controlled around a fuel cell operating temperature and will not be considered. The compressor or airpath component is considered due to the power not being negligible with respect to the fuel cell system.

From the aeristech data provided, we assumed a variable speed to obtain power consumption from the compressor for the whole operating range of the fuel cell as shown in Fig. 2.5. Using cftool in Matlab with the simplified power consumption as function of the fuel cell current, we obtain the following fit for the compressor:

$$P_{\text{comp}} = d_1 I_{\text{fc}}^2 + d_2 I_{\text{fc}} + d_3 \quad (2.52)$$

where $d_1 = 1.22 \times 10^{-4}$, $d_2 = 3.11 \times 10^{-4}$, and $d_3 = 0.49$ are affine parameters.

2.4.2 Fuel Cell Net Efficiency for the Liquid-cooled Stack

The fuel cell system for the liquid-cooled stack model consists of the following: a fuel cell and the balance of plant component responsible for providing the airflow to the fuel cell (also known as the airpath component). The efficiency of the fuel cell is shown in Fig. 2.6 and calculated as:

$$\eta_{fc} = \frac{P_{fc} - P_{comp}}{V_0(T_{fc})I_{fc}n_{fc}n_{st}} \quad (2.53)$$

where n_{st} is the number of fuel cell stacks and P_{fc} is the power of the fuel cell and is calculated as:

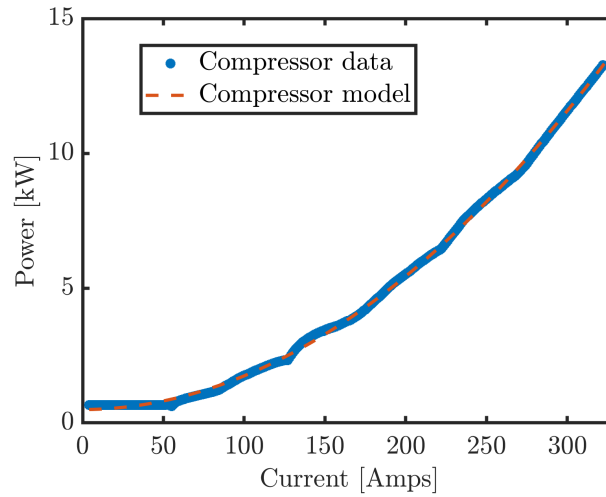


Figure 2.5: 10 kW Aeristech data and compressor model fit.

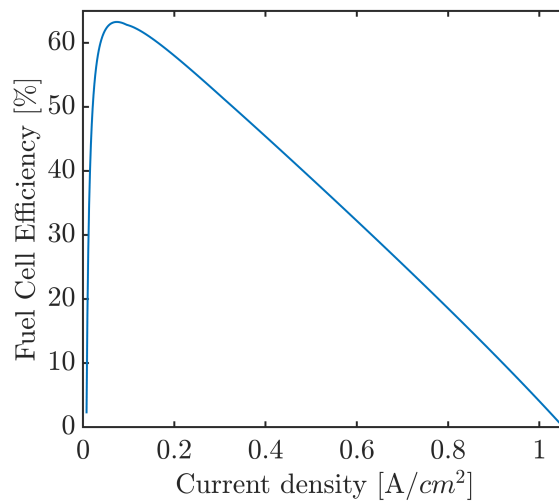


Figure 2.6: Static efficiency curve for two 15kW Hydrogenics stacks.

$$P_{fc} = I_{fc}V_{fc}n_{fc}n_{st} \quad (2.54)$$

The 15 kW Hydrogenics stack is composed of 65 cells, therefore, $n_{fc} = 65$. The polarization curve formulation (V_{fc}) can be found in section 2.2.1 and the parameters for the Hydrogenics in section 2.3.

2.5 Air-cooled and Liquid-cooled Fuel Cell Behavior

Military vehicles' power demand ranges from 300 W robots to 250 kW vehicles. The cooling system's problem with the different power military vehicles demands when they become fuel cell vehicles arises. Air-cool and open cathode systems have become popular for cooling the fuel cell in mobile applications. The popularity has been because the air used to cool the system can also supply the oxygen required for fuel cell operation [74]. By providing the air to cool the fuel cell while also operating the fuel cell, the cost for the balance of plant components reduces by merging the thermal subsystem and the reactant subsystem into one [74]. Air-cooled fuel cells tend to operate in the power ranges of 100W-5kW, and the stoichiometry ratios are around 100-150 for fuel cell operation under relatively dry conditions (around 35% relative humidity). Unfortunately, for automotive applications, the fuel cell operates around 80 kW, and liquid cooling systems are used due to the higher heat transfer coefficients compared to the air-cooled systems for the same output power [170]. Liquid-cooled fuel cells tend to operate at fully humidified conditions (around 90% relative humidity) by utilizing either internal or external humidification systems. The liquid-cooled fuel cell behavior is captured at high relative humidity by the 0-D semi-empirical fuel cell model developed in this study. Unfortunately, we are not able to capture the behavior of the air-cooled fuel cell. Therefore, an empirical model is used to capture the air-cooled fuel cell stack with such a simple physics based model, as discussed in the next section.

2.6 Empirical Model for Air-cooled Stack

The Ballard 1020 ACS air-cooled fuel cell stack (shown in Fig. 2.7) behavior will be modeled in this work. The air-cooled fuel cell under study is designed to be used on light duty applications, and it can be scaled to operate from 450 W to 3 KW [2]. The Ballard fuel cell has an open cathode and a self-humidifying membrane. The inclusion of the self-humidifying membrane reduces the cost of the fuel cell system.

The voltage of a single cell (V_{fc}) in millivolts is obtained from [7] for the Ballard 1200 ACS air-cooled stack and is given as a function of air stoichiometry (λ_{air}) and a fuel cell voltage function



Figure 2.7: Ballard 1200 ACS air-cooled fuel cell stack. Figure from [2].

influenced by temperature ($V_{fc,T}$) as:

$$V_{fc} = \left(\frac{-0.4363}{\lambda_{air} - 5} V_{fc,T} + V_{fc,T} \right) \quad (2.55)$$

where the λ_{air} is calculated as:

$$\lambda_{air} = \frac{W_{air}}{C_{air} I_{fc} n_{fc}} \quad (2.56)$$

where $C_{air} = 0.0167$ slpm/A/cell is the air consumption. The $V_{fc,T}$ in millivolts is expressed by the following equation if the fuel cell temperature is less than the optimal temperature (T_{opt}) in Celsius:

$$V_{fc,T} = [-2.954 \times 10^{-3} (T_{opt} - T_{fc})^2 + 7.315 \times 10^{-3} (T_{opt} - T_{fc})] 0.61711 I_{fc} + V_{fc,initial} \quad (2.57)$$

and if the fuel cell temperature is higher than T_{opt} is given as:

$$V_{fc,T} = [0.13575 (T_{fc} - T_{opt})^2 + 0.13032 (T_{fc} - T_{opt})] - 0.03990 I_{fc} + V_{fc,initial} \quad (2.58)$$

The optimal temperature can thus be calculated by the following equation:

$$T_{opt} = 52.204 \times (1 - e^{-0.010 I_{fc}}) + 38.095 \quad (2.59)$$

The nominal polarization curve ($V_{fc,initial}$) in millivolts can be expressed as:

$$V_{fc,initial} = -0.0019 I_{fc}^3 + 0.268 I_{fc}^2 - 14.34 I_{fc} + 973.6 \quad (2.60)$$

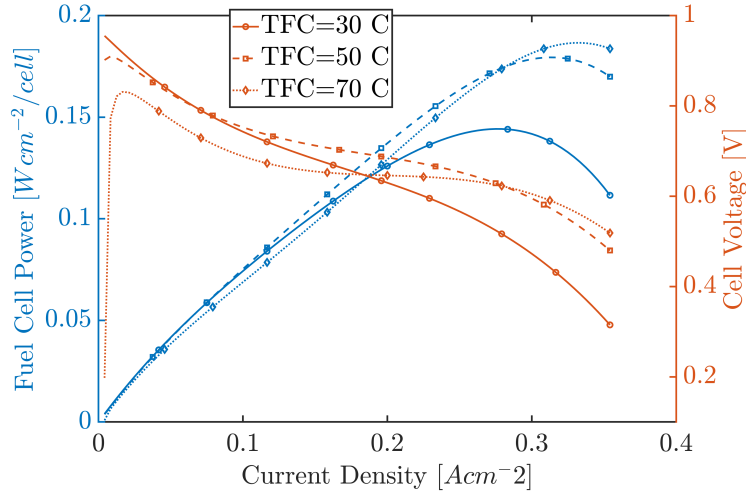


Figure 2.8: The fuel cell polarization curve and power under different temperatures for Ballard 1020 ACS air-cooled fuel cell. The voltage and power drop as the temperature increases, similarly shown in [162]. The current density is given as I_{fc}/A_{fc} where $A_{fc} = 240 \text{ cm}^2$ is the stack active area.

The fuel cell voltage and power under different fuel cell temperatures are shown in Fig. 2.8. The fuel cell voltage and power increase until 50°C , and then it drops as the temperature increases. Similar behavior is shown in [162]. There is a slight drop in voltage at low current densities at 70°C influenced by the air stoichiometry being less than 5 to maintain cell self heating, but this operation point is impractical and cannot be achieved in steady state operation. As shown in Fig. 2.8, the fuel cell model captures the temperature and airflow effect on fuel cell voltage.

2.7 Conclusion

In this chapter, a 0-D fuel cell model is used that captures the behavior of the liquid-cooled fuel cell. Voltage data for the liquid-cooled system under fixed temperature and pressures are used to obtain the polarization curve parameters. An empirical model obtained from [7] is used to model the air-cooled fuel cell stack. The fuel cell system for a Ballard 1200 ACS air-cooled stack and 15kW Hydrogenics HD 15 liquid-cooled stack is explained and modeled. For the Ballard 1200 ACS air-cooled stack, an empirical fan model is used to model this balance of plant components and how it affects fuel cell behavior through the efficiency curve and fuel cell temperature. For the 15kW Hydrogenics HD 15 liquid-cooled stack, only the compressor model is taken into account as this represents the largest power consumption. The coolant pump and radiator fan can be considered relatively constant and low loads when compared to the generated fuel cell power. In contrast, the balance of plant components significantly affects the cooling for an air-cooled stack and should

not be neglected when analyzing vehicles powered by air-cooled fuel cells. Determining at what power and energy density the liquid cooling system is cost effective or reduces the total cost of ownership will be important in the future. In the future, the same 0-D model should be used for the air cooled fuel cell (Ballard 1200 ACS) stack and validated against transient temperature and voltage data for both liquid cooled and air cooled stack. That way the same model would capture the behavior of both fuel cells and simplify the modeling analysis.

CHAPTER 3

Thermal Control Loop in an Air-cooled FC Powered Robot

3.1 Introduction

For systems smaller than 1 KW similar to the robot considered in this chapter, open cathode systems are popular since the air used for cooling can also supply the oxygen required for fuel cell operation ([74]). Merging the thermal management and the reactant supply with a single fan can reduce the BOP cost. An air-cooled open cathode architecture is ideal for portable applications owing to simple construction ([12]). This study considers a fuel cell with air-cooled open cathode and dead-ended anode. The excess cathode air supplied for cooling helps to remove excess water and consequently reduces the need for anode purging at the expense of lowering the membrane conductivity, so a balance must be achieved for optimum efficiency. The anode purge is assumed to occur according to the manufacturers' specifications ([7]) causing a drop in fuel cell efficiency ($\sim 7\%$) across all power levels in this study.

The FC system's efficiency and thermal behavior are coupled and FC systems are typically combined with batteries to help filter the load required to operate the vehicle. For obtaining the optimal power-split, one can apply Dynamic Programming (DP) to solve the minimum hydrogen consumption problem ([110]). However, the fuel cell temperature as a state in addition to the battery state of charge (SOC) increases complexity preventing applying DP over long duration cycles due to *the curse of dimensionality*. Thus, in this study, an offline pseudospectral method is considered for the augmented optimal power management problem. The work by [136] showed the importance of fuel cell temperature for fuel cell efficiency, hydrogen consumption, and battery sizing power-split strategies using a similar method. Note that the solutions of the offline optimization problem are valuable for analyzing the system's behavior and creating a benchmark goal for real-time implementation.

The PI controller is widely used in industry because of its simplicity, robust performance for both linear and nonlinear systems, and easy implementation ([141]). For instance, [88] used two

PI controllers for controlling the airflow and temperature to avoid oxygen starvation and the drop of system efficiency while extending fuel cell lifetime. [32] used PI control to maintain fuel cell current in the presence of load disturbance. In the work by [13], two PI controllers were developed to obtain the power-split by controlling the fuel cell's efficiency and the SOC of a fuel cell/battery passenger vehicle. This double PI controller reduced hydrogen consumption by 1.4% compared to a simpler PI controller that only controls the battery SOC. [150] proposed using PI control combined with heuristic control strategies such as fuzzy control to achieve the power-split and temperature regulation.

The proposed architecture consists of two control loops. One loop regulates the fuel cell's airflow through a fuel cell temperature reference where the minimum airflow is determined from the fuel cell current. The second controls the fuel cell current to track a battery SOC reference. The PI controllers track the optimal temperature setpoint based on the average power and a linear reference for the SOC.

The remainder of this study is organized as follows: Section 3.2 provides details of the models used in this study. Sections 3.3 and 3.4 present the offline optimization problem formulation for minimizing hydrogen consumption and the proposed two-PI controller approach, respectively. Section 3.5 discusses the results obtained from two approaches, followed by concluding remarks in Section 3.6.

3.2 Fuel Cell Vehicle Model for Hybrid Electric Vehicle

The vehicle under study is a small Packbot robot, shown in Fig. 3.1. The Packbot robot weighs 11 kg without batteries or manipulator arm ([156]) and requires 230 W of peak power for traction. The Packbot robot can operate only for 1 hour using the battery pack in a desert terrain containing loose sand, organic foliage, gravel, and larger stone obstacles ([76]). Therefore we propose to add a fuel cell to extend the operating time in the Packbot robot to achieve an 8 hour mission. The fuel cell vehicle (FCV) model is separated into two components: the fuel cell system and battery pack. This section will explain the modeling of the different components and how they interact with each other.

For this vehicle, two known trajectories obtained from ([15]) operating the Packbot robot on a test course in Warren, MI are used to validate the developed algorithms on different terrains. The two trajectories shown in Fig. 3.5 correspond to the Packbot operating on a flat pea gravel terrain (shown in Fig. 3.5a) and from the Packbot operating on a hill terrain (shown in Fig. 3.5b). Using the model in ([46]) an estimate of the power consumption can be obtained from the terrain type, grade, and desired speed. These cycles were chosen to observe the performance of the two PI controllers. The traction power will be supplied by both the Ballard 1200 ACS air-cooled fuel cell

and lithium-ion battery pack, and the power-split is controlled by the FC DC/DC converter. The DC/DC converter, motor, and powertrain components are assumed to be ideal and modeled based on a static efficiency curve.

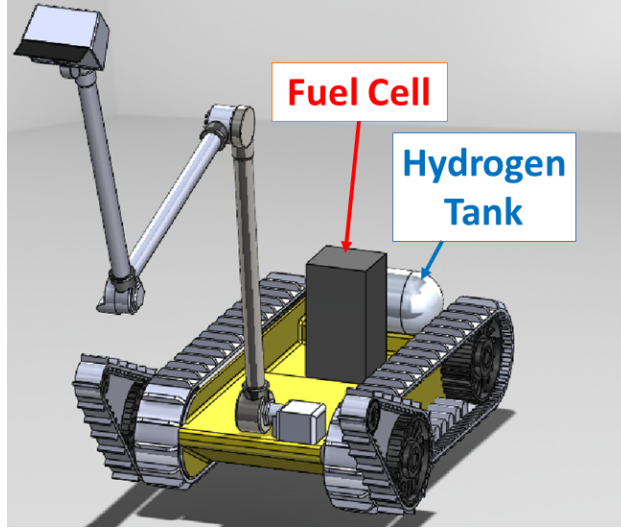


Figure 3.1: Packbot robot powered by a Ballard 1200 ACS air-cooled fuel cell and lithium-ion battery pack.

3.2.1 Battery Model Parameterized for the Packbot

The Packbot robot uses a BB2590 battery module, which consists Li-ion battery cells ([156]). A one state open circuit voltage with resistance model (OCV-R) from [136] is used to model the battery. The terminal voltage (V_b) of the battery is given as:

$$V_b = n_s(V_{ocv}(SOC) - I_b R_b) \quad (3.1)$$

where $n_s = 8$ is the number of battery modules in series for forming a stack, $R_b = 0.18 \Omega$ is the battery internal resistance, I_b is the battery current per cell, and $V_{ocv}(SOC)$ is the open circuit voltage (OCV) as a function of state of charge (SOC) given by:

$$V_{ocv}(SOC) = \sum_{i=0}^7 a_i SOC^i \quad (3.2)$$

where $a_7 = 122.30$, $a_6 = -483.10$, $a_5 = 770.03$, $a_4 = -634.56$, $a_3 = 288.65$, $a_2 = -71.74$, $a_1 = 9.52$, and $a_0 = 3$ are fitted parameters. The SOC is calculated as:

$$\frac{dSOC}{dt} = -\frac{V_{ocv}(SOC) - \sqrt{V_{ocv}^2(SOC) - \frac{4R_b P_b}{n_p n_s}}}{2R_b 3600 Q_b} \quad (3.3)$$

where $Q_b = 1.875 Ah$ is the battery capacity, $n_p = 1$ is the number of battery cells in parallel in a module, and P_b is the battery power

$$P_b = P_{load} - P_{fc} + P_{fan} \quad (3.4)$$

where P_{load} is the power demanded in Fig. 3.5, P_{fc} is the fuel cell power, and P_{fan} is the cooling fan power as discussed below.

3.2.2 Air-cooled Fuel Cell System

The fuel cell system consists of the fuel cell and the BOP that considers the fan power ([136]):

$$P_{fan} = \left(k_1 + k_2 \Delta p_{st} \frac{W_{air}}{n_{fc}} \right) n_{fc} \quad (3.5)$$

where $k_1 = 1$ and $k_2 = 10^{-3}$ are constants that capture the electrical power of the fan and the work associated with the pressure drop across the stack (Δp_{st}) that depends on the airflow rate U :

$$\Delta p_{st} = f \frac{4L}{D_h} \left(\frac{1}{2} \rho_{air} U^2 \right) \simeq 4.65U \quad (3.6)$$

where $f = 14.2$ is the friction factor for a square cross section, $L = 60$ mm is the channel length, $D_h = 0.66$ mm is the hydraulic diameter, and ρ_{air} is the air density. The approximation in (3.6) is valid for velocity of air (m/s) in the cathode channels U based on the flow rate W_{air} :

$$U = \frac{W_{air} 1000}{60 n_{fc} A_{cs}} \quad (3.7)$$

where $A_{cs} = 125 \text{mm}^2$ is the total cross sectional area of the channels. The temperature rise is given from:

$$m c_p \frac{dT_{fc}}{dt} = Q_{gen} - Q_{cool} \quad (3.8)$$

where $m c_p = 100$ is the heat capacity, Q_{gen} and Q_{cool} are the heat generated and rejected. The heat generated by the fuel cell:

$$Q_{gen} = (E_{th} - V_{fc}) I_{fc} \quad (3.9)$$

where $E_{th} = 1.2545$ V is the theoretical potential of the fuel cell using the lower heating value of hydrogen from [7]. The lower heating value is chosen since it has the latent heat capacity of water vapor, based on our assumed membrane hydration. The rejected heat is:

$$Q_{cool} = \frac{1}{h}(T_{fc} - T_{amb}) \left(\frac{W_{air}}{n_{fc}} \right) \quad (3.10)$$

where W_{air} is the airflow rate that will cool the stack (in standard liter per minute) and $h = 26$ is the heat transfer coefficient. The relationship between U and h can be found in [7] and [136]. The coefficient is approximated from the data in the operation manual for the Ballard 1020 ACS fuel cell stack. The efficiency of the fuel cell is calculated as:

$$\eta_{fc} = \frac{P_{fc} - P_{fan}}{E_{th} I_{fc} n_{fc}} \quad (3.11)$$

where I_{fc} is the fuel cell current and the power of the fuel cell is calculated as:

$$P_{fc} = I_{fc} V_{fc} n_{fc} \quad (3.12)$$

where V_{fc} is the fuel cell voltage and the number of fuel cell in a stack is $n_{fc} = 7$. The V_{fc} in millivolts is obtained from [7] and is given as a function of air stoichiometry (λ_{air}) and a fuel cell voltage function influenced by temperature ($V_{fc,T}$) as:

$$V_{fc} = \left(\frac{-0.4363}{\lambda_{air} - 5} V_{fc,T} + V_{fc,T} \right) \quad (3.13)$$

the λ_{air} is calculated as:

$$\lambda_{air} = \frac{W_{air}}{C_{air} I_{fc} n_{fc}} \quad (3.14)$$

where $C_{air} = 0.0167$ slpm/A/cell is the air consumption needed to support the reaction. The $V_{fc,T}$ in millivolts is expressed by the following equation if the fuel cell temperature is less than the optimal temperature (T_{opt}) in Celsius:

$$V_{fc,T} = [-2.954 \times 10^{-3}(T_{opt} - T_{fc})^2 + 7.315 \times 10^{-3}(T_{opt} - T_{fc})]0.61711I_{fc} + V_{fc,initial}. \quad (3.15)$$

If the fuel cell temperature is higher than T_{opt} , then:

$$V_{fc,T} = [0.13575(T_{fc} - T_{opt})^2 + 0.13032(T_{fc} - T_{opt})] - 0.03990I_{fc} + V_{fc,initial}. \quad (3.16)$$

The optimal temperature can thus be calculated by the following equation:

$$T_{\text{opt}} = 52.204 \times (1 - e^{-0.010I_{\text{fc}}}) + 38.095. \quad (3.17)$$

The nominal polarization curve ($V_{\text{fc,initial}}$) in millivolts can be expressed as:

$$V_{\text{fc,initial}} = -0.0019I_{\text{fc}}^3 + 0.268I_{\text{fc}}^2 - 14.34I_{\text{fc}} + 973.6. \quad (3.18)$$

The fuel cell voltage and power under different fuel cell temperatures are shown in Fig. 3.2. Similar behavior is shown in [162]. There is a drop in voltage at low current densities at 70°C influenced by the air stoichiometry being less than 5. The fuel cell can't operate at steady state in these conditions. As shown in Fig. 2.8, the fuel cell model captures the temperature and airflow effect on fuel cell voltage and the fan parasitic effect on the fuel cell system efficiency.

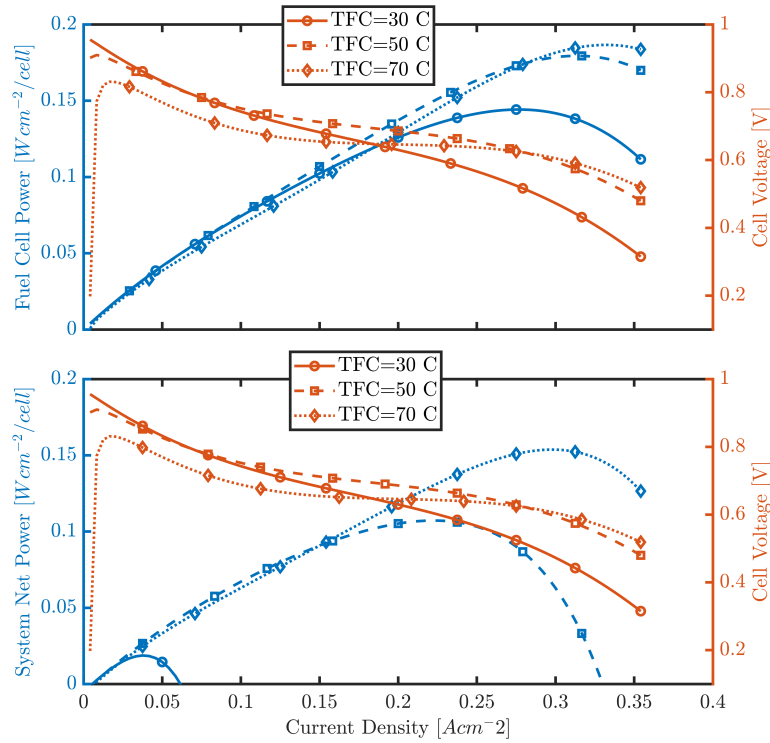


Figure 3.2: The steady state fuel cell polarization, power, and system net power for different temperatures for Ballard 1020 ACS air-cooled FC. Depending on the fuel cell temperature, the fan may impose a higher parasitic load than the fuel cell power as shown by 30°C, therefore, affecting fuel cell efficiency. The current density is given as $I_{\text{fc}}/A_{\text{fc}}$ with cell active area $A_{\text{fc}} = 240 \text{ cm}^2$.

3.3 Optimal Power-split Problem

Most control strategies only consider the fuel cell current or fuel cell power as an input and the battery SOC as a state for the optimal power-split that minimizes the hydrogen fuel consumption. These strategies typically assume that the auxiliary load is fixed and maintains the temperature around the manufacturer's optimal or recommended temperature. Depending on the fuel cell operating temperature, drying or flooding can occur, causing a voltage drop that affects the fuel cell performance and degradation ([167]), and at the same time changes the parasitic losses through the cooling fan power. Thus, this study considers the thermal management of the fuel cell system to account for the fuel cell temperature impact on the system efficiency and optimal power-split as shown in the schematic of Fig. 3.3.

The load power over the determined trip is required for the optimal control strategy. If a rough trip information is available, the load profile can be approximated with segments from a map of the grade and terrain type similar to the information from popular mobile routing applications ([25]). For this work, we assume predetermined load profiles from travelling in flat with gravel and hill terrains.

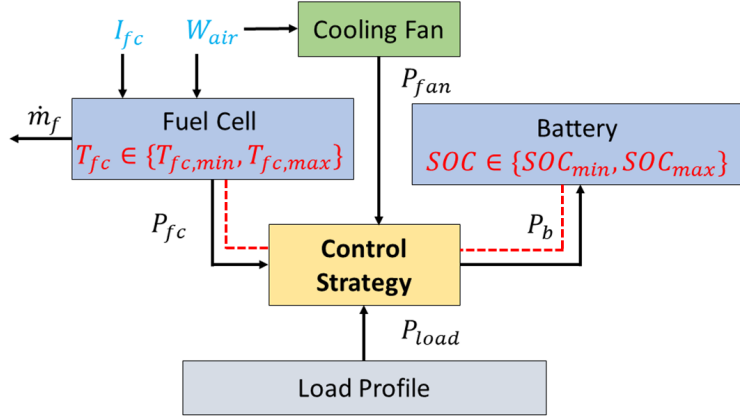


Figure 3.3: Schematic of the optimal coordination of the FC/battery power split and the thermal/cooling system. The states and control inputs are highlighted in red and blue, respectively.

The objective of power management is to minimize the total hydrogen fuel consumption without any constraint violation for the whole trip. Thus, the cost function J is:

$$J = \int \dot{m}_f dt = \int \frac{I_{fc} n_{fc} M_{H_2}}{2F} dt \quad (3.19)$$

where \dot{m}_f is the hydrogen consumption, $M_{H_2} = 2.016 \times 10^{-3}$ kg/mol is the hydrogen molar mass, and $F = 96,485$ C/mol is the Faraday's constant. The system consists of two states, state of charge ($x_1 = SOC$) and fuel cell temperature ($x_2 = T_{fc}$), and two inputs, fuel cell current ($u_1 = I_{fc}$) and

airflow ($u_2 = W_{\text{air}}$).

Constraints on the input and states are determined based on the information provided by the manufacturer ([7]). For the control inputs, the following constraints are considered:

$$4 \leq I_{\text{fc}} \leq 75 \quad (3.20)$$

$$\lambda_{\text{air},\text{min}} I_{\text{fc}} C_{\text{air}} n_{\text{fc}} \leq W_{\text{air}} \leq W_{\text{fan},\text{max}} \quad (3.21)$$

The fuel cell maximum operating current for the Ballard 1200 ACS air-cooled fuel cell stack is at 75 amps. The minimum fuel cell current is determined as 4 A to avoid high parasitic losses that degrade the total efficiency of the fuel cell system. The minimum airflow rates depend on the air stoichiometry and fuel cell current as shown in Eq. (3.21), and the maximum air flow is limited by the fan speed. The minimum airflow is determined by using $\lambda_{\text{air},\text{min}} = 50$ to avoid oxygen starvation. For the states, the following constraints are used:

$$SOC_{\text{min}} \leq SOC \leq 90 \text{ (\%)} \quad (3.22)$$

$$20 \leq T_{\text{fc}} \leq 70 \text{ (}^\circ\text{C)} \quad (3.23)$$

The fuel cell temperature is constrained between 20 – 70 °C since 70 °C is the highest temperature the fuel cell can operate without causing degradation. The upper SOC range is limited to maximize regenerative capability of the battery, while the $SOC_{\text{min}}=70\%$ so the pack can meet the peak power requirement while using a quarter of the battery size based on prior analysis ([136]).

Various optimization strategies or algorithms can be used to obtain the optimal power-split problem. A pseudospectral method is used instead of DP since the considered optimal control problem is more complex than a typical power-split problem without consideration of thermal management (2 states and 2 control inputs vs. 1 state and 1 control). [136] demonstrated the quality of the optimal solutions and reduced computation from hours to 100 s. [136] also demonstrated the improvement of adding the thermal management (two states and two input formulation) compared to Dynamic Programming (1 state vs. one input) and a rule-based strategy. The problem is formulated and implemented using the MATLAB-based optimal control software, Gauss Pseudospectral Optimization Software (GPOPS-II) ([113]). The limitation of the pseudospectral methodology is that it gives a local solution instead of a global solution. On top of that, the methodology is sensitive to the initial conditions and guesses for the trajectory of the states and inputs. Despite reducing the computational time to ~ 30 minutes, we still need a fast computational method for future real-time implementation. Therefore, a reference-based control strategy is used that takes around 7 seconds (300x real-time) to solve on a 9th Generation Intel Core i7-9750H (4.5 GHz) CPU using MATLAB.

3.4 Reference-based Control Strategy

As discussed earlier, solving the optimal control problem in real-time is challenging ([36]), and hence for real-time implementation, this study develops two PI controllers, as shown in Fig. 3.4: one controls the fuel cell’s airflow while the other regulates the fuel cell current. Controlling the fuel cell current is equivalent to managing the power-split, since the remaining power is drawn from the battery. The PI controller for the airflow control consists of the following equations in discrete time:

$$W_{air}^*(k-1) = K_p e(k-1) + K_i q(k-1) \quad (3.24)$$

$$W_{air}(k-1) = \max(W_{air}^{min}, W_{air}^*(k-1)) \quad (3.25)$$

$$e(k-1) = T_{fc,ref}(k-1) - T_{fc}(k-1) \quad (3.26)$$

$$q(k) = K_a (W_{air}(k-1) - W_{air}^*(k-1)) \Delta t + e(k-1) \Delta t + q(k-1) \quad (3.27)$$

where K_p is the proportional gain, K_i is the integral gain, K_a is the saturation or anti-windup gain, $u = W_{air}$ is the input, W_{air}^* is the airflow without applying the lower saturation limit value, and $\Delta t = 0.26$ s is the time step. Note that q is the integral controller state. The anti-windup provides fast temperature regulation once the system warms and flows above the minimum (also known as the saturated value, the same as the minimum airflow in the optimal control strategy). The $T_{fc,ref}$ denotes a reference temperature setpoint.

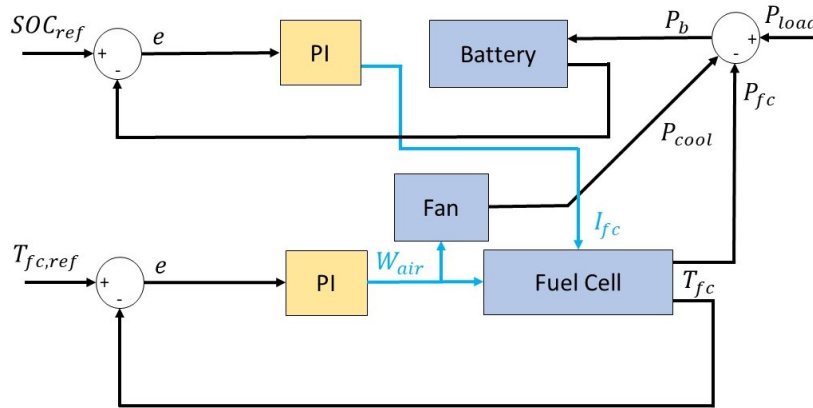


Figure 3.4: Block diagram of the reference-based FC/battery power-split and the thermal/cooling system. The yellow box denotes the PI controller with the anti-windup.

The fuel cell current needs to be determined to obtain the power-split of the robot, another PI

controller is formulated as follows to control the fuel cell current:

$$I_{fc}^*(k-1) = K_{p,soc}e_{soc}(k-1) + K_{i,soc}p(k-1) \quad (3.28)$$

$$I_{fc}(k-1) = \max(I_{fc}^{\min}, I_{fc}^*(k-1)) \quad (3.29)$$

$$e_{soc}(k-1) = SOC_{ref}(k-1) - SOC(k-1) \quad (3.30)$$

$$p(k) = K_{a,soc}(I_{fc}(k-1) - I_{fc}^*(k-1))\Delta t + e_{soc}(k-1)\Delta t + p(k-1) \quad (3.31)$$

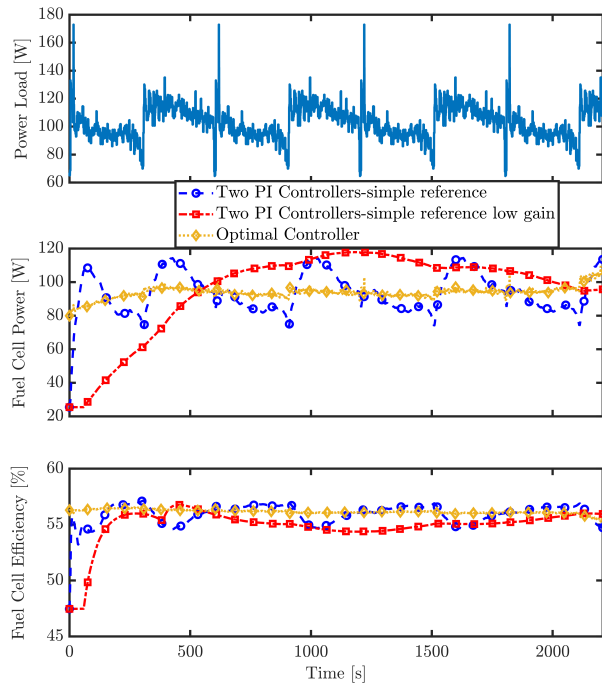
where $K_{p,soc}$ is the proportional gain, $K_{i,soc}$ is the integral gain, $K_{a,soc}$ is the saturation or anti-windup gain, $u = I_{fc}$ is the input, I_{fc}^* and is the fuel cell current without applying the lower saturation limit value. Note that p is the integral controller state. The anti-windup is included to provide fast fuel cell current regulation once the system starts operation. Currents above the minimum (the saturated value, the same as the minimum current in the optimal control strategy) are required. The SOC_{ref} denotes a reference SOC setpoint.

3.5 Results

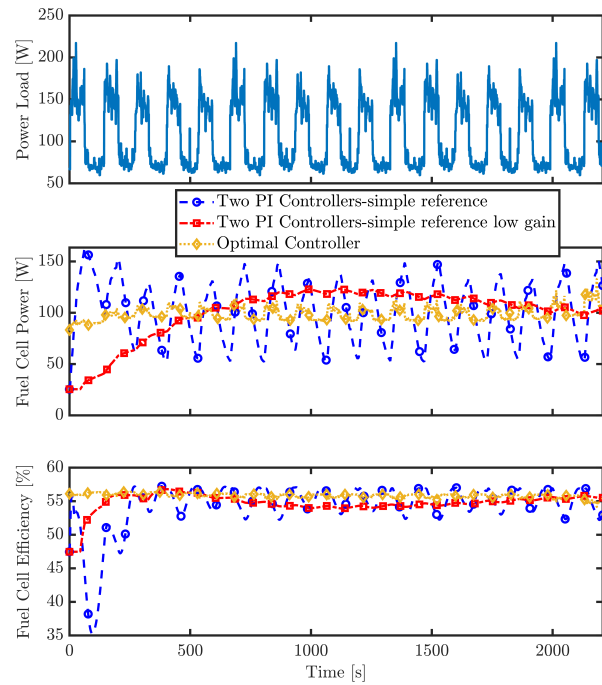
Table 3.1: Hydrogen Consumption & Root Mean Square Error (RMSE)

Flat pea gravel terrain profile shown in Fig. 3.5a			
Methodology	Hydrogen Consumption (g)	Temperature RMSE (°C)	Current RMSE (A)
Simple ref.	2.75	0.79	2.29
Simple ref. low gain	2.84	3.90	4.71
Optimal Controller	2.74	-	-
Hill terrain profile shown in Fig. 3.5b			
Simple ref.	3.03	1.53	6.18
Simple ref. low gain	2.99	4.01	4.91
Optimal Controller	2.91	-	-

The two load profiles shown in Fig. 3.5 will be analyzed to compare the PI controller with a simple linear reference SOC trajectory and constant temperature setpoint to the offline optimal results for both the temperature and the SOC trajectories. The reference temperature setpoint was chosen as 51°C and is fixed and equal to the value that the optimal controller selected to operate for the majority of the time. The reference SOC setpoint is a linear trajectory from the initial state of charge (90%) to the final $SOC_{min} = 70\%$. This small battery range is chosen to conveniently emulate small battery size without resizing the actual battery.

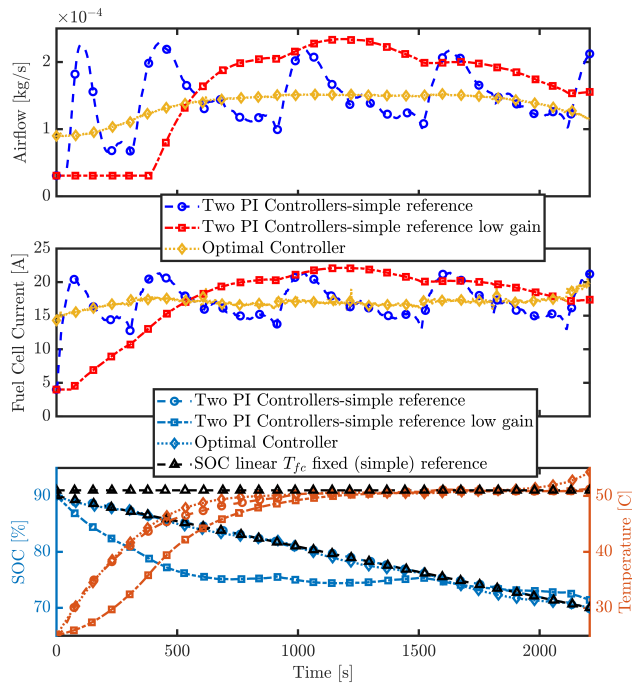


(a) Flat pea gravel terrain results.

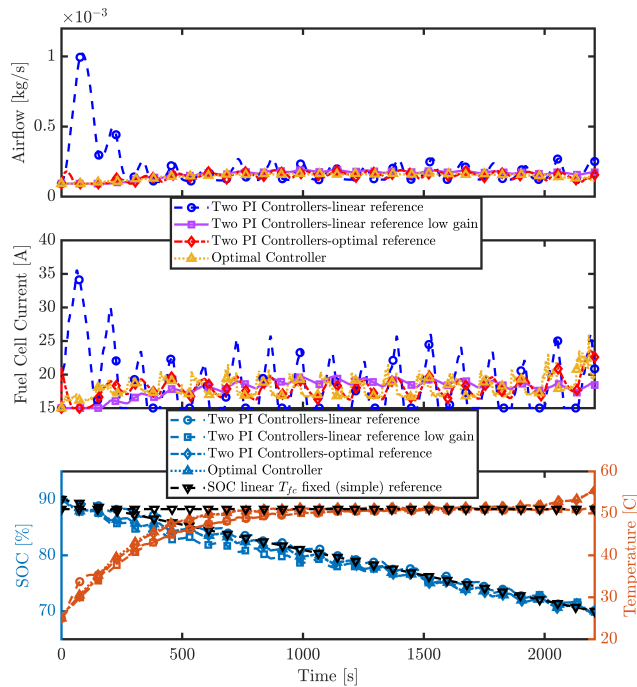


(b) Hill terrain results.

Figure 3.5: Comparison of fuel cell power and efficiency between the results obtained with offline optimal control strategy and the two PI controllers for the two terrain cases considered in this study (flat pea gravel terrain 3.5a, and hill terrain 3.5b).



(a) Flat pea gravel terrain results.



(b) Hill terrain results.

Figure 3.6: Comparison of fuel cell current, airflow, SOC, and fuel cell temperature results from offline optimal control strategy and the two PI controllers for the flat pea gravel and hill terrain case considered in this study.

Table 3.2: PI controller Gains

Airflow Control			Current Control		
Simple reference					
K_p	K_i	K_a	$K_{p,soc}$	$K_{i,soc}$	$K_{a,soc}$
-30	-0.1	-5	1500	30	0.1
Simple reference low gain					
K_p	K_i	K_a	$K_{p,soc}$	$K_{i,soc}$	$K_{a,soc}$
-30	-0.1	-5	100	0.2	0.1

The first set of gains (Table 3.2) was chosen to track well $T_{fc,ref}$ achieving a RMSE=1.53 as shown in Table 3.1 while maintaining similar hydrogen consumption with the optimal controller for the flat gravel terrain. One more set of PI gains is also chosen to demonstrate that less accurate temp and SOC tracking causes higher hydrogen consumption as summarized in Table 3.1 for the flat terrain. For the hilly terrain the low gain PI controller performs better in terms of hydrogen consumption due to the lower RMSE in current as shown in Table 3.1. Therefore, the PI controller gains tuning will be further studied. The benefit of the low gain PI controller is the smoother airflow which might cause less degradation to the FC and the fan. Degradation will be considered in future work.

3.6 Conclusion

In this study, two PI control strategies are designed to realize an offline optimal controller for a fuel cell hybrid electric vehicle with an integrated thermal management and air supply BOP system. One PI controller controls the airflow through fuel cell temperature reference, and the other controls the fuel cell current to satisfy a prescribed SOC reference. A pseudospectral methodology from Matlab called GPOPS is used to obtain the optimal power split for the hybrid electric vehicle. Also, setpoints are introduced for the two PI controllers after achieving the power split and the optimal trajectories for the inputs and states from the optimal control strategy. The two PI controllers' performance using the simple reference derived from the offline optimal results can achieve 96% of the fuel savings of the optimum hydrogen consumption with full preview information. Despite the achievement, the set of gains need to be further studied to avoid fluctuations in the fuel cell current and avoid degradation [78]. In the future, adaptive reference control [47] should be used and validated with real-time data from the hybrid electric vehicle to verify that appropriate gains are used for a plethora of duty cycles. Fuel cell degradation should be also considered to analyze the current fluctuations on fuel cell lifetime.

CHAPTER 4

Sizing Effect on Power Split of Medium-size Fuel-cell Military Vehicle

One of the barriers in terms of reducing the fuel cell vehicle cost is through the reduction of the balance of plant components [60] that accounts around 50% at low volume and 25% at high volume [62]. For automotive systems, in which an 80-kW fuel cell system is typically considered [137], liquid cooling systems are recommended to cool the fuel cell [79], [176], [172], [174]. Besides the cooling system chosen, the energy management of the fuel cell vehicle needs to be determined. Dynamic programming is used for the energy management of fuel cell hybrid electric vehicles by minimizing the hydrogen consumption given a battery energy capacity and impedance (resistance). Note here that for most fuel cell vehicles, the energy management corresponds to a power split between the fuel cell and the battery, while the battery charge is sustained. In this work we consider the battery depletion and let the optimal controller define if the operation is a charge depleting, sustaining, or blending. While hydrogen consumption defines the operation cost [35], the capital cost [40] is influenced by the battery sizing and is considered in the following sections.

Although an optimal power split problem can be solved by DP, its computational requirements can be prohibitively high for long drive cycles (longer trips than their battery energy). To resolve the issue of solving an optimal control problem for long and not well defined drive cycles, an equivalent consumption minimization strategy (ECMS) is developed. Another variant of ECMS is adaptive ECMS [110] where the equivalence factor is updated at each time step to track a reference SOC trajectory of a battery [24] in the form of PI controller [42] or through power configuration parameters [163], showing the promise of this methodology for real-time implementation.

In this chapter, two approaches to power split including DP and ECMS are considered and compared using a liquid cooling system capable of regulating a fixed 65°C condition with low parasitic losses for a plug-in hybrid fuel cell medium-sized military vehicle over three difference drive cycles. For performance comparison, first, the size of battery and fuel cell are fixed. Then, different battery sizes and chemistries are considered to study their impacts on fuel consumption and, consequently, on the control strategies.

The remainder of the chapter is organized as follows: Section 4.1 provides details of the models used in this study. In sections 4.2 and 4.3, the optimal control problem formulation for the minimum hydrogen consumption using DP and ECMS are presented. Section 4.4 discusses the results obtained from the two approaches, followed by the different battery sizing combinations over the hilly terrain cycle and LFP and NMC as Li-ion battery chemistries in Section 4.5. Section 4.7 provides the concluding remarks.

4.1 Simulation Models

Table 4.1: Medium size military vehicle performance requirements.

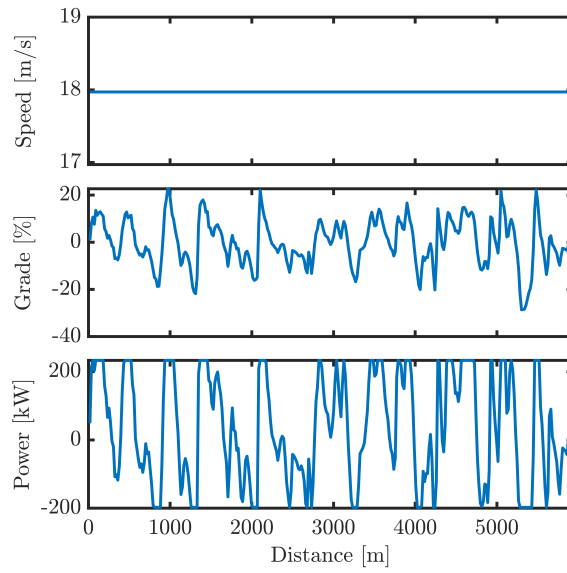
Vehicle Performance Requirements	Value
Maximum grade (%)	60
Maximum acceleration	0-50 <i>mph</i> in 26 <i>s</i>
Average speed required (<i>mph</i>)	25
Maximum speed (<i>mph</i>)	70

The vehicle used in this study is a medium-size military vehicle, with the vehicle specifications given in Table 4.2 and the vehicle performance requirements in Table 4.1. These specifications and performance requirements were provided by the Ground Vehicle Systems Center (GVSC). In vehicle simulation, three operating scenarios are considered: two driving cycles and one power profile. For the driving cycles, the vehicle’s velocity and grade profiles are obtained from the hilly terrain drive cycle [132] and a Highway driving [107], shown in Figs. 4.1a and 4.1b, respectively. For the power profile, a silent-watch operation followed by firing of an electrothermal-chemical (ETC) gun in [39] is combined with the resulting power trajectories from the hilly terrain drive cycle and the Munson cycles [92] (see Fig. 4.2).

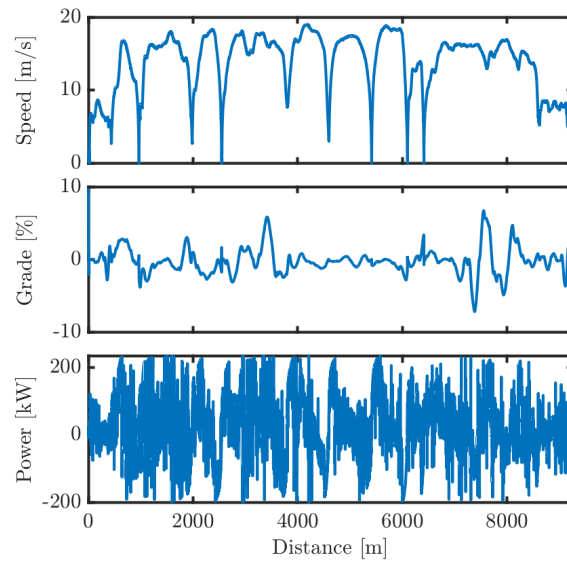
Table 4.2: Medium size military vehicle specifications.

Vehicle Specifications	Value
Weight (<i>lbs</i>)	24500
Frontal Area (<i>ft</i> ²)	58.7
Wheel/Sprocket Radius (<i>in</i>)	20
Engine Displacement Volume (<i>L</i>)	7
Engine, motor power limits (<i>kW</i>)	270

It is noted that the hilly terrain drive cycle is chosen since it represents an aggressive driver on a hilly terrain [10]. On the other hand, the highway driving is chosen to investigate whether



(a) Hilly terrain drive cycle corresponds to a trip Energy of 38.43 kWh, Root Mean Square power (RMS) of 158 kW and peak power of 230kW.



(b) Highway driving cycle requires a trip Energy of 16.44 kWh, Root Mean Square (RMS) power of 78 kW, and Peak power of 230kW.

Figure 4.1: Speed and grade profile from the highway driving and hilly terrain cycle that will be used for the power split analysis of the medium-size vehicle.

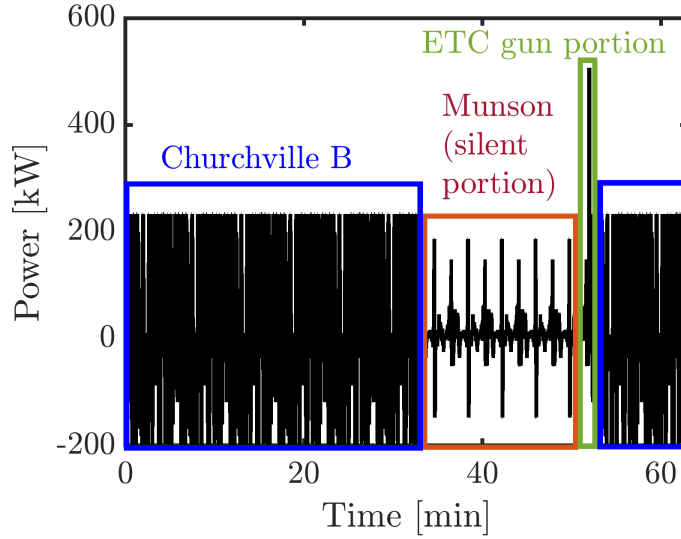


Figure 4.2: Power from silent watch profile that will be used for the power split analysis of the medium-size vehicle. Silent watch profile requires energy of 29.51 kWh and has a power variability of Root Mean Square (RMS) 135 kW with a peak power of 550kW.

the power split strategies studied in this work can be applied to both military and commercial vehicles. The silent watch profile with the ETC gun firing is chosen to study the effect of the gun shooting on the power split of the vehicle. The hilly terrain drive cycle and highway driving cycles are repeated until the drive cycles reach 1 hour of vehicle operation to obtain more representative working conditions on the vehicle.

4.1.1 Vehicle and Motor Model

The main focus of this study is on power split or energy management, and hence longitudinal dynamics are only considered. The vehicle dynamics are captured by the following force equations:

$$F_a = Ma, \quad (4.1)$$

$$F_g = Mg \sin \left(\tan^{-1} \left(\frac{\beta}{100} \right) \right), \quad (4.2)$$

$$F_d = A + Bv + Cv^2, \quad (4.3)$$

where F_a is the acceleration force, F_g is the gradient force, and F_d is the resistance drag forces. The inputs are: a , which is the vehicle's acceleration, β the gradient percentage, and v is the vehicle velocity. The total mass of the vehicle (M) is calculated as:

$$M = n_{st}m_{fc} + n_s n_p m_b + m_v \quad (4.4)$$

where $m_{fc} = 55$ (kg) is the weight of a fuel cell stack, $m_b = 0.27$ (kg) is the weight of a single battery cell and m_v is the weight of the vehicle in kg. The motor power P_m and wheel power P_{wheels} are determined from the following equations:

$$P_{wheels} = (F_a + F_g + F_d)v \quad (4.5)$$

$$\omega_m = \frac{vGR_{fd}}{r_{tire}} \quad (4.6)$$

$$\tau = \frac{(F_a + F_g + F_d)r_{tire}}{GR_{fd}\eta_{fd}} \quad (4.7)$$

$$\tau_m = \begin{cases} \min(\phi_1(\omega_w, \tau)) & \text{if } \tau \geq 0 \\ \max(\phi_2(\omega_w, \tau)) & \text{otherwise} \end{cases} \quad (4.8)$$

$$P_m = (o + b\omega_m + c\omega_m^2) + (d + e\omega_m + f\omega_m^2 + q\omega_m^3)\tau_m + (h + k\omega_m + l\omega_m^2)\tau_m^2 \quad (4.9)$$

where ω_m is the motor speed, τ is the wheel torque, τ_m is the motor torque, P_m is the electric power of the motor, and P_{wheels} is the wheel power. The functions ϕ_1 and ϕ_2 determine the maximum and minimum torques allowed by the motor.

Table 4.3: Vehicle and motor model parameters for medium size military vehicle.

Name	Parameter	Value
Vehicle Weight (kg)	M_v	11113.013
Static Road Load (N)	A	353.76
Dynamic Road Load (N/(m/s))	B	1.77
Aerodynamic Load (N/(m/s) ²)	C	2.67
Final Drive Gear Ratio	GR_{fd}	12
Tire Radius (m)	r_{tire}	0.51
Final Drive Efficiency	η_{fd}	0.96
motor parameters	o	1265
motor parameters	b	6.25
motor parameters	c	7.61×10^{-3}
motor parameters	d	-8.22×10^{-2}
motor parameters	e	1
motor parameters	f	-3.60×10^{-6}
motor parameters	q	3.51×10^{-9}
motor parameters	h	3.714×10^{-2}
motor parameters	k	-2.96×10^{-5}
motor parameters	l	1.34×10^{-7}

The electric power of the motor (P_m) is an empirical function of motor speed and torque ob-

tained from the following equation:

$$P_m = P_{\text{mech}} + P_{\text{loss}} \quad (4.10)$$

where P_{mech} is the mechanical power and P_{loss} is the power loss by the motor. The mechanical power and power loss are given by:

$$P_{\text{mech}} = \frac{\pi \omega_m \tau_m}{30} \quad (4.11)$$

$$P_{\text{loss}} = \left(\frac{100}{\eta_m(\omega_m, |\tau_m|)} - 1 \right) |P_{\text{mech}}| \quad (4.12)$$

where η_m is the efficiency of the motor in percentage and is shown in Fig. 4.3, the vehicle and motor model parameters are shown in Table 4.3.

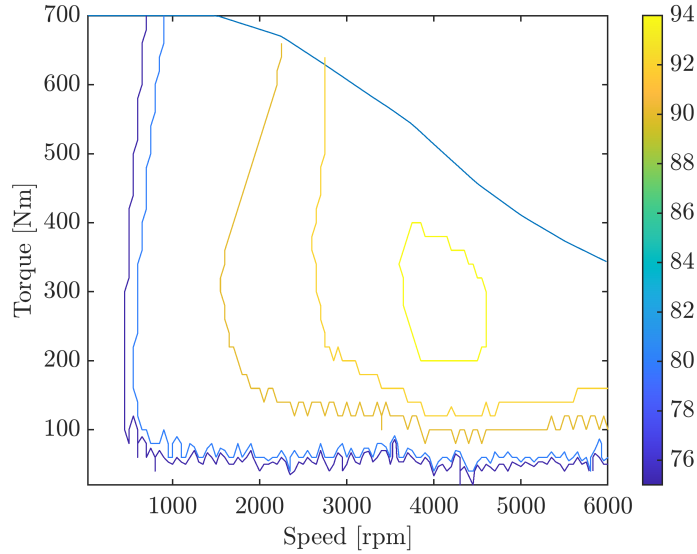


Figure 4.3: Motor UQM HD220 Efficiency Map used to obtain our load profile.

4.1.2 Battery Models for NMC and LFP Chemistry

As previously describe in Chapter 3, a simple equivalent circuit model is used to capture the battery's behavior. Two battery chemistries will be modeled in this study. One of the battery chemistries that is being modeled is the NMC with a rated power of approximately 450 W per cell. The second battery chemistry is the LFP with a rated power of approximately 840 W per cell. The following battery model is used for both chemistries except for the OCV-SOC function and battery

internal resistance values. The terminal voltage of the battery is given as:

$$V_t = V_{oc} - I_b R_b \quad (4.13)$$

where R_b is the battery internal resistance, I_b is the battery current per cell, and V_{oc} is the open circuit voltage (OCV). Typically, V_{oc} and R_b are dependent on the state of charge (SOC) of the battery, as shown in Fig. 4.4 for the NMC chemistry. A lookup table was used for representing the OCV of the NMC chemistry. For the LFP the OCV is given as:

$$V_{oc}(z) = V_0 + d(1 - \exp(-fz)) + h \left(1 - \exp\left(-\frac{-k}{1-z}\right) \right) + gz + \sum_{i=1}^3 a_{v,i} \arctan\left(-\frac{z - b_{v,i}}{c_{v,i}}\right), \quad (4.14)$$

where V_0 , g , d , f , h , k , $a_{v,i}$, $b_{v,i}$, and $c_{v,i}$ are tuned parameters found in Appendix A.4. The SOC dynamics are represented by:

$$\dot{\text{SOC}}_b = -\frac{I_b}{Q_b}, \quad (4.15)$$

where $Q_b = n_p 5 \text{ Ah}$ is the battery's pack capacity and $n_p = 10$ is the number of battery cells in parallel in a module.

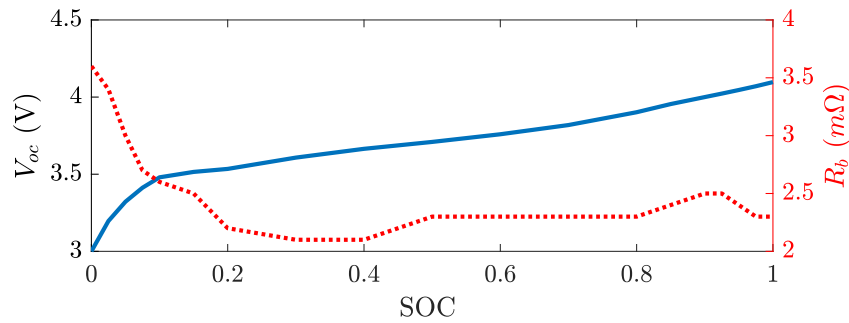


Figure 4.4: The open-circuit voltage and internal resistance of the battery as a function of battery SOC.

The battery current I_b is given as:

$$I_b = \frac{V_{oc} - \sqrt{V_{oc}^2 - 4R_p P_b}}{2R_b}. \quad (4.16)$$

where P_b is the battery power, $R_p = \frac{n_s}{n_p} R_b$ is the resistance of the battery pack, and $n_s = 150$ is the number of battery modules in series for forming a stack. The battery current formulation assumes that the battery power is the input to the battery system. The P_b is calculated as:

$$P_b = P_m - P_{fc} + P_{comp} \quad (4.17)$$

where P_m is the power demanded from the vehicle, P_{fc} is the power of the liquid-cooled 15 kW Hydrogenics HD15 stack, and P_{comp} is the power of the compressor (balance of plant component used to provide the air to the fuel cell). In our vehicle formulation, the mechanical power is equal to the load power ($P_m = P_{load}$).

4.1.3 Fuel Cell Parameters for Liquid Cooled Operation

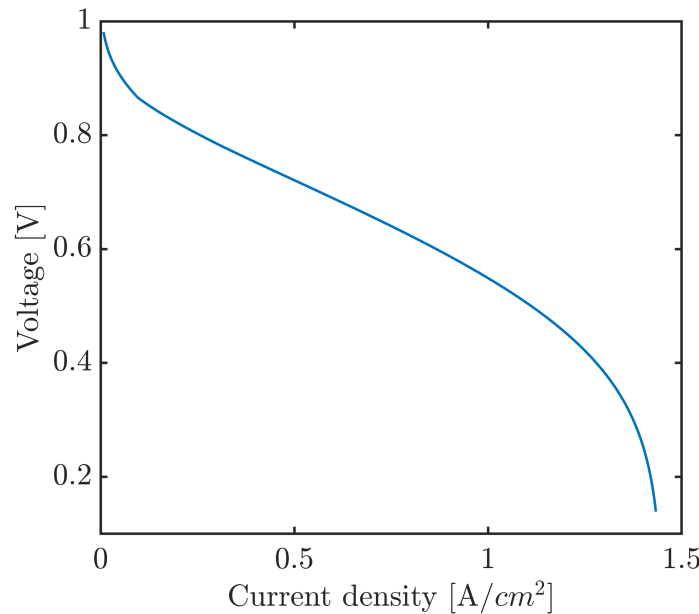


Figure 4.5: Voltage or polarization curve at $65^\circ C$ used for our fuel cell system analysis.

In this study, a liquid-cooled Proton Exchange Membrane Fuel-cell system is considered based on the model of a 15 kW Hydrogenics HD15 stack. A parasitic load for air supply (compressor) is considered, and hence the compressor power is modeled as:

$$P_{comp} = d_1 I_{fc}^2 + d_2 I_{fc} + d_3 \quad (4.18)$$

where $d_1 = 1.22 \times 10^{-4}$, $d_2 = 3.11 \times 10^{-4}$, and $d_3 = 0.49$ are affine parameters and I_{fc} is the fuel

cell current. The efficiency of the fuel cell is calculated as:

$$\eta_{fc} = \frac{P_{fc} - P_{comp}}{V_0(T_{fc})I_{fc}n_{fc}n_{st}} \quad (4.19)$$

where $V_0(T_{fc}) = 1.256 - 2.26 \times 10^{-4}T_{fc}$ is the fuel cell's theoretical potential given as a function of fuel cell temperature, n_{st} is the number of fuel cell stacks, and P_{fc} is the power of the fuel cell calculated as:

$$P_{fc} = I_{fc}V_{fc}n_{fc}n_{st} \quad (4.20)$$

where n_{fc} is the number of fuel cell in a stack and V_{fc} is the fuel cell voltage given by:

$$V_{fc} = V_0(T_{fc}) + \frac{RT_{fc}}{nF} \log \left(\frac{p_{H_2} \sqrt{p_{O_2}}}{p_v} \right) - \frac{RT_{fc}}{F} \operatorname{asinh} \left(\frac{i_{loss} + i}{2i_{oc}} \right) - iR_{mb} + B_c \log \left(1 - \frac{i}{i_{max}} \right) \quad (4.21)$$

where the universal gas constant is $R=8.3145$ J/molK, $F=96,485$ C/mol is the Faraday constant, and $n=2$ is the number of moles of hydrogen. The current density loss due to hydrogen crossover is given by $i_{loss} = 8.72$ mA/cm², $i_{oc} = 0.17$ μ A /cm² is the exchange current density, $R_{mb} = 0.1548$ Ω cm² is the membrane resistance of the fuel cell, $B_c = 0.1028$ V is the mass transport loss coefficient, and $i_{max} = 1.4508$ A/cm² is the limiting current density.

The fuel cell polarization curve is a function of temperature, pressure, and relative humidity. For this study, a constant fuel cell temperature of 65°C is assumed for the fuel cell temperature and under fully humidified conditions (relative humidity is 90%). The polarization curve or voltage (V_{fc}) under these conditions is shown in Fig. 4.5 and used for this study. The 15 kW Hydrogenics stack is composed of 65 cells ($n_{fc}=65$) and 12 stacks ($n_{st}=12$). The number of fuel cell stacks was chosen to supply the drive cycle's average power and the battery pack to supply the drive cycle's peak power. The total power of the fuel cell stack is, therefore, 180 kW. The compressor power is around 10 kW, and it's scaled to operate for two fuel cell stacks meaning one compressor provides the airflow to two fuel cell stacks. From the power load of our chosen fuel cell stack, it is evident that the cooling system should be liquid-cooled. Therefore, the assumption of a constant fuel cell temperature of 65°C is valid since the cooling system for the liquid-cooled fuel cell system usually operates at low load conditions than the whole fuel cell system. Therefore, the cooling system can be neglected [79], [176], [172], [174].

4.2 Dynamic Programming (DP) Formulation

Dynamic Programming (DP) is an algorithmic technique that finds the optimal control sequence that minimizes a given cost function in consideration of constraints. In this case, hydrogen consumption is the given cost function. A desired final battery state of charge, fuel cell current, and state of charge ranges are used as constraints. Since the optimal decision at every instant depends on the future demands and constraints, DP starts from the last step and propagates backward, assuming complete knowledge of the entire load trajectory. One input (the fuel cell current) and one state (battery SOC) are considered for the system, and the cost function to be minimized is the hydrogen consumption given as:

$$J = \int \dot{m}_f = \frac{I_{fc} n_{fc} M_{H_2}}{2F} \quad (4.22)$$

where J is the cost function, \dot{m}_f is the hydrogen consumption, $M_{H_2} = 2.016 \times 10^{-3}$ kg/mol is the hydrogen molar mass. A schematic of the power flow in the system is shown in Fig. 4.6. The input and state are constrained to avoid fuel cell and battery degradation as follow:

$$I_{fc,\min} \leq I_{fc} \leq I_{fc,\max} \quad (4.23)$$

$$SOC_{\min} \leq SOC \leq SOC_{\max} \quad (4.24)$$

where $I_{fc,\min}=4$ is the minimum fuel cell current, $I_{fc,\max} = 425$ is the maximum fuel cell current, $SOC_{\min} = 24\%$ is the minimum battery SOC, and $SOC_{\max} = 95\%$ is the maximum battery SOC. The maximum fuel cell current is determined from the maximum operating current provided by the manufacturer [4]. The minimum fuel cell current is determined to avoid high parasitic losses that degrade the total efficiency of the fuel cell system. The maximum battery SOC is chosen to provide charging above the usual limit of 80% for a plug-in vehicle without exceeding the 100% state of charge limit. The minimum battery SOC is determined close to the usual minimum limit of a plug-in vehicle (which is 20%). The initial SOC is chosen as 85%. The solution to the DP problem is numerically obtained using the **dpm** function implemented in the MATLAB environment [142].

The dynamic equations with state and control variables need to be discretized in a time domain to solve the optimal control problems using DP. The level of discretization affects the accuracy of a solution and the computation time; for instance, coarse discretization could result in fast computation but large numerical errors. Therefore, step sizes for the discretization should be carefully chosen. The level of discretization for time, fuel cell current, and battery state of charge for this study is provided in Table 4.4.

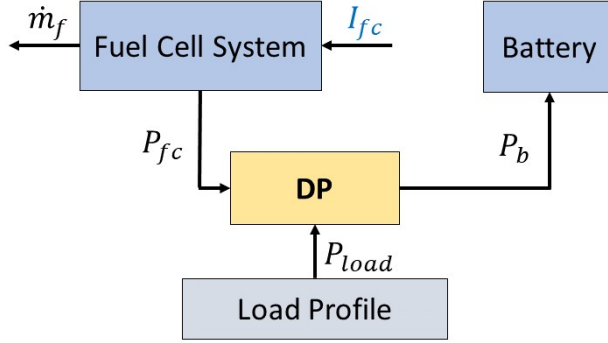


Figure 4.6: Dynamic Programming formulation for medium size military vehicle. The dynamic programming (DP) formulation uses fuel cell current as an input (I_{fc}) and state of charge (SOC) as a state. DP minimizes the cost function (\dot{m}_f).

Table 4.4: Discretization of optimization variables in Dynamic Programming

Cycle	State	Symbol	Value	Unit
Hilly terrain cycle & Silent watch	Time	Δt	1	s
	Fuel cell current	ΔI_{fc}	2.81	A
	SOC	ΔSOC	1.5×10^{-4}	-
Highway driving	Time	Δt	0.1	s
	Fuel cell current	ΔI_{fc}	2.81	A
	SOC	ΔSOC	1.5×10^{-4}	-

4.3 Equivalent Consumption Minimization Strategy

Even though DP gives the optimal solution, its computational time exponentially increases as the number of states increases. The equivalent consumption minimization strategy (ECMS) is a heuristic method that reduces the global minimization problem into an instantaneous minimization problem. It is solved at each instant, only using a weighted value of the electric energy and the actual energy flow in the powertrain, making it ideal for real-life implementation. An ECMS formulation and an explanation of how it can be derived from another optimal control strategy (PMP) can be found [110]. The instantaneous formulation from [110] is implemented, and the cost function that needs to be minimized is:

$$\dot{m}_{f,\text{eqv}}(t) = \dot{m}_f(t) + \frac{s}{Q_{\text{lhv}}} P_b \quad (4.25)$$

where $\dot{m}_{f,\text{eqv}}(t)$ is the instantaneous equivalent consumption, $\dot{m}_f(t)$ is the hydrogen consumption given in Eq. (4.22), $Q_{\text{lhv}} = 120 \text{ kJ/g}$ is the lower heating value of hydrogen, P_b is the battery power given by Eq. (4.17), and s is the equivalence factor. By varying s , load power (P_{load}), fuel

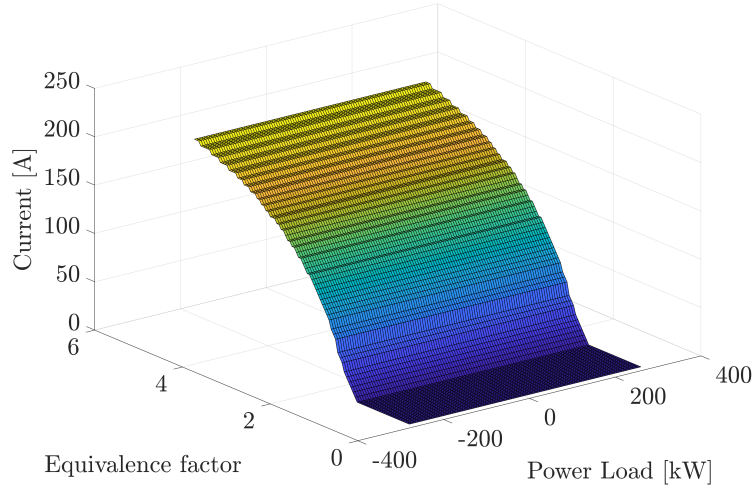


Figure 4.7: Lookup table of fuel cell current as a function of equivalence factor and load power obtained from the equivalence factor minimization strategy.

cell current (I_{fc}) and solving Eq. (4.25), the following lookup table for the fuel cell current is obtained as shown in Fig. 4.7. With a chosen constant s and load power known, the fuel cell current for the power split strategy can be obtained.

4.4 DP and ECMS Performance Comparison

Table 4.5: Chosen equivalence factors for the three drive cycles

Cycle	Equivalence factor value
Hilly terrain cycle	1.66
Highway driving	1.32
Silent watch profile	1.56

To compare the two developed control strategies the following parameters will be calculated

and compared:

$$\text{Stack net efficiency} = \eta_{fc} = \frac{\int (P_{fc} - P_{comp})dt}{\int (V_0(T_{fc})(I_{fc}n_{fc}n_{st}))dt} \times 100 \quad (4.26)$$

$$\text{Trip energy} = \int (P_m)dt \quad (4.27)$$

$$\text{Battery energy} = \int (P_b)dt \quad (4.28)$$

$$\text{Fuel cell energy} = \int (P_{fc} - P_{comp})dt \quad (4.29)$$

$$\text{Battery to trip energy ratio} = \frac{\text{Battery energy}}{\text{Trip energy}} \quad (4.30)$$

$$\text{Battery energy loss} = \int (R_p I_b^2)dt \quad (4.31)$$

For the battery, we assume the efficiency is equal to 1 for both charging and discharging cases. The chosen values of s for the three operating scenarios are shown in Table 4.5. It is noted that the chosen equivalence factors are determined such that the battery SOC at the end of each cycle matches the final SOC obtained from the DP for a fair comparison in terms of fuel consumption for both control strategies. The NMC chemistry is considered in this analysis with the behavior shown in Fig. 4.4.

Table 4.6: DP and ECMS performance comparison for all drive cycles

Cycle Parameters	Churchville B		Highway driving		Silent watch	
	DP	ECMS	DP	ECMS	DP	ECMS
Trip Energy (kWh)	38.43	38.43	16.44	16.44	29.51	29.51
Battery Energy (kWh)	14.42	14.29	16.36	16.36	14.78	14.68
Fuel Cell Energy (kWh)	24.01	24.13	0.08	0.08	14.32	14.38
Battery to Trip Energy ratio	0.38	0.37	1	1	0.50	0.51
Hydrogen Consumption (kg)	1.21	1.22	0.12	0.12	0.74	0.75
Stack Net Efficiency (%)	63.11	63.27	2.17	2.17	61.44	61.66
Mean Current (A)	37.60	37.69	4	4	24.07	24.14
Mean Absolute Battery Power (kW)	133.95	136.92	54.48	54.48	103.53	101.15
Mean Fuel Cell Net Power (kW)	21.83	21.94	0.08	0.08	13.61	13.70

From the obtained results, Hilly terrain drive cycle is the most demanding cycle (with 38.43 kWh of trip energy), followed by the silent watch profile (with 29.51 kWh of trip energy) and then

the highway driving (with 16.44 kWh of trip energy). With the current fuel cell and battery sizing, the highway driving is barely using the fuel cell, showing that commercial vehicles are less load demanding than military vehicles. The ECMS performs close to the DP (the results have barely any difference). The reason behind this similarity in performance is explained in [66]. Due to our problem formulation being convex in fuel cell hydrogen consumption and concave with state of charge time derivative, the ECMS will perform similarly to DP independently of battery size as long as the equivalence factor chosen matched the final SOC from the DP results.

4.5 Battery Sizing Analysis Results with NMC

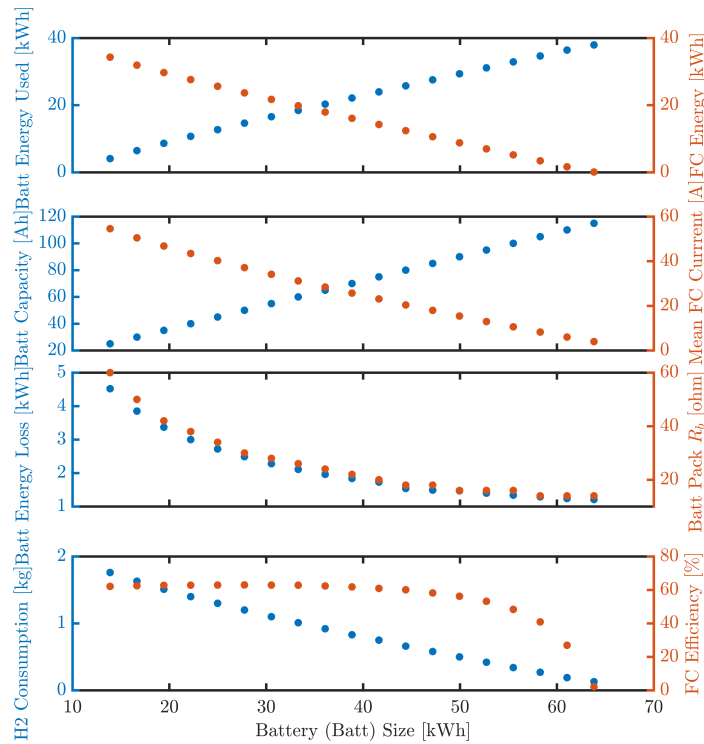


Figure 4.8: Battery size comparison for Hilly terrain drive cycle.

Since the battery size is influenced by the driving cycle [155], for the battery sizing analysis, the most demanding drive cycle should be chosen (worst case scenario). Hilly terrain drive cycle seems to require the most energy (Trip Energy is 38.43 kWh compared to 29.51 kWh from Silent watch profile and 16.44 kWh from Highway driving) and most power (RMS=158 kW compared to the Silent watch profile of RMS=135 kW). The Silent watch profile in the ETC gun portion has a peak power of around 500 kW compared to the Hilly terrain drive cycle that only has 230 kW of

peak power. Still, Hilly terrain cycle maintains the 230 kW for longer periods compared to Silent watch profile. Therefore, Hilly terrain drive cycle is chosen for the battery sizing analysis.

DP will be used to obtain the optimum power split given the various battery sizes (as shown by Table 4.7) investigated in this study. For a fair comparison all battery sizes considered will operate within a depleting mode of 85-24% SOC. The battery size is investigated based on changing the parallel connection (n_p) while maintaining the same series connection (n_s) that maintains the stack voltage. A constant internal resistance (R_b) of 2 ohm is used for this comparison to represent the NMC chemistry. The value of 2 ohms is obtained from approximating the internal resistance of the NMC shown in Fig. 4.4.

The results from the battery sizing are shown in Fig. 4.8 and a pattern is observed when the battery energy in the pack is reduced. When the battery energy in the pack is reduced, the battery capacity of the pack is also decreasing while the battery losses increase. The pattern makes sense since the number of battery cells in parallel in a module (n_p) is being reduced (evidenced by Eq. (4.15) and Eq. (4.31)). Therefore, as the n_p decreases, the fuel cell energy usage and hydrogen consumption will increase. However, the fuel cell efficiency is the best for a battery size of 28 KWh. The decrease in fuel cell efficiency for bigger or smaller batteries is due to the compressor taking more power from the fuel cell. To determine what will be the most appropriate battery size for the medium size military vehicle a comparison between the weight ($M_{T,v}$,kg), volume (V_T ,L), and total cost of the vehicle (C_T ,\\$) is performed. The weight of the vehicle (kg) is calculated by the following equation:

$$M_{T,v} = m_v + n_s n_p m_b + n_{st} m_{fc} + \frac{n_{st}}{2} m_{comp} + n_{HT} m_{HT} \quad (4.32)$$

where $m_{comp} = 9.1$ kg is the compressor weight [1], $n_{HT} = 3$ is the number of hydrogen tanks, and $m_{HT} = 97$ kg is the weight of a hydrogen tank [62]. Each tank can provide around 5 kg of hydrogen. The Hilly terrain drive cycle consumes around 2 kg for 40 miles. Therefore, the number of hydrogen tanks (n_{HT}) will be equal to 3 to be sufficient for 300 miles operation of the medium size vehicle. The total cost of the vehicle (C_T ,\\$) is given as [19],[101]:

$$C_T = CC + OC \quad (4.33)$$

where CC is the capital cost:

$$CC = C_B E_B + C_{fc} P_{net} + C_{HT} S E_{H2} n_{HT} M_{HT} \quad (4.34)$$

where $C_B = 169$ (\$/kWh) is the cost of an NMC battery pack [104], $C_{fc} = 46$ (\$/kW(net)) is the fuel cell system cost (including fuel cell and BOP) [60], and $P_{net} = 120$ kW(net) is the net power

of the fuel cell system (fuel cell and BOP). The tank cost is $C_{HT} = 10.80$ (\$/kWh), $SE_{H_2} = 33.3$ kWh/kg is the specific energy of hydrogen, and $M_{HT} = 5$ kg is the usable hydrogen tank capacity [62]. The battery energy for each battery pack size is given in Table 4.7, and calculated as:

$$E_B = n_s n_p Q_{cell} V_{ave} \quad (4.35)$$

where $Q_{cell} = 5$ Ah is the capacity of one NMC cell and $V_{ave} = 3.7$ V is the average voltage.

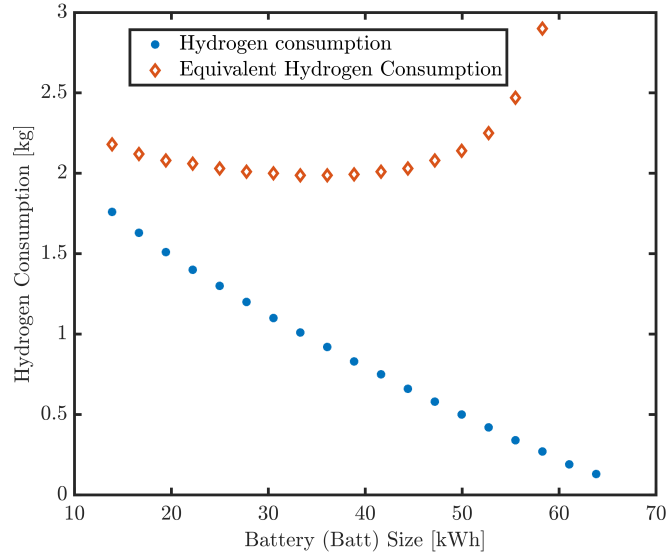


Figure 4.9: Hydrogen consumption comparison for Hilly terrain drive cycle.

The operating cost (OC) is:

$$OC = C_F \times \frac{HC_e}{D_m} \times D \quad (4.36)$$

where $C_F = 10$ \$/kg is the fuel price, $D_m = 40$ are the total miles traveled by the medium size vehicle operating Hilly terrain drive cycle for 1 hour, $D = 100,000$ is the total mileage over the ownership of the vehicle, and HC_e is the equivalent hydrogen consumption (kg) for Hilly terrain drive cycle operating for 1 hour given as:

$$HC_e = \frac{\text{Battery energy}}{Q_{lhv}} \frac{100}{\text{Stack net efficiency}} + \int \dot{m}_f \quad (4.37)$$

and shown in Fig. 4.9. The equivalent hydrogen consumption takes into account the energy used from the battery and converts it to hydrogen and adds it to the actual hydrogen consumption of the

fuel cell. The volume (L) [19] is given as:

$$V_T = \frac{E_B}{ED_{BC}} + n_{st}Vol_{fc} + n_{HT}V_{HT} \quad (4.38)$$

where $ED_{BC} = 0.274$ kWh/L is the energy density of the battery pack [104], $Vol_{fc} = 52$ L is the

Table 4.7: Battery Size Comparison for Hilly terrain drive cycle with NMC

Battery Energy (kWh)	n_p	η_{fc} (%)	$M_{T,v}$ (kg)	V_T (L)	CC (\$)	OC (\$)	C_T (\$)
13.88	5	62.10	12,321	1,116	13,260	54,500	67,760
16.65	6	62.49	12,362	1,126	13,728	53,000	66,728
19.43	7	62.75	12,402	1,136	14,198	52,000	66,198
22.2	8	62.82	12,443	1,146	14,666	51,500	66,166
24.98	9	62.90	12,483	1,156	15,136	50,750	65,886
27.75	10	62.98	12,524	1,166	15,604	50,250	65,854
30.53	11	62.88	12,564	1,176	16,074	50,000	66,074
33.3	12	62.81	12,605	1,187	16,542	49,688	66,230
36.08	13	62.37	12,645	1,197	17,012	49,693	66,705
38.85	14	61.79	12,686	1,207	17,480	49,833	67,313
41.63	15	60.90	12,726	1,217	17,950	50,250	68,200
44.4	16	60.08	12,767	1,227	18,418	50,750	69,168
47.18	17	58.18	12,807	1,237	18,888	52,000	70,888
49.95	18	56.21	12,848	1,247	19,356	53,500	72,856
52.73	19	53.21	12,888	1,257	19,826	56,250	76,076
55.5	20	48.36	12,929	1,268	20,294	61,750	82,044

volume of the fuel cell stack [4], and $V_{HT} = 147$ L is the volume of one hydrogen tank [62]. From the results in Table 4.7, the sensitivity of the weight to the battery size is almost insignificant ($\sim 5\%$) while the volume and the total cost is more sensitive ($\sim 14\text{-}21\%$). It makes sense that the battery size is not sensitive to the total weight of the vehicle. The medium size vehicle weights 11,100 kg. Therefore, the battery pack will not add significant weight to the overall vehicle. For smaller vehicles (around 1600 kg), the battery pack will have more influence on the weight of the vehicle. Due to the behavior shown in Fig. 4.9, the lowest total cost battery size is the 28 kWh with a total cost \$65,854. Future work will include fuel cell sizing in addition to battery size.

4.6 Battery Sizing Comparison between NMC and LFP

In this section, the chosen battery size 28 KWh ($n_s = 150$ and $n_p = 10$) results are compared with the results obtained by using an internal resistance (R_b) of 1 ohms with the LFP chemistry. The approximation for the resistance is obtained from [37]. DP is used for the comparison of both

chemistries at the chosen battery size with the final SOC around 24%. The results from the battery sizing comparison for LFP ($R_b = 1$ ohm) and NMC ($R_b = 2$ ohm) are shown in Table 4.8 for a power cell (capacity of both cell chemistries is 5 Ah). Since the capacity for both cells are the same, the $n_p = 10$ is equal for both. Due to the LFP having a lower voltage range compared to NMC (3.6-2 volts compared to 4.1-3 from NMC) the $n_s = 176$ was chosen assuming an average voltage of 3.15 volts.

Table 4.8: Battery Size Comparison for Hilly terrain drive cycle

Parameters	NMC 27.75 KWh $n_s = 150$ $R_p = 30$ ohm	LFP 27.75 KWh $n_s = 176$ ohm $R_p = 18$ ohm
Trip Energy (kWh)	38.30	38.26
Battery Capacity for pack (Ah)	50	50
Battery Energy (kWh)	14.64	16.31
Battery Energy Loss (kWh)	2.49	1.39
Fuel Cell Energy (kWh)	23.66	21.95
Battery to Trip Energy ratio	0.38	0.43
Hydrogen Consumption (kg)	1.20	1.11
Stack Net Efficiency (%)	62.98	62.98
Mean Current (A)	37.12	34.45

As for the comparison between LFP and NMC for all the chosen battery sizes, it is observed that NMC has approximately twice the battery loss than LFP, which is due to the fact that the internal resistance of NMC is twice larger than that of LFP (2 ohm compared to 1 ohm from LFP). Because of the higher internal resistance, the battery usage will be limited compared to LFP, as shown by the battery energy, and battery to trip energy ratio. Therefore, the fuel cell is used more for NMC than LFP, as shown by the fuel cell energy, current, and hydrogen consumption for all battery sizes confirming that LFP is better for the fuel cell vehicle than NMC.

4.7 Conclusion

In this chapter we investigated and developed a medium-size military vehicle's power split based on two approaches including dynamic programming (DP) and equivalent consumption minimization strategy (ECMS). A liquid cooling strategy capable of regulating a fixed 65°C condition with low parasitic losses is assumed for all the strategies. The Hilly terrain drive cycle is chosen to represent the vehicle's behavior in a military mission, and highway driving cycle to describe commercial vehicles' behavior. The third cycle (silent watch profile) is chosen where an ETC gun fires while

a portion represents silent mobility representing a more realistic mission environment. From the obtained results, the fuel cell is barely used over the highway driving cycle (only 0.08 kW of mean fuel cell net power and 54.48 kW of mean absolute battery power), showing that commercial vehicles are less demanding than military vehicles.

For the Hilly terrain drive cycle, Highway cycle, and the Silent watch profile, ECMS performance is relatively close to DP by choosing a value of an equivalence factor that matches the final SOC from DP. The similarity in performance is due to our problem formulation being convex in fuel cell hydrogen consumption and concave with the state of charge time derivative. Independent of battery size, ECMS will always perform similarly to DP if the equivalence factor chosen matches the final SOC obtained from DP. For the ECMS, an estimate of the SOC trajectory using the obtained results can be used with the work in [24] and be validated for real-time implementation.

For the battery sizing, the results demonstrate that sizing is vital for maximizing fuel cell efficiency. It shows that in terms of fuel cell efficiency, there is an optimal battery size. For this study, the optimal battery size seems to be 28 KWh since it is the cheapest and operates at the highest fuel cell system efficiency.

As for the battery chemistry, LFP seems to be preferable to NMC since LFP has lower battery losses and uses less the fuel cell than NMC. In [20], it is suggested that the temperature should be taken into account when evaluating the specific energy and power of different battery chemistries for military vehicles. Future work should include the thermal analysis of the battery in the modeling for the battery sizing analysis between NMC and LFP for the medium size military vehicle. The nonlinear LFP open-circuit voltage should also be considered to obtain a more realistic comparison.

CHAPTER 5

Co-optimization of Speed Trajectory and Power Management for a Fuel-cell/Battery Electric Vehicle

5.1 Introduction

With the advent of connected and autonomous vehicles, optimal energy management has become an important part of vehicle control strategies. Control strategies for Autonomous Vehicles (AV) can directly manipulate the speed of the vehicle to minimize energy consumption by utilizing information from vehicle-to-vehicle, and vehicle-to-infrastructure communication about future road conditions. The so-called *eco-driving* problems of determining the speed trajectory that minimizes a vehicle's energy consumption for various powertrain architectures such as conventional vehicles and electrified vehicles have been extensively explored in the literature.

On the other hand, vehicle hybridization introduces new challenges to the energy management problem. The increase in the number of state and control variables with hybridization can contribute to improved fuel efficiency, but it increases the complexity of the optimal control problems, e.g., battery state-of-charge (SOC) and power-split ratio among two (or more) energy sources. Therefore, the approaches or algorithms studied for vehicles with a single energy source (e.g., a conventional vehicle with an internal combustion engine or a battery-powered electric vehicle) may not lead to the global solution for eco-driving of hybridized vehicles and hence much effort has been spent to address the co-optimization problem for hybrid electric vehicles. Typically, these problems have been solved in two ways, either with sequential optimization that minimizes the energy demand at the wheel, or with co-optimization that takes into account the energy generation within the propulsion systems.

A bi-level optimization or a sequential optimization has been applied based on the idea of decoupling the optimization of the speed profile (first level) and the power management (second level) to reduce computation cost in terms of time and memory usage. In the first level, the speed profile is optimized by minimizing (1) the energy consumption by a single power source such as the engine and the motor [111, 105, 123, 85, 124], or (2) the deviation of acceleration [25]. In the

second level, minimum energy consumption is achieved by (1) optimal gear shifting, (2) optimal power-split between the engine and the motor, or (3) both gear-shifting and power-split depending on vehicle architecture. For example, in [25], the authors presented the potential for fuel efficiency improvement by the sequential smoothing of a velocity profile given traffic constraints and the optimization of its charge depletion strategy in a plug-in hybrid electric vehicle application.

Approaches to co-optimization have also been discussed in several papers. In [52], a co-optimization was carried out by allowing for small deviations in velocity and controlling the power split for a hybrid electric vehicle. This work was further improved in [53], where first the long-horizon SOC trajectory was optimized and then within a short horizon, the co-optimization was implemented. The authors in [95, 96, 97] developed algorithms that combine Dynamic Programming with the Energy Management System design for a hybrid electric vehicle to calculate eco-driving cycles. Notably, the performance of co-optimization was presented in comparison with sequential optimization approaches for a parallel hybrid electric vehicle in [85] where four methods were used to solve the optimal control problem and compared in terms of fuel consumption saving, state trajectories, computation time and memory to find the trade off between optimality and complexity. From the four methods, the two step sequential optimization of the control variables achieves near optimal fuel savings while maintaining a reasonable computation time. The performance of co-optimization was also presented in comparison with sequential optimization approaches for a series hybrid electric vehicle in [23]. The co-optimization consisted on finding the optimal speed profile and the power split simultaneously, which performed better in terms of fuel economy compared to the sequential optimization approach.

Here we study electric vehicles with a hybrid energy storage system consisting of a hydrogen fuel-cell and a battery. Fuel-cell hybrid energy storage systems in applications to ground vehicles have been intensively studied in literature for their potential to improve energy efficiency and emissions [73, 157]. In [73] a multi-input multi-output controller was developed that minimizes the primary energy consumption and startup time while balancing energy generation among a fuel cell, thermoelectric device, and battery. In [157] a finite state machine strategy was proposed for energy management for a hybrid vehicle that consisted of fuel cell/battery/supercapacitor system. Energy management techniques for fuel-cell hybrid electric vehicles and trams have also been investigated and are well discussed in [140] and [115], respectively. There are additional benefits for military applications because of their potential for increased mobility, ability to export electrical power, silent watch, and low-temperature operation (i.e., no heat signature or noise). Especially, the Proton Exchange Membrane Fuel Cell has high efficiency (around 50% of peak efficiency) and low operating temperature (around 70°C).

In this chapter, the problem formulation for co-optimization and sequential optimization of a speed profile and power management for a fuel-cell/battery powered electric vehicle is dis-

cussed. Section 5.2 details models to capture the longitudinal dynamics and powertrain behavior of a fuel-cell/battery powered electric vehicle. Section 5.3 addresses the problem formulation for co-optimization of a speed profile and power management and its PMP analysis. Approaches to co-optimization and sequential optimization are discussed as well. Then, the performance of the two approaches in terms of energy consumption and driving time is investigated through a case study in Section 5.4. Finally, conclusions are presented in Section 5.5.

5.2 Vehicle and Powertrain Model

The vehicle of interest in this study is a lightweight military ground robot electrically hybridized by a battery pack and a fuel cell. This hybridized architecture allows it to smooth out transient loads and to provide auxiliary power during startup and shutdown of the fuel cells. Especially, Proton Exchange Membrane Fuel Cells are of great interest to the army because of their advantages such as silent mobility and low heat signature ($\approx 70^\circ\text{C}$). The topology of the fuel-cell/battery powertrain considered in this study is illustrated in Fig. 5.1. The fuel-cell is coupled to the battery by a DC/DC converter that regulates the power flow from the fuel-cell to account for the change in cell terminal voltage. The main focus of this work is on optimization of vehicle speed and power management. In general, a DC/DC converter has its maximum efficiency around 95% and has a similar shape to the efficiency curve of the Proton Exchange Membrane Fuel-cell system which typically has poor efficiency at low power, reaches a peak between 20 and 50% of the rated power, and then tapers off slightly at high power levels. Therefore, detailed models for power electronics and efficiency are not considered, that is, power losses by the DC/DC converter are not included in this study.

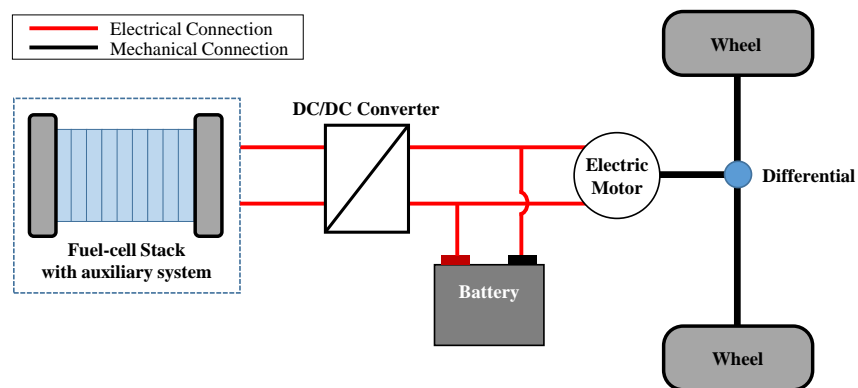


Figure 5.1: A simple schematic of a fuel-cell/battery powered electric vehicle.

5.2.1 Point-mass Longitudinal Dynamics

The longitudinal dynamics of the vehicle to determine propulsion and braking power are described by:

$$\dot{s} = v, \quad (5.1)$$

$$M\dot{v} = f_m + f_b - f_r, \quad (5.2)$$

where M is the vehicle mass, s and v denote the distance and velocity of the vehicle, f_m is the mechanical force provided by the electric motor, f_b is the force by the friction brake. The resistive force f_r is computed based on the grade θ and velocity of a vehicle as given by,

$$f_r = A + Bv + Cv^2 + Mg \sin \theta, \quad (5.3)$$

where coefficients A , B , and C are used to determine resistance forces by rolling and aerodynamic drag, and the grade angle θ is a function of distance, i.e. $\theta = \theta(s)$.

5.2.2 Lumped Efficiency Parameters for Fuel Cell System

In this study, a liquid-cooled Proton Exchange Membrane Fuel-cell system is considered based on the model of a 15 kW Hydrogenics HD15 stack. To include a parasitic load for cooling and air supply, a static power consumption is considered, and hence the fuel-cell system is modeled with a simple static function of the fuel cell system efficiency, η_{fc} ; hence, the hydrogen fuel power P_{fc}^{in} can be expressed as follows:

$$P_{fc}^{in} = \frac{P_{fc}^{out}}{\eta_{fc}}, \quad (5.4)$$

where P_{fc}^{out} is the fuel-cell net power. In general, the fuel cell system efficiency η_{fc} is influenced by the operating temperature of the fuel-cell system. Since the fuel cell generates a significant amount of heat, auxiliary power is required for regulating temperature. In this study, it is assumed that the temperature of the fuel-cell system is perfectly regulated at 60°C such that the maximum efficiency can be achieved for various power levels. A more detailed description of the fuel-cell model is provided in section 2.2.1 and 2.3. Under this assumption, η_{fc} can be expressed in terms of fuel cell's net system power (P_{fc}^{out}):

$$\eta_{fc} = \phi(P_{fc}^{out}). \quad (5.5)$$

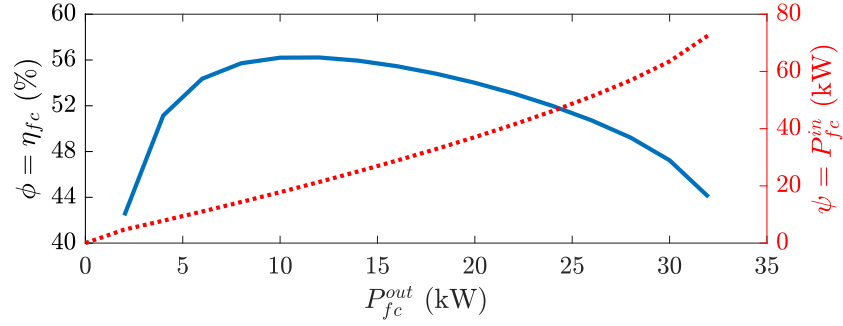


Figure 5.2: The static efficiency of the fuel-cell system. The power for the blower and cooling system load to regulate the temperature of the fuel-cell is included in this efficiency.

From equations (5.4) and (5.5), the hydrogen fuel power is given by:

$$P_{fc}^{in} = \psi(P_{fc}^{out}), \quad (5.6)$$

where $\psi(P_{fc}^{out}) = P_{fc}^{out} / \phi(P_{fc}^{out})$ which is shown in Fig. 5.2. Here two stacks are required to achieve the power requirement of the vehicle.

5.2.3 Battery Model

When it comes to power management, the battery output power P_b is generally used as an input to the battery system and hence the following equation is used to convert the battery power output to the corresponding current:

$$I_b = \frac{V_{oc} - \sqrt{V_{oc}^2 - 4R_b P_b}}{2R_b}. \quad (5.7)$$

In this chapter we used the same NMC battery model as Chapter 4.2.

5.2.4 Motor Model

The electrical power for propulsion and regenerative braking by the motor P_m^{elec} is determined from the mechanical power and the efficiency of the motor, P_m^{mech} and η_m , respectively. The electrical power P_m^{elec} should be provided by the fuel cell and the battery and hence the following equation is obtained:

$$P_m^{elec} = \frac{f_m^{prop} v}{\eta_{m,1}} + f_m^{reg} v \eta_{m,2} = P_b + P_{fc}^{out} \eta_{DC} \quad (5.8)$$

where f_m^{prop} and f_m^{reg} represent the positive force for propulsion and the negative force for regeneration by the motor, respectively; η_{DC} denotes the efficiency of the DC/DC converter; and $\eta_{m,1}$ and $\eta_{m,2}$ denote motoring and generating efficiency of the motor, respectively. Note that the main focus of this work is on optimization of vehicle speed and power management and hence is concerned on power flows among powertrain components, i.e., the fuel-cell, the battery, and the motor; therefore, detailed models for power electronics are not considered, that is, power losses by the DC/DC converter are not included in this study and hence $\eta_{\text{DC}} = 1$ is assumed.

5.3 Optimal Control Problem Formulation

In this section, two approaches to optimization of the speed profile and power management for the all-electric vehicle considered in this study are presented: co-optimization and sequential optimization.

For simplicity, the assumptions in [10] are adopted in this study: (1) the efficiency of the motor is invariant, that is, the motoring and generating efficiency of the motor is fixed; (2) the vehicle moves forward only; and (3) road grade and velocity limit are distance-dependent and known. In general, the efficiency of an electric motor is nonlinear [26]. However, the efficiency is relatively constant above certain force or torque levels covering the nominal operating range, and hence the assumption of invariant efficiency is considered reasonable.

5.3.1 System Dynamics

For PMP analysis, the battery dynamics are simplified via linearization as given by:

$$\begin{aligned} \dot{\text{SOC}} &\approx \left. \frac{-V_{\text{oc}} + \sqrt{V_{\text{oc}}^2 - 4P_b^0 R_b}}{2Q_b R_b} \right|_{P_b^0=0} \\ &\quad + \left. \frac{1}{2Q_b R_b} \frac{-4R_b P_b}{2\sqrt{V_{\text{oc}}^2 - 4P_b^0 R_b}} \right|_{P_b^0=0} \\ &= -\frac{1}{Q_b V_{\text{oc}}} P_b. \end{aligned} \tag{5.9}$$

It should be noted that similar approaches to approximating the battery SOC dynamics can be found in the literature [45, 17].

Finally, from Eqs. (5.1), (5.2), (5.8), and (5.9), the following system dynamics can be obtained:

$$\dot{x}_1 = x_2, \quad (5.10)$$

$$\dot{x}_2 = u_1 + u_2 + u_3 - \kappa(x_1, x_2), \quad (5.11)$$

$$\dot{x}_3 = \sigma(x_2, u_1, u_2, u_4), \quad (5.12)$$

where

$$x = [x_1, x_2, x_3]' = [s, v, \text{SOC}]',$$

$$u = [u_1, u_2, u_3, u_4]' = \left[\frac{f_m^{\text{prop}}}{M}, \frac{f_m^{\text{reg}}}{M}, \frac{f_b}{M}, P_{\text{fc}}^{\text{out}} \right]',$$

and

$$\kappa = \frac{f_r(x_1, x_2)}{M},$$

$$\sigma = - \frac{1}{Q_b V_{\text{oc}}(x_3)} \left(\frac{M x_2 u_1}{\eta_{m,1}} + M x_2 u_2 \eta_{m,2} - u_4 \right).$$

The control inputs are bounded by their limits such that $u_1 \in [0, u_1^{\text{max}}]$, $u_2 \in [u_2^{\text{min}}, 0]$, $u_3 \in [u_3^{\text{min}}, 0]$, and $u_4 \in [0, u_4^{\text{max}}]$. It is noted that the power losses by the DC/DC converter are not considered and hence $\eta_{\text{DC}} = 1$ is assumed. When $\eta_{\text{DC}} \neq 1$, $u_4 = P_{\text{fc}}^{\text{out}} \cdot \eta_{\text{DC}}$ needs to be used instead.

The use of four control inputs is deliberate for Pontryagin's Minimum Principle analysis, which will be discussed in the following section, similar to the approach in [10]. Initial and final conditions of the states are:

$$\begin{aligned} x_1(0) &= 0, & x_2(0) &= v_0, & x_3(0) &= \text{SOC}_0, \\ x_1(t_f) &= s_f, & x_2(t_f) &= v_f, & x_3(t_f) &= \text{SOC}_f, \end{aligned} \quad (5.13)$$

where t_f and s_f are operational time and distance traveled, and these are bounded, meaning that the vehicle stops at time t_f after traveling a given distance, s_f .

5.3.2 Simplification of Control Modes

In this subsection, the co-optimization problem to minimize hydrogen fuel consumption is presented and analyzed to determine a small subset of control actions via Pontryagin's Minimum Principle (PMP) analysis. In the authors' previous work [10], a finite number of operational modes were analytically found for minimum electrical energy consumption. Since this study considers

additional state and control variables, the battery SOC and power split ratio, respectively, a similar analysis has been conducted so that the results can be used to effectively implement Dynamic Programming to mitigate the computational burden due to *the curse of dimensionality*.

The primary goal of the optimization is to determine a speed profile and a power split trajectory that minimize the total energy consumption over a given route. Thus, the cost function to be minimized is the total hydrogen fuel energy, defined by:

$$\mathcal{J} = \int_0^{t_f} P_{fc}^{\text{in}} (P_{fc}^{\text{out}}) dt = \psi(u_4) dt \quad (5.14)$$

Since the given optimal control problem suffers from the curse of dimensionality when it is solved by Dynamic Programming, simplified control actions are much preferred. To that end, Pontryagin's Minimum Principle is considered, similarly to the approach in [10]: the solution to the optimal control problem leads to the minimization of the Hamiltonian comprised of the cost function subject to constraints via the system dynamics.

The Hamiltonian is defined as:

$$\begin{aligned} \mathcal{H} = & \psi(u_4) + p_1 x_2 + p_2 (u_1 + u_2 + u_3 - \kappa(x_1, x_2)) \\ & - \frac{M p_3}{Q_b V_{oc}(x_3)} \left(\frac{x_2 u_1}{\eta_{m,1}} + x_2 u_2 \eta_{m,2} - \frac{u_4}{M} \right) \end{aligned} \quad (5.15)$$

where the first term corresponds to the cost function in (5.14) and the other terms are related to the system dynamics described by (5.10)–(5.12) associated with the adjoint variables p_1 , p_2 , and p_3 . The dynamics of the adjoint variables are given by:

$$\dot{p}_1 = - \frac{\partial \mathcal{H}}{\partial x_1} = p_2 \kappa_{x_1}, \quad (5.16)$$

$$\dot{p}_2 = - \frac{\partial \mathcal{H}}{\partial x_2} = -p_1 + p_2 \kappa_{x_2} + \tilde{p}_3 \left(\frac{u_1}{\eta_{m,1}} + u_2 \eta_{m,2} \right), \quad (5.17)$$

$$\dot{p}_3 = - \frac{\partial \mathcal{H}}{\partial x_3} = \left(\frac{x_2 u_1}{\eta_{m,1}} + x_2 u_2 \eta_{m,2} - \frac{u_4}{M} \right) \tilde{p}_{3x_3}, \quad (5.18)$$

where

$$\tilde{p}_3 = \frac{M p_3}{Q_b V_{oc}(x_3)},$$

and $(\cdot)_* = \frac{\partial(\cdot)}{\partial *}$.

The Hamiltonian function is further simplified by factoring out the control input u in order to

determine optimal control inputs. Then equation (5.15) becomes:

$$\begin{aligned} \mathcal{H} = & \left(p_2 - \frac{\tilde{p}_3 x_2}{\eta_{m,1}} \right) u_1 + (p_2 - \tilde{p}_3 x_2 \eta_{m,2}) u_2 + p_2 u_3 \\ & + \psi(u_4) + \frac{\tilde{p}_3 u_4}{M} + p_1 x_2 - p_2 \kappa(x_1, x_2). \end{aligned} \quad (5.19)$$

As can be seen from Eq. (5.19), the control inputs u_1 , u_2 , and u_3 appear as linear, meaning that, based on the values of the switching functions $p_2 - \frac{\tilde{p}_3 x_2}{\eta_{m,1}}$, $p_2 - \tilde{p}_3 x_2 \eta_{m,2}$, and p_2 , the control inputs u_1 , u_2 , and u_3 to minimize \mathcal{H} can be found. On the other hand, the control input u_4 is given by:

$$u_4 = \begin{cases} 0, & \text{if } u^* \leq 0 \\ u^*, & \text{if } 0 < u^* < u_4^{\max} \\ u_4^{\max}, & \text{o.w.} \end{cases}$$

where u_4^* is determined from the stationary condition $\frac{\partial \mathcal{H}}{\partial u_4} = 0$.

Since each switching function for u_1 , u_2 , and u_3 has three options, of being greater than, less than, or equal to 0, 27 different modes are possible. However, not all of the modes are feasible due to the assumptions considered for the problem. For instance, the conditions $p_2 - \frac{\tilde{p}_3 x_2}{\eta_{m,1}} > 0$, $p_2 - \tilde{p}_3 x_2 \eta_{m,2} = 0$, and $p_2 \geq 0$ cannot occur at the same time. From the first two conditions, $\tilde{p}_3 x_2 \eta_{m,2} > \frac{\tilde{p}_3 x_2}{\eta_{m,1}}$; because of the fact that efficiency of the motor is positive and less than 1 (i.e., $0 < \eta_m < 1$) and the assumption that the electric vehicle moves forward only (i.e., $x_2 > 0$), \tilde{p}_3 has to be negative, and p_2 has to be negative. Similarly, the conditions $p_2 - \frac{\tilde{p}_3 x_2}{\eta_{m,1}} < 0$, $p_2 - \tilde{p}_3 x_2 \eta_{m,2} > 0$, and $p_2 \leq 0$ cannot occur simultaneously. It is also obvious that the motor cannot provide both propulsion and regeneration forces simultaneously, which allows for ruling out the conditions $p_2 - \frac{\tilde{p}_3 x_2}{\eta_{m,1}} < 0$ and $p_2 - \tilde{p}_3 x_2 \eta_{m,2} > 0$. Moreover, the conditions $p_2 - \frac{\tilde{p}_3 x_2}{\eta_{m,1}} < 0$ and $p_2 > 0$ can be eliminated as both propulsion force and friction braking force are used, which should be avoided to minimize the energy consumption.

The following six cases are feasible in vehicle operation:

$$p_2 - \frac{\tilde{p}_3 x_2}{\eta_{m,1}} < 0, p_2 - \tilde{p}_3 x_2 \eta_{m,2} < 0, p_2 < 0 \quad (5.20a)$$

$$p_2 - \frac{\tilde{p}_3 x_2}{\eta_{m,1}} > 0, p_2 - \tilde{p}_3 x_2 \eta_{m,2} < 0, p_2 < 0 \quad (5.20b)$$

$$p_2 - \frac{\tilde{p}_3 x_2}{\eta_{m,1}} > 0, p_2 - \tilde{p}_3 x_2 \eta_{m,2} > 0, p_2 < 0 \quad (5.20c)$$

$$p_2 - \frac{\tilde{p}_3 x_2}{\eta_{m,1}} > 0, p_2 - \tilde{p}_3 x_2 \eta_{m,2} > 0, p_2 > 0 \quad (5.20d)$$

$$p_2 - \frac{\tilde{p}_3 x_2}{\eta_{m,1}} = 0, p_2 - \tilde{p}_3 x_2 \eta_{m,2} < 0, p_2 < 0 \quad (5.20e)$$

$$p_2 - \frac{\tilde{p}_3 x_2}{\eta_{m,1}} > 0, p_2 - \tilde{p}_3 x_2 \eta_{m,2} = 0, p_2 < 0 \quad (5.20f)$$

The optimal control inputs u_1 , u_2 , and u_3 for the first four cases can be easily determined to minimize the Hamiltonian, resulting in *full propulsion*, *coasting*, *full regenerative braking*, and *full braking*, respectively. On the other hand, for the last two cases, u_1 and u_2 are undefined because the optimal control actions cannot be determined uniquely; in this case, Kelley's condition [65] can be used to determine the optimal control inputs: for a single control problem, the control u for a singular-arc can be found by differentiating $\chi = \frac{\partial \mathcal{H}}{\partial u}$ with respect to time t until the control input u appears explicitly, and then Kelley's condition must be satisfied. That is:

$$\begin{aligned} \frac{d^i \chi}{dt^i} &= 0, \quad i = 0, 1, \dots, 2l - 1, \\ \frac{d^{2l} \chi}{dt^{2l}} &= h_1(x, p) + h_2(x, p)u, \\ (-1)^{l+1} \frac{d}{du} \left(\frac{d^{2l} \chi}{dt^{2l}} \right) &\leq 0 \end{aligned} \quad (5.21)$$

where l is an integer variable.

In case (5.20e), u_1 is undefined. Consider $\chi_1 = p_2 - \frac{\tilde{p}_3 x_2}{\eta_{m,1}} = 0$. Then, its first and second time derivatives are expressed as follows:

$$\begin{aligned} \dot{\chi}_1 &= -p_1 + p_2 \kappa_{x_2} + \frac{\tilde{p}_3 \kappa}{\eta_{m,1}} = 0, \\ \ddot{\chi}_1 &= p_2 \left(\frac{2\kappa_{x_2}}{x_2} + \kappa_{x_2 x_2} \right) (u_1 - \kappa) + p_2 \kappa_{x_1 x_2} x_2 = 0. \end{aligned}$$

From Eq. (5.3), it can be found that the resistance force f_r is the sum of two terms, and each term is described by one state only, leading to $\kappa_{x_1 x_2} = 0$; moreover, the resistance force is a monotonic

Table 5.1: Possible Control Actions.

Control u	Description
$[u_1^{\max}, 0, 0] \times u_4$	Full Propulsion
$[0, 0, 0] \times u_4$	Coasting
$[0, u_2^{\min}, 0] \times u_4$	Full Regenerative Braking
$[0, u_2^{\min}, u_3^{\min}] \times u_4$	Full Braking
$[\kappa(x_1, x_2), 0, 0] \times u_4$	Cruising
$[0, \kappa(x_1, x_2), 0] \times u_4$	

function with $\kappa_{x_1}, \kappa_{x_2x_2} > 0$ and $x_2 > 0$, resulting in $\frac{2\kappa_{x_2}}{x_2} + \kappa_{x_2x_2} > 0$. Therefore, the candidate solution is obtained as

$$u_1 = \kappa(x_1, x_2), \quad (5.22)$$

and this solution satisfies the Kelley's condition:

$$(-1)^2 \frac{\partial}{\partial u_1} \frac{d^2}{dt^2} \chi_1 = p_2 \left(\frac{2\kappa_{x_2}}{x_2} + \kappa_{x_2x_2} \right) u_1 \leq 0,$$

because $\frac{2\kappa_{x_2}}{x_2} + \kappa_{x_2x_2} > 0$ and $p_2 < 0$.

Similarly, in the case (5.20f), the solution can be found to be:

$$u_2 = \kappa(x_1, x_2). \quad (5.23)$$

Clearly, both cases (5.20e) and (5.20f) describe a *cruising* operation of the vehicle, as the same amount of input is applied to the system to maintain the speed. Thus, five possible control actions are determined for u_1 , u_2 , and u_3 , and they are summarized in Table 5.1. It should be highlighted that the vehicle dynamics are controlled by the five control modes only, regardless of the fuel-cell power u_4 . This result allows a substantial decrease in computational cost in solving the co-optimization problem with Dynamic Programming. In the following subsections, Dynamic Programming formulation for co-optimization and sequential optimization is explained in detail.

5.3.3 Co-optimization

In general, the problem of optimizing a speed profile is formulated in the distance domain, since it is easy to handle road data; e.g., terrain type, grade, and speed restrictions are distance-dependent [26, 52, 53, 10]. Thus, the optimal control problem discussed in Section 5.3 can be reformulated

as follows:

$$\begin{aligned}
\min \quad & \mathcal{J}_1 = \int_0^{s_f} \frac{\psi(u_4)}{\xi_2} ds \\
\text{s.t.} \quad & \xi_1' = 1/\xi_2, \\
& \xi_2' = \frac{f_e(s, \xi_2, u_c) + f_f(u_c) - \kappa(\xi)}{M\xi_2}, \\
& \xi_3' = -\frac{V_{oc} - \sqrt{V_{oc}^2 - 4R_b(P_{\text{dmd}} - u_4)}}{2\xi_2 Q_b R_b}, \\
& \xi_1(0) = 0, \xi_1(s_f) = t_f, \\
& \xi_2(0) = v_0, \xi_2(s_f) = v_f, \\
& \xi_3(0) = \text{SOC}_0, \xi_3(s_f) = \text{SOC}_f, \\
& u_c \in \{u_{c,1}, u_{c,2}, u_{c,3}, u_{c,4}, u_{c,5}\}, \\
& u_4 \in [0, u_4^{\text{max}}],
\end{aligned} \tag{5.24}$$

where $\xi = [\xi_1, \xi_2, \xi_3]^T = [t, v, \text{SOC}]^T$; since the equations of motion are expressed in terms of s , $\xi' = \frac{d\xi}{ds}$ is used. The mode-dependent force by the motor $f_e(s, \xi_2, u_c)$ is detailed in Appendix A.1. The power demand P_{dmd} is given by:

$$P_{\text{dmd}} = \eta_m(f_e) \cdot f_e(s, \xi_2, u_c)\xi_2. \tag{5.25}$$

where

$$\eta_m(f_e) = \begin{cases} \frac{1}{\eta_{m,1}}, & f_e \geq 0, \\ \eta_{m,2}, & f_e < 0. \end{cases} \tag{5.26}$$

In order to further reduce the computational cost, the optimal control problem (5.24) is modified

such that a weighted penalty on a travel time is included as follows:

$$\begin{aligned}
\min \quad & \mathcal{J}'_1 = \int_0^{s_f} \left(\frac{\psi(u_4)}{\xi_2} + \lambda \frac{1}{\xi_2} \right) ds \\
\text{s.t.} \quad & \xi'_2 = \frac{f_e(s, \xi_2, u_c) + f_f(u_c) - \kappa(\xi)}{M\xi_2}, \\
& \xi'_3 = -\frac{V_{oc} - \sqrt{V_{oc}^2 - 4R_b(P_{\text{dmd}} - u_4)}}{2\xi_2 Q_b R_b}, \\
& \xi_2(0) = v_0, \xi_2(s_f) = v_f, \\
& \xi_3(0) = \text{SOC}_0, \xi_3(s_f) = \text{SOC}_f, \\
& u_c \in \{u_{c,1}, u_{c,2}, u_{c,3}, u_{c,4}, u_{c,5}\}, \\
& u_4 \in [0, u_4^{\max}],
\end{aligned} \tag{5.27}$$

where λ is a weighting factor to penalize a travel time. Apparently, this formulation can effectively eliminate one state variable ξ_1 from the co-optimization problem. It should be noted that a desired travel time can be achieved by adjust the weighting factor λ .

5.3.4 Sequential Optimization

Although a significant amount of reduction in computation can be achieved by using the finite operational modes of the vehicle dynamics, co-optimization is still computationally costly. Therefore, the co-optimization problem can be sequentially solved, which has been typically used in the literature [105, 123, 85, 111, 25]. In sequential optimization, an optimal speed profile is determined at the first stage, and then a power management strategy is optimized over the speed profile at the second stage. Obviously, the number of state and control variables considered at each stage is small compared to the co-optimization problem, allowing for faster computation and less memory requirement.

At stage I, the problem of optimizing a speed profile is formulated as:

$$\begin{aligned}
\min \quad & \mathcal{J}_{2,1} = \int_0^{s_f} (\eta_m(f_e) \cdot f_e(s, \xi_2, u_c)) ds \\
\text{s.t.} \quad & \xi_1' = 1/\xi_2, \\
& \xi_2' = \frac{f_e(s, \xi_2, u_c) + f_f(u_c) - \kappa(\xi)}{M\xi_2}, \\
& \xi_1(0) = 0, \xi_1(s_f) = t_f, \\
& \xi_2(0) = v_0, \xi_2(s_f) = v_f, \\
& u_c \in \{u_{c,1}, u_{c,2}, u_{c,3}, u_{c,4}, u_{c,5}\}.
\end{aligned} \tag{5.28}$$

Note that the cost function $\mathcal{J}_{2,1}$ is the total energy consumption by the motor for propulsion and regenerative braking. It is possible to further reduce the computational cost by following the approach used in (5.27), i.e., adding a penalty on a travel time and eliminating one state ξ_1 . However, for the purpose of performance comparison, travel times obtained from solutions to the optimal control problem (5.27) are used as a terminal constraint in this optimization problem.

Then, at stage II, the problem of optimal power management over the speed profile obtained from Stage I is solved with the following formulation:

$$\begin{aligned}
\min \quad & \mathcal{J}_{2,2} = \int_0^{s_f} \frac{\psi(u_4)}{\xi_2} ds \\
\text{s.t.} \quad & \xi_3' = -\frac{V_{oc} - \sqrt{V_{oc}^2 - 4R_b(P_{dmd} - u_4)}}{2\xi_2 Q_b R_b}, \\
& \xi_3(0) = \text{SOC}_0, \xi_3(s_f) = \text{SOC}_f, \\
& u_4 \in [0, u_4^{\max}]
\end{aligned} \tag{5.29}$$

where P_{dmd} is the power demand to traverse the optimized drive cycle obtained at stage I; that is, P_{dmd} is known.

In the following section, a case study to compare the performance of two optimization approaches will be presented.

5.4 Case Study - Lightweight Military Ground Robot

A light-weight military ground vehicle hybridized with a fuel cell and a battery is considered as a target vehicle. The parameters and operational constraints are summarized in Table 5.2. The drive

Table 5.2: Vehicle parameters and constraints.

Parameter	Symbol	Value	Unit
Mass	M	453.6	kg
A	A	0.17	N
B	B	0.06804	Ns/m
C	C	13.608	Ns ² /m ²
Tire radius	r	0.2794	m
Final drive ratio	i_a	7.54	-
Speed limit	v_{lim}	23	m/s
Max. Acc.	a_{max}	2	m/s ²
Min. Acc.	a_{min}	-2	m/s ²
Max. Motor Speed	$\omega_{m,max}$	6500	RPM
Max. Motor Power	$P_{m,max}$	30	kW
Motor Operation Voltage	V_m	50	V
Max. Battery Power	P_b^{max}	6	kW
Min. Battery Power	P_b^{min}	-6	kW
Number of Battery Cells in Series	N_s	14	-
Number of Battery Cells in Parallel	N_p	1	-
Max. SOC	SOC_{max}	1	-
Min. SOC	SOC_{min}	0.3	-
Max. FC Power	$P_{fc,max}^{out}$	32	kW
Min. FC Power	$P_{fc,min}^{out}$	0	kW
Number of Fuel-cell Stacks	N_{fc}	2	-
Number of Fuel-cell Cells	N_{cell}	65	-

cycles for the development of ground vehicles in the Army Ground Vehicle Programs typically focus on operating at a constant speed over varied terrain for practical reasons [132]. Thus, two different drive conditions as shown in Fig. 5.3 are studied: 1) the Convoy Cycle - long distance driving on a relatively flat road (small variation in grade), and 2) the Curchville-B Cycle - constant speed driving on a hilly road (more discernible and aggressive grade change).

5.4.1 Optimization Set-up

To solve the optimal control problems using DP, the dynamic equations with state and control variables in a time domain need to be discretized. The level of discretization affects the accuracy of a solution and the computation time: coarse discretization results in fast computation but large numerical errors. Therefore, step sizes for the discretization should be carefully chosen. The level of discretization for time, velocity, battery SOC, and distance for this study is provided in Table 5.3.

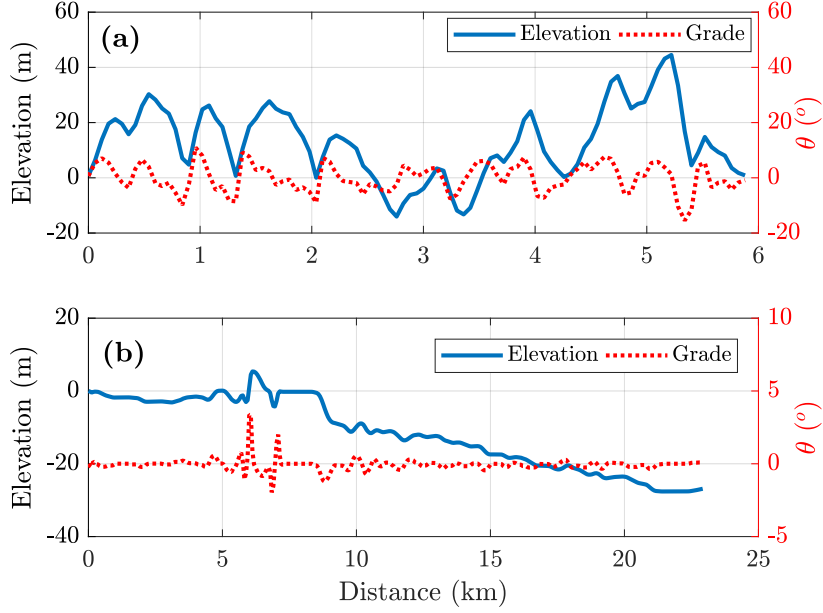


Figure 5.3: Elevation and grade of the considered driving environment. (a) Churchville-B Cycle and (b) Convoy Cycle.

Table 5.3: Discretization of optimization variables in Dynamic Programming.

State	Symbol	Value	Unit
Velocity	Δv	0.1	m/s
Time	Δt	1	s
Distance	Δs	60	m
SOC	ΔSOC	0.007	-

Since this study finds an optimal speed profile, the initial and terminal speed constraints are set to be the same as the original driving cycles as given by:

- Churchville-B Driving: $\xi_2(0) = \xi_2(s_f) = 12$,
- Convoy Driving: $\xi_2(0) = \xi_2(s_f) = 0$,

The initial and terminal constraints of the battery SOC are set as follows:

$$\text{SOC}_0 = 0.9, \text{SOC}_f \in [\text{SOC}_{\min}, \text{SOC}_{\max}].$$

Note that terminal SOC values from the co-optimization and the sequential optimization can be different, since no specific value is assigned for the terminal SOC; this will be shown in the following subsection.

A solution to the DP problem is numerically obtained by using the **dpm** function implemented in the MATLAB environment [142]. To run DP over the considered driving environment, the following hardware is used: Windows 10 with Intel[®] Core[™] i7-7700HQ CPU @ 2.80 GHz and 32.0 GB RAM.

5.4.2 Optimization Results

Table 5.4: Average computation time.

Cycle	Co-optimization	Sequential Optimization	
		<i>Speed Opt</i>	<i>Power Opt</i>
Churchville-B	5 mins 33.1 secs	4.83 secs	0.34 secs
Convoy	19 mins 49.9 secs	15.60 secs	1.18 secs

The computation time to run the co-optimization and sequential optimization are provided in Table 5.4. The co-optimization is about 64–71 times slower than the sequential optimization. It should be noted that the co-optimization is performed with limited control inputs u_c and without including time as a state variable, meaning that the original problem with discretized continuous control inputs will lead to a significant increase of the computation time.

5.4.2.1 Churchville-B Driving

Figure 5.4(a)–(d) show comparisons of energy consumption by the motor, the fuel cell, the battery, and both the fuel-cell and the battery, respectively, over the driving cycles obtained by the co-optimization and the sequential optimization for different driving times. Particularly, the numbers indicate the difference in energy consumption and the percentage reduction by co-optimization: negative values indicate that co-optimization leads to less energy consumption than sequential optimization. It can be observed from Fig. 5.4(a) that the sequential optimization leads to lower energy consumption by the motor than the co-optimization. This makes sense since the energy consumption by the motor is the cost function in the sequential optimization. On the other hand, as shown in Fig. 5.4(b), more hydrogen energy is consumed in the sequential optimization than in the co-optimization, which is not surprising because the co-optimization finds a solution that minimizes the hydrogen energy consumption. The battery energy consumption to complement the fuel cell for vehicle operation is presented in Fig. 5.4(c). Since the solutions obtained by the co-optimization prefer not using the fuel cell, a large amount of energy needs to be provided by the battery.

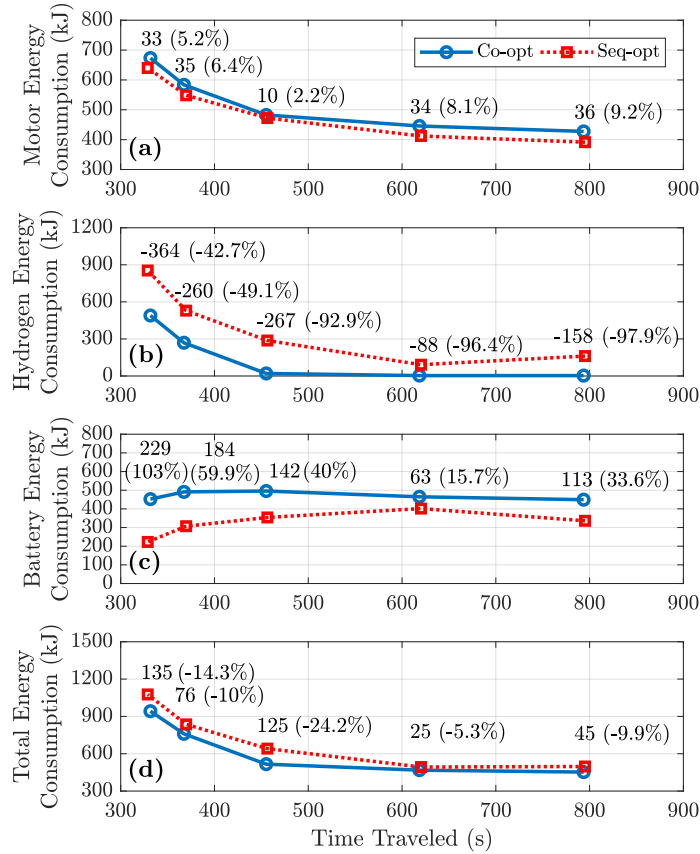


Figure 5.4: Comparison of energy consumption obtained by co-optimization and sequential optimization for various times traveled on Churchville-B road. (a) energy consumption by the motor, (b) energy consumption by the fuel cell, (c) energy consumption by the battery, and (d) the total energy consumption by the fuel cell and the battery.

The total energy consumed for each optimization approach is compared in Fig. 5.4(d). Overall, co-optimization can achieve lower total energy consumption than sequential optimization. Particularly, the total energy savings by co-optimization range from 5.3% to 24.2%, which highlights the benefit of co-optimization against sequential optimization. However, for driving cycles with a longer time traveled, the energy savings achieved by co-optimization are not as significant compared to the shorter cases.

For better understanding of the energy savings by co-optimization, the trajectories of the vehicle speed and the battery SOC are presented in Figs. 5.6(a) and (b) for the shortest cycle, and in Figs. 5.6(c) and (d) for the longest cycle, respectively. As can be seen from Fig. 5.6(a), for the shortest drive cycle, the speed profile obtained by co-optimization has less deviation than that obtained by sequential optimization. It can also be observed that the vehicle speeds selected by the two approaches are different. Particularly, the solutions by co-optimization prefer coasting dur-

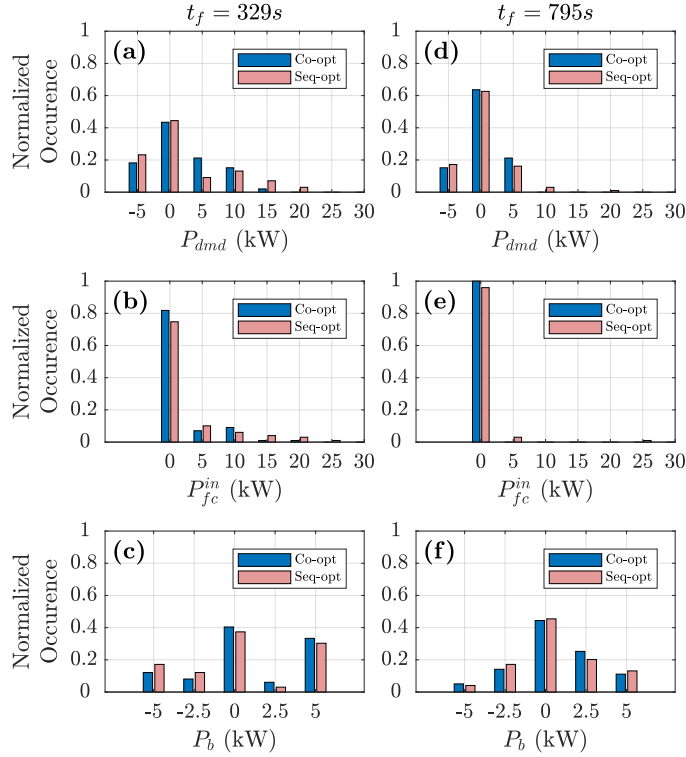


Figure 5.5: Histograms of normalized occurrence of powertrain operation obtained by co-optimization and sequential optimization on Churchville-B road for two drive cycles. (a) motor power demand, (b) fuel-cell input power, and (c) battery power with $t_f = 329s$; (d) motor power demand, (e) fuel-cell input power, and (f) battery power with $t_f = 795s$.

ing downhills, whereas those by sequential optimization prefer regenerative braking and cruising during downhills. The use of coasting is beneficial as it can minimize unnecessary energy conversion; i.e., recuperated braking energy used later for vehicle propulsion. For instance, as shown in Fig. 5.6(b), the battery SOC increases around 100 s in sequential optimization. However, no change is observed in co-optimization during the same time period. Eventually, the terminal SOC in sequential optimization becomes significantly higher than that in co-optimization. Figure 5.6(c) also shows that the deviation of vehicle speed in co-optimization is less than that in sequential optimization for the longest cycle. Since solutions by both optimization approaches prefer using cruising from 450 s until the end of the trip, the difference in terminal SOC of two solutions is less than that observed in the shortest drive cycle.

In sequential optimization, the total energy consumed by the motor is minimized and the efficiency of the powertrain system including the fuel cell and the battery is not included. Therefore, high-power operation is preferred as long as the total motor energy is minimized and the use of coasting operation can be maximized as seen from Figs. 5.5(a) and (d) at Stage I. Since the battery

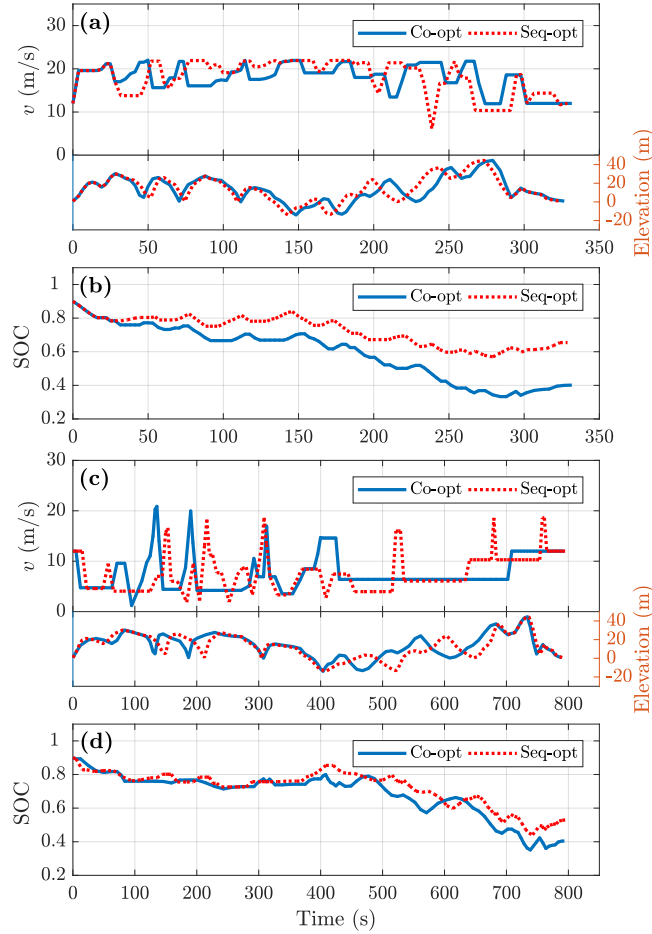


Figure 5.6: Comparison of vehicle and powertrain operation obtained by co-optimization and sequential optimization over Churchville-B road for travel times of 329 and 795 seconds. (a) vehicle speed, (b) electrical power demand by the motor, (c) power consumed by the fuel cell, (d) power provided by the battery, and (e) battery SOC.

power is insufficient to provide such high motor power, the fuel-cell needs to be used as well despite the fact that the fuel-cell system has lower efficiency than the battery, as shown in Figs. 5.5(b) and (e). The battery can be used in a wide range within its limits to minimize fuel consumption at Stage II, compared to the fuel-cell (see Figs. 5.5(c) and (f)).

On the other hand, high-power operation is not preferred in co-optimization due to low efficiency of the fuel cell as seen from Figs. 5.5(a) and (d). Therefore, the battery can be used as a primary power source and the use of the fuel-cell can consequently be reduced as shown in Figs. 5.5(b) and (d). More specifically, for the shortest cycle, the co-optimization hardly uses the fuel-cell at higher power, i.e., $P_{fc}^{in} > 10$ kW, which can be explained by the efficiency of the fuel-cell (see Fig. 5.2). Consequently, lower terminal SOC's are obtained in co-optimization than those

in sequential optimization (see Figs. 5.6(b) and (d)). It is found that the longest cycle can be driven without using the fuel-cell.

5.4.2.2 Convoy Driving

Comparisons of energy consumption by the motor, the fuel cell, the battery, and both the fuel-cell and the battery obtained by the co-optimization and the sequential optimization during the Convoy driving for different driving times are presented in Figs. 5.7(a)–(d). The results show similar trend as observed for the Churchville-B driving shown in Fig. 5.4. However, the energy savings by co-optimization in the Convoy driving are much smaller than those in the Churchville-B driving; specifically, the maximum energy saving via co-optimization is found to be 5.3% only.

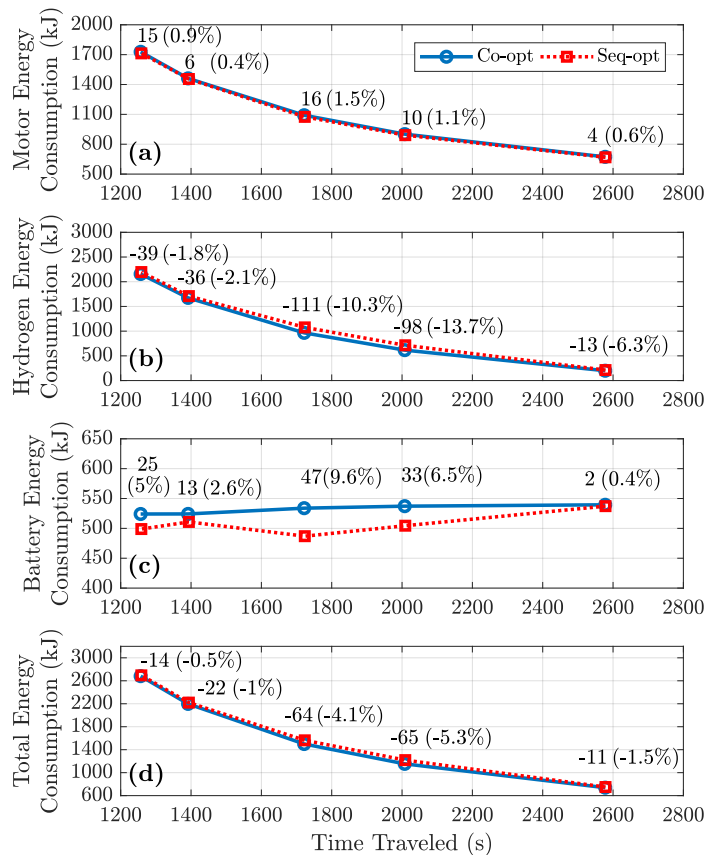


Figure 5.7: Comparison of energy consumption obtained by co-optimization and sequential optimization for various times traveled on Convoy road. (a) energy consumption by the motor, (b) energy consumption by the fuel cell, (c) energy consumption by the battery, and (d) the total energy consumption by the fuel cell and the battery.

This small benefit in energy saving by co-optimization can be explained from the trajectories

of the vehicle speed and the battery SOC for two driving times presented in Fig. 5.9, in which Figs. 5.9(a) and (b) show the results for the shortest cycle while Figs. 5.9(c) and (d) show those for the longest cycle. As seen from Fig. 5.9(a), for the shortest cycle, both optimization approaches use the so-called *Pulse-and-Glide* operation in a very similar way. Note that this Pulse-and-Glide operation is one of the most typical energy-efficient driving strategies for proper roads in the plains or with a slope less than 2% [152, 48]. In this operation, the vehicle accelerates quickly to a higher speed and then keeps coasting or gliding as a result of the vehicle’s kinetic energy stored in the period of acceleration. Because of this similar driving pattern, the resulting SOC trajectories obtained from both optimization approaches become similar as well (see Fig. 5.9(b)). For the longest cycle, very similar trajectories in vehicle speed and battery SOC are observed as shown in Figs. 5.9(c) and (d), respectively. It can be also found that Pulse-and-Glide operation is not preferred in relatively low speed operation for both co-optimization and sequential optimization.

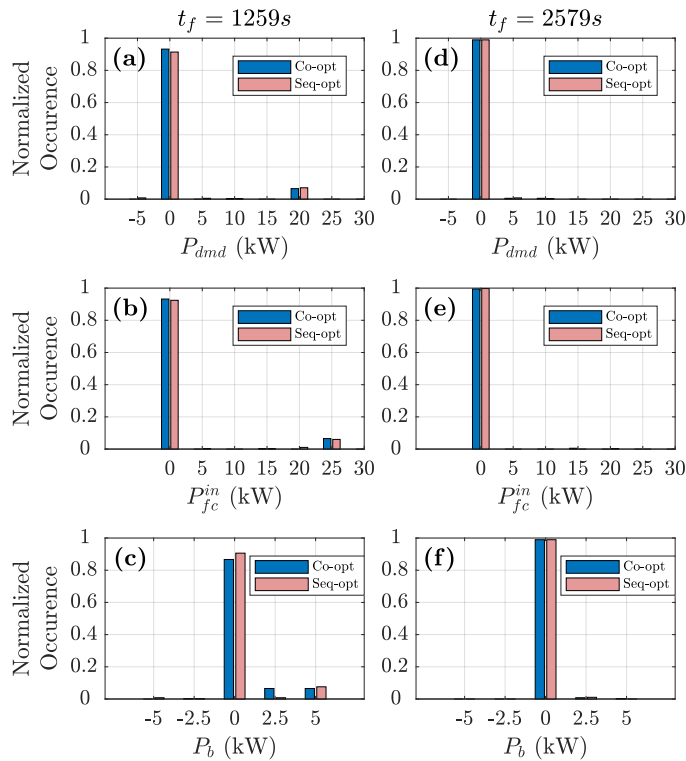


Figure 5.8: Histograms of normalized occurrence of powertrain operation obtained by co-optimization and sequential optimization on the Convoy cycle for two driving times. (a) motor power demand, (b) fuel-cell input power, and (c) battery power with $t_f = 1259s$; (d) motor power demand, (e) fuel-cell input power, and (f) battery power with $t_f = 2579s$.

Since both co-optimization and sequential optimization find similar solutions, the normalized occurrences of powertrain look also similar for both shortest and longest cycles. Especially, for

the shortest cycle, the Pulse-and-Glide strategy dominates vehicle operation. To provide the high propulsion power, both fuel-cell and battery need to be used as shown in Figs. 5.8(a)–(c). On the other hand, for the longest Convoy cycle the fuel-cell is hardly used for both co-optimization and sequential optimization since power demand is sufficiently low such that the battery can only provide propulsion and braking power, as seen from Figs. 5.8(d)–(f).

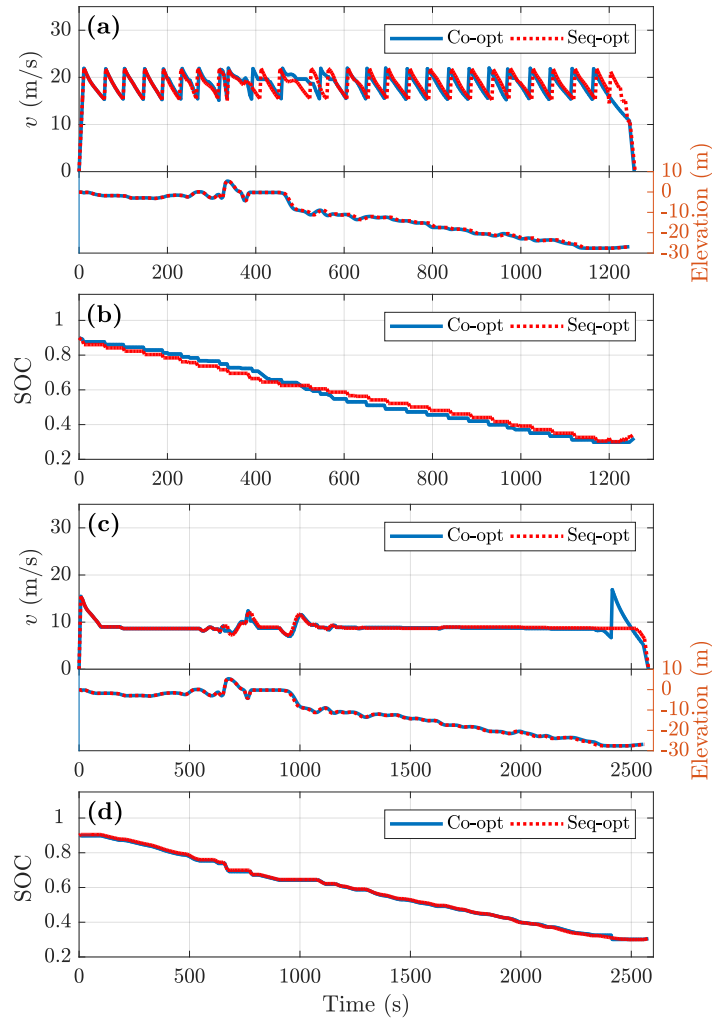


Figure 5.9: Comparison of vehicle and powertrain operation obtained by co-optimization and sequential optimization over the Convoy cycle for travel times of 1259 and 2579 seconds. (a) vehicle speed, (b) electrical power demand by the motor, (c) power consumed by the fuel cell, (d) power provided by the battery, and (e) battery SOC.

5.5 Conclusion

This chapter investigates the co-optimization and sequential optimization approaches for determining the speed profile and power-split of fuel-cell/battery hybrid electric systems based on Dynamic Programming. In order to reduce computational cost for Dynamic Programming, the optimal control problem is reformulated and analyzed by applying Pontryagin's Minimum Principle to reduce the number of control input combinations. It is found that the simplification of the battery SOC dynamics leads to the use of discrete vehicle control modes, similarly to [10]. This result allows for a substantial decrease in computational cost of Dynamic Programming. To further reduce computational load, the original co-optimization problem is modified by eliminating the state variable corresponding to time and adding a penalty on operation time instead. Then, two specific driving scenarios for a military ground vehicle over the Churchville-B Cycle and Convoy Cycle are simulated to compare the two approaches in terms of energy consumption. The total energy savings by co-optimization range from 5.3% to 24.2% for aggressive driving on a hilly terrain. Meanwhile, on a relatively flat road, the benefit of co-optimization is less significant. Nonetheless, co-optimization achieved 0.5%-5.3% reduction in total energy consumption as compared to sequential optimization.

CHAPTER 6

State of Charge Estimation for LFP Chemistry Cells

6.1 Introduction

The primary function of the battery management system (BMS) is to provide an accurate state of charge (SOC) estimation. The SOC represents the amount of charge in ampere-hours (Ah) remaining in a cell divided by its total capacity [28, 125]. The BMS traditionally uses current, voltage, and sometimes temperature measurements to estimate the SOC to plan future actions and to prevent over-charging or discharging of cells. Generally, manufacturers provide conservative estimates of remaining energy, since an overestimation of SOC can leave the vehicle stranded. In the case of unmanned air vehicles (UAV), overestimation of SOC might prevent the vehicle from safe landing, since landing maneuvers require very high power, which typically cannot be achieved at very low SOC levels [27]. Underestimating SOC, on the other hand, wastes valuable resources and adds cost and weight to the vehicles, which is critical for robotic platforms.

From the lithium ion batteries, lithium iron phosphate (LFP) has been considered for UAV, hybrid electric vehicle (HEV), electric vehicle (EV) and are promising for fuel cell vehicles (FCVs) due to their capacity for fast charging, high power capability, and long cycle life [178]. LFP batteries consists of graphite as the negative electrode and lithium iron phosphate (metal oxide) as the positive electrode [131]. Due to the relative flat half-cell potential the positive electrode exerts (also known as the phase-separating cathode active material) [90], the open circuit voltage (OCV) has a relatively flat slope through most of its operating SOC range (10–95%), as shown in Figure 6.1. The phase transitions in the graphite material correspond to the different voltage plateaus with respect to SOC, as shown in Fig. 6.1a. This makes SOC estimation difficult under noisy environments [161],[169] and inexpensive sensing, such as robotic and automotive applications. Previous work has suggested strain or stress (pressure or force) measurements to augment terminal voltage for SOC estimation [99]. Specifically, the graphite in the negative electrode expands when the lithium ions are intercalating into it, and the positive electrode contracts as the lithium ions leave it causing a change of thickness in the components of the battery [63]. This change in thickness

causes the battery to swell. Therefore, the overall observed cell swelling is the summation of the swelling from the positive and negative electrodes. When the cells are constrained to a fixed displacement, as typical in automotive packs, the battery swelling results in an increased force on the fixture. This swelling force can be measured using a load cell [99].

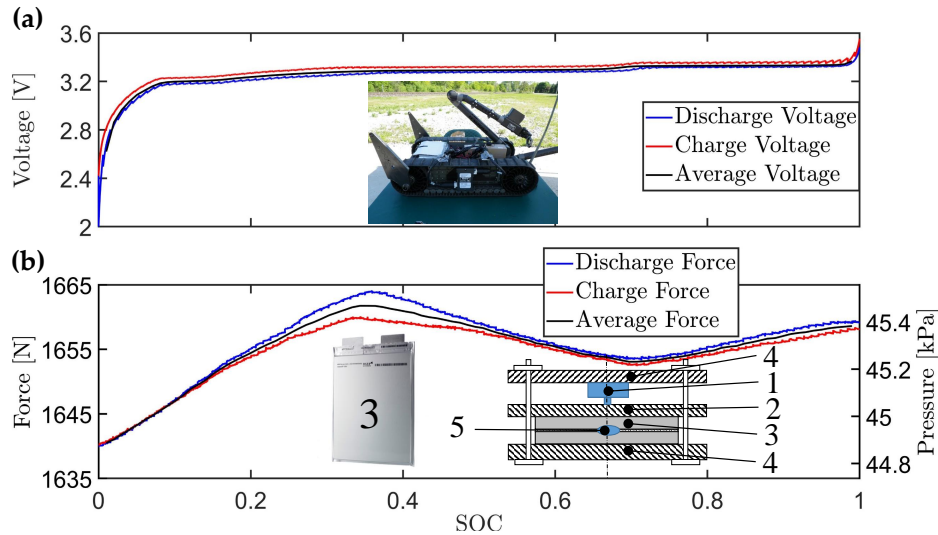


Figure 6.1: Measured voltage and force for the 20 Ah A123 lithium ion iron phosphate battery cycled under low current rate $C/20$. **(a)** Measured discharge (blue), charge (red), and average of discharge and charge (black) voltage for a $C/20$ cycle. For military robots such as the Packbot shown above, SOC estimation is critical to avoid the robot getting stranded. Lithium ion iron phosphate (LFP) batteries are typically used for operation of this robot due to the high power required. **(b)** Measured discharge (blue), charge (red), and average of discharge and charge (black) force for the under current rate $C/20$. The experimental battery fixture consists of: (1) load cell (force sensor); (2) movable plate; (3) lithium ion battery; (4) two aluminum end-plates; (5) temperature sensor. For generalization of the results to the other cell sizes, the force measurements can be converted to pressure by dividing the force by the surface area of our battery (A_b), which is the width ($w_b = 0.161m$) times the length ($l_b = 0.227m$) of the battery, $A_b = w_b \times l_b m^2$.

The structural changes of this expansion have been studied from the electrode mechanics point of view with respect to strain/OCV coupling [63, 18]. The overall volume change of this expansion results in a monotonic function of SOC for a nickel manganese cobalt (NMC) graphite cell [108]. By measuring the force produced by the expansion and including it in the estimation algorithm, improved SOC accuracy can be achieved as compared to voltage based methods [98, 99]. The greatest benefits were observed in the 30–50% SOC region, where the voltage slope was relatively flat, but also at the low SOC level, where voltage drops very fast and is challenging to have an accurate model as the battery ages. The change in measured force vs. SOC over many cycles can also inform better estimates of the battery state of health (SOH) [130]. For the LFP-graphite cell studied here, the anode (negative electrode which is graphite) expands during charging but the simultane-

ous higher contraction rate of the cathode (positive electrode which is LFP) results in a combined cell contraction in the middle SOC range. The overall result is a non-monotonic F–SOC behavior, as shown in Fig. 6.1b. Due to the F–SOC non-monotonicity, SOC estimation based on measured force is challenging since multiple SOC equilibrium points can correspond to the same measured force. Additionally, all mechanical measurements (force, pressure, or displacement) even after calibration exhibit drift associated with small changes in material and a shift in the SOC–expansion behavior as the battery ages. Loss of cyclable lithium causes a shift in capacity and a change in the SOC–expansion behavior of the cell. This capacity loss shifts the stoichiometric ratio associated with lithium concentration in each electrode and hence changes the electrode expansion [100] as a function of lithium intercalation (Coulombs stored) and the measured force/pressure versus SOC as the unknown drift addressed here. Moreover the LFP pouch cells used here are supported by poron sheets [5] between the cells instead of the spacers used in [98]. Thermal expansion of the battery and fixture and viscoelastic response of the compliant poron pad introduces an additional aging and drift factor. Predicting and modeling this aging behavior requires extensive resources and is currently by-passed by estimating this unknown bias as proposed in this study. As can be appreciated, the drift is a general problem of measuring the mechanical behavior (force, pressure, or displacement) of all batteries and it is not just a battery chemistry (LFP)-related issue.

Battery cell balancing is critical to extend the range of battery powered vehicles, the pack operating lifetime, and charge and discharge power limits [67]. To achieve fast and accurate cell balancing, accurate SOC estimation is needed [134]. Voltage-based SOC estimation for the LFP chemistry is particularly challenging since the voltage is relatively flat with respect to SOC. The proposed method improves the SOC estimation using leveraging information about the cell expansion and contraction during charging and discharging. Cell-to-cell variability due to aging, as well as the resulting changes in the measured force, was not investigated, but should be the focus of future research. The influence of cell balancing or imbalanced cells in a module whose force is measured should also be further investigated following the initial work by [69]. Since there would typically be only one force (or strain) measurement in a pack of series connected cell, cell balancing techniques [59] will be of high importance.

In this study, we demonstrate the improvement in the SOC estimation of LFP batteries by using mechanical in addition to electrical measurements that can be implemented in packs or modules of both hard encased and pouch cells [71]. A novel solution to the multiple equilibrium SOC points is proposed based on the piecewise linear (PWL) F–SOC characteristic approximation that is further used in a switching gain model-based linear quadratic estimator (LQE) design that consists of a combination of force and voltage measurements [119]. Due to the drift that appears in most force measurements, as shown in Fig. 6.2, the SOC may not be accurately estimated. Therefore a bias state is added to the LQE in order to capture the drift in the force measurement due to un-modeled

changes in battery swelling or creep of the plastic materials. Experimental validation is also performed on the model-based (LQE) controller design using the combinations of force and voltage measurements during realistic battery electric vehicle usage profiles including the Dynamic Stress Test (DST). The performance of a controller designed with a “perfect” model is compared to one with model mismatch in the OCV and F–SOC PWL fit. The simulated model mismatch captures the typical modeling uncertainties or changes in the cell expansion and open circuit voltage due to aging [75].

6.2 Experimental Setup and Force Behavior

The battery considered here for the experimental validation is an A123 20 Ah lithium iron phosphate pouch cell with a voltage range of 3.6–2 V. The fixture, as shown in Fig. 6.1b, consists of an active battery cell (3) (with a temperature sensor on top of it (5)) and a dummy (inactive) cell with a compliant rubber pad in between. The active battery cell and inactive cell consists of a laminated aluminum pouch cell and the rubber pad is a Poron 4701-30 from Rogers, which is 1.14-mm thick. The temperature sensor is a multimeasurand GE sensor that consists of three resistance temperature detectors (RTDs) and one eddy current expansion sensor [71]. The dummy cell and the rubber pad is used as a stress absorber to emulate the conditions a cell might experience in a pack configuration. The purpose of the dummy cell is to simulate the compliance of the whole system. The stiffness of poron is much less than that of the battery, thus the compression of the dummy cell is negligible in terms of the whole system. Therefore, the dummy cell can be used without complicating the force measurement. The dummy cell is held tight by an aluminum bottom end-plate (4), and a movable plate is placed on top of the active cell. This plate has one degree of freedom in the vertical direction with the force sensor (1) placed on top of it. On top of the force sensor, the fixed top aluminum end-plate is bolted to the bottom end-plate to simulate the behavior of a constrained battery pack with fixed distance between the end plates. The force sensor is an Omega (LC305-500) load cell sensor (strain gauge type). The sensor has a 2225 N full scale range with an accuracy of 4.45 N. The load cell and voltage are digitized and recorded by Data Translation DT-9828, which has a voltage accuracy of 2 millivolts. In this study, the force sensor is used because it is cheaper than the displacement sensors [100], but also less accurate. For example, the accuracy of the displacement sensor used in [100] is 1 μm , which corresponds to 0.35 N of compressive force on the poron, while for the Omega force sensor used the accuracy is listed as a percentage of full scale range (4.45 N). The force only accuracy is the important reason for integrating force and voltage information along with performing the bias estimation.

The force plotted against SOC (F–SOC) and the open circuit voltage vs. SOC (OCV–SOC) are measured experimentally using a pulse–relax profile. Specifically, a CCCV charge is applied

followed by a pulse-relax discharge profile, with the current rate of $\frac{C}{20}$ for 12 min (which results in a 1% SOC change) followed by a 1 h of rest period to eliminate the influence of the internal resistance and electrolyte polarization of the battery. The data points at the end of the rest are used to obtain the discharge F-SOC and OCV-SOC. The test is then repeated using charge pulses of equal duty cycle. The average between the measurements at the same SOC from the charge and discharge datasets is obtained for the F-SOC, as shown in Fig. 6.1b. The average F-SOC shown in Fig. 6.1b is modeled in Section 6.3 and is the best fit parameters that match the force inflection points. An average fit is also obtained from data for OCV-SOC and shown in Fig. 6.3a. The values of the fit for the OCV-SOC (average of discharge and charge) and F-SOC can be found in Appendix A.4.

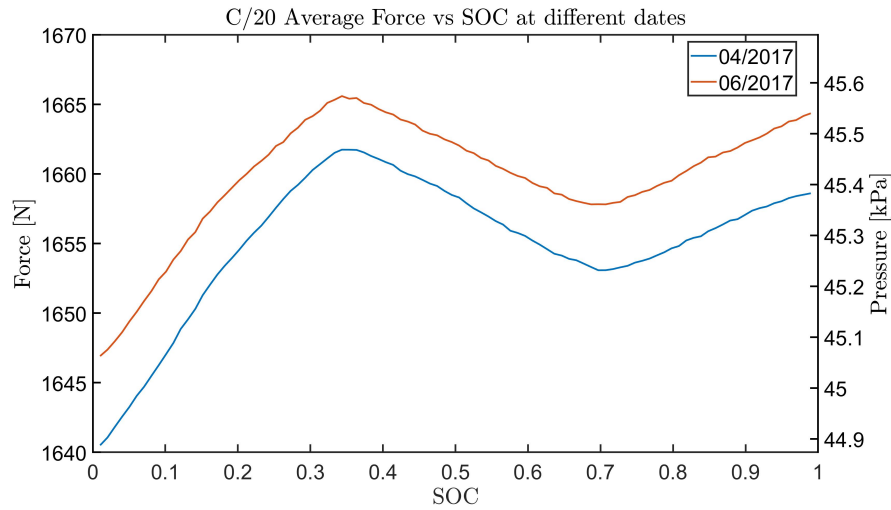


Figure 6.2: Drift in the force sensor can be observed by comparing the force vs. SOC for two $\frac{C}{20}$ cycles which were conducted two months apart with three cycles done in between them with the same battery. The force measurements have a minimum of 3 N and a maximum of 6 N drift across the entire SOC range. The drift could be caused by thermal expansion of the battery, pad, and fixture [98], capacity change, or a combination of all four throughout the life of the cell and module on which measurements are performed. Adjustments in the fixture and changes in the preload will cause larger changes in measured force but can also be modeled as a sensor drift. For generalization of the results to the other cell sizes, the pressure is shown.

An important consideration is the drift observed in the measured force between repeated tests as shown in Fig. 6.2. Two average force cycles with an applied current of $\frac{C}{20}$ at different test dates are shown. These cycles have approximately a minimum 3 N and a maximum 6 N of drift in between the second test (performed on 06/2017 (MM/YYYY)) and first test (performed on 04/2017 (MM/YYYY)). This measurement was taken with the same cell. The drift could be caused by thermal expansion of the battery, pad, and fixture, capacity change or a combination of all four throughout the life of the cell and module on which measurements are performed. That is the reason we

have treated the observed bias as an unknown variable. We assume that this unknown/uncertain-origin drift evolves slower than the force measurement from the charge/discharge changes and we therefore can estimate it as an unknown constant bias in real time. This drift in force can affect the SOC estimation if not compensated and, thus, estimation of the sensor bias is used to improve the practical force based SOC estimation.

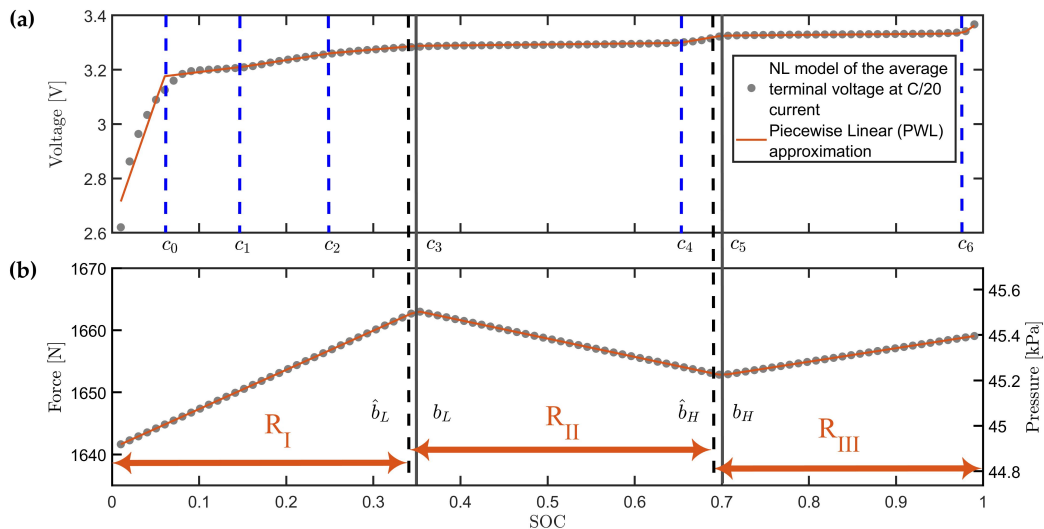


Figure 6.3: A piecewise linear approximation of the (a) open circuit voltage and (b) cell swelling force was fit to the experimental measured values for the A123 Lithium Iron Phosphate Battery Cell. The gray dots correspond to the average of measured data at each SOC point from the charge and discharge cycles at the $\frac{C}{20}$ rate (see Figure 6.1). The orange line represents the PWL fit. The horizontal solid lines represent the inflection points of the cell swelling force. The horizontal dashed black lines represent the inflection points of the cell swelling force used for the developed observers. R_I , R_{II} , and R_{III} represent the force slope regions determined by our PWL model. For the PWL force model, we assume $b_L = c_3$ and $b_H = c_5$ since the changes in voltage and force slopes are due to the intrinsic phase transitions in the material of the battery electrodes [100]. Assessment of the SOC estimator robustness is performed by imposing $\hat{b}_L \neq b_L$ and $\hat{b}_H \neq b_H$ to capture model mismatch for the force and voltage behavior. For generalization of the results to the other cell sizes, the pressure is shown.

For the SOC estimation development, tuning, and comparison, two models with two different levels of fidelity are used:

- The simulation model includes the nonlinearities and hysteresis for the electric characteristics detailed in Section 6.5.
- The observer model ignores hysteresis and uses piecewise linear approximations of the nonlinearities detailed in Section 6.5.

In the next section, the simulation model is detailed and its efficacy is highlighted in Figure 6.4 based on a modified DST cycle [6] that is scaled for a 20 Ah Li-ion battery, as shown in Fig. 6.4a. The DST was chosen because it has a current profile that has the combination of the following C-rates and is representative of usage in an electric vehicle: C/4, C/2, 1C, and 2C. If the utilization of the electrode is relatively uniform, the C-rate should not influence the swelling significantly. The electrode expansion depends on the bulk concentration of the electrode solid phase, as opposed to the terminal voltage which depends on the surface concentration [34] and therefore is less sensitive to C-rate. The theory for determining up to what current density the electrode utilization is uniform can be found based on the porous electrode models by Fuller Doyle and Newman [41] and Newman and Tobias [117]. The largest expected contribution of C-rate dependence (or more precisely root mean square (RMS) current) on the result is through thermal expansion of the cell. The experimental profile consists of a Constant-Current/Constant-Voltage (CCCV) charging protocol at a rate of 1C until the battery is fully charged. After a rest period of 30 min, a 1C rate discharge current is applied until it reaches 61% SOC. After the second rest period of 2 h, the modified DST cycle is applied. The resulting voltage, temperature, force, and SOC are shown in Figs. 6.4b, 6.4c, 6.4d and 6.4e, respectively. The SOC is calculated by Coulomb counting using a high resolution current sensor and assumed to be the true SOC.

6.3 Simulation Model

The models described here include the drift present in our force data and higher dynamics such as hysteresis present in our voltage. These models were simulated to validate the robustness of our developed estimators for analysis purposes before the experimental implementation. After this validation, the estimators were used with experimental data and their performance was evaluated. The battery model used for our simulations is presented in the following subsections. The SOC (z) is simply modeled as

$$\frac{dz}{dt} = -\frac{I}{C_b}, \quad (6.1)$$

where C_b is the cell capacity.

6.3.1 Cell Swelling Force Model (F-SOC)

The force measured at the load cell is modeled using a static non-linearity $F_{sim}(z)$, which is a function of state of charge, with additive bias and noise terms given by

$$F(z) = F_{sim}(z) + v_F + f_d \quad (6.2)$$

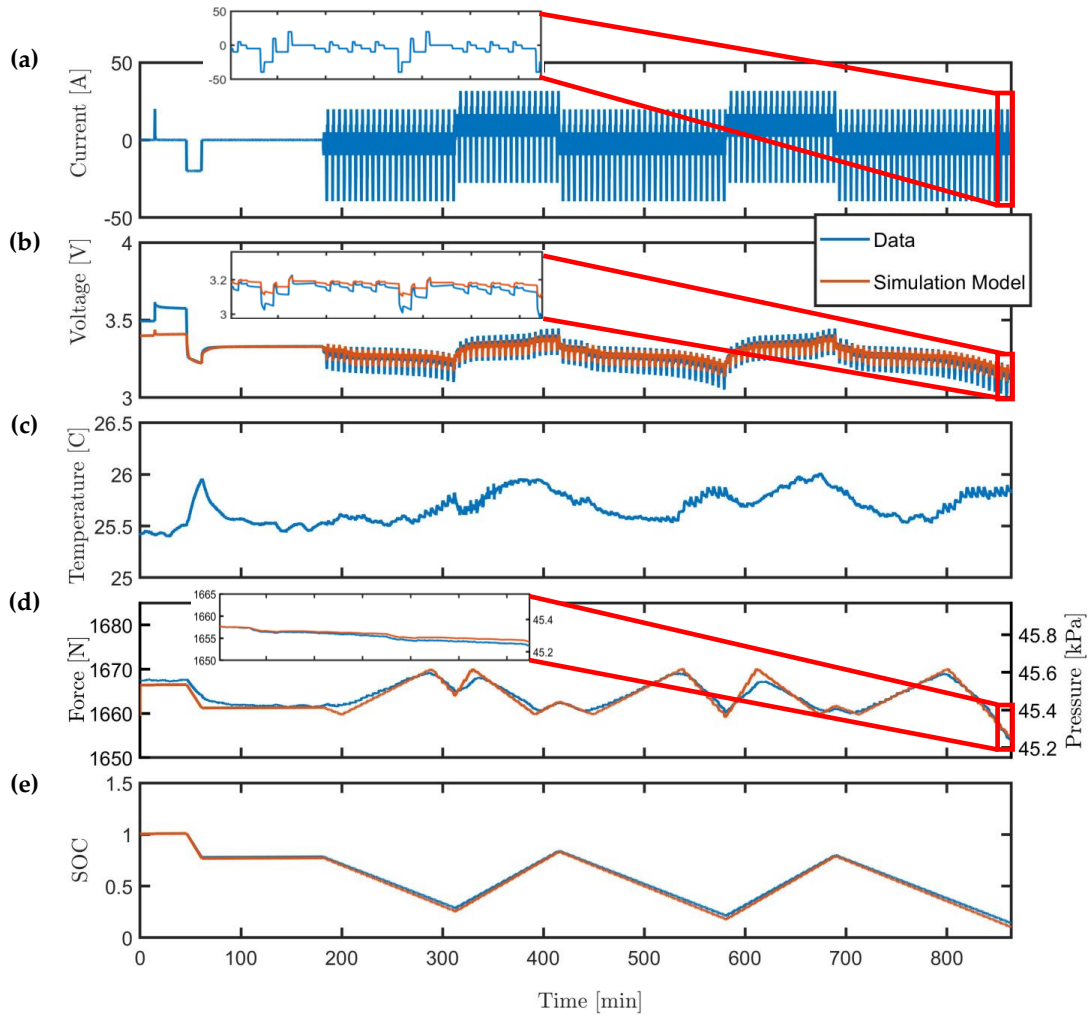


Figure 6.4: Comparison of open loop simulation model results (denoted by the color orange) and experimental measurement of voltage, temperature, force, and SOC obtained from the 20 Ah battery during the Dynamic Stress Test (DST) inside an environmentally controlled chamber set at 25 °C ambient conditions. (a) Current profile scaled for the 20 Ah A123 battery. (b) Comparison of the open loop model terminal voltage and measurement. (c) Measured battery temperature. (d) Comparison of the open loop modeled force and measured force. After 30 min of rest, the unmodeled dynamics in force excited by cycling of the cell to decay to zero. For generalization of the results to the other cell sizes, the pressure is shown. (e) Comparison of state of charge (SOC) measurement.

where $F(z)$ (N) is the measured force that relies on $F_{sim}(z)$, which is the PWL model of the average F–SOC behavior; v_F is the measurement noise; and f_d is a constant drift or bias (assumed to be constant but unknown) value present in our force measurement. A piecewise linear representation of the average F–SOC behavior is given by

$$F_{sim}(z) = C(z)z + C_0(z) = \begin{cases} \alpha_m z + \alpha_{m0}, & \text{if } z \leq b_L \\ \beta_m z + \beta_{m0}, & \text{if } b_L < z \leq b_H \\ \gamma_m z + \gamma_{m0}, & \text{otherwise} \end{cases} \quad (6.3)$$

where α_m , β_m , and γ_m are the slope parameters; α_{m0} is the preload or the force sensed at zero state of charge; and b_L and b_H denote the SOC where a change in the sign of the slope in the PWL model occurs as shown by the solid gray vertical lines in Figure 6.3. These parameter values can be found in Appendix A.4 and can be adjusted to simulate model uncertainty and mismatch. The parameters β_{m0} and γ_{m0} in the PWL model are uniquely determined from the other parameters via constraints of piecewise continuity

$$\beta_{m0} = (\alpha_m - \beta_m)b_L + \alpha_{m0} \quad (6.4)$$

$$\gamma_{m0} = (\beta_m - \gamma_m)b_H + (\alpha_m - \beta_m)b_L + \alpha_{m0}. \quad (6.5)$$

The operating regions R represent the force slope regions determined by our PWL model. The first region is defined as $R_I : \hat{z} \in [0, \hat{b}_L)$, the second region is defined as $R_{II} : \hat{z} \in [\hat{b}_L, \hat{b}_H]$, and the third region is defined as $R_{III} : \hat{z} \in (\hat{b}_H, 1]$. The operating regions are shown in Figure 6.3.

6.3.2 Terminal Voltage Model (OCV-SOC)

The terminal voltage in volts is modeled as

$$V_T = V_{oc}(z) - IR - V_1 - V_2 - V_h + v_V, \quad (6.6)$$

where $R[\Omega]$ is the total equivalent series resistance, I is the discharge current applied to the battery, V_1 and V_2 are the voltages due to the two resistance and capacitance (RC) pairs, and v_V represents the V measurement noise. The OCV characteristic, $V_{oc}(z)$, is SOC dependent and modeled using

$$V_{oc}(z) = V_0 + d(1 - \exp(-fz)) + h \left(1 - \exp \left(-\frac{-k}{1-z} \right) \right) + gz + \sum_{i=1}^3 a_{v,i} \arctan \left(-\frac{z - b_{v,i}}{c_{v,i}} \right), \quad (6.7)$$

where $V_0, g, d, f, h, k, a_{v,i}, b_{v,i}$, and $c_{v,i}$ are tuned parameters found in Appendix A.4. The electric equivalent circuit (EC) battery model [57, 116] is used for the simulation in our observer validation. In this study, voltage hysteresis (V_h) [118] is also considered for the simulation model

$$\frac{dV_1}{dt} = \frac{-V_1}{R_1 C_1} + \frac{I}{C_1} \quad (6.8)$$

$$\frac{dV_2}{dt} = \frac{-V_2}{R_2 C_2} + \frac{I}{C_2} \quad (6.9)$$

$$\frac{dz}{dt} = -\frac{I}{C_b} \quad (6.10)$$

$$\frac{dV_h}{dt} = -\left| \frac{\gamma_h I}{C_b} \right| V_h + \left| \frac{\gamma_h I}{C_b} \right| H(z, \text{sgn}(I)) \quad (6.11)$$

where V_1 and V_2 are the voltages of the RC equivalent circuits, R_1 and R_2 are the resistors, C_1 and C_2 are the capacitors of the RC equivalent circuits, V_h is the hysteresis voltage, γ_h is the hysteresis rate constant, and $H(z, \text{sgn}(I))$ is a function of SOC and the sign of current ($\text{sgn}(I)$) following [118]. The function $H(z, \text{sgn}(I))$ is taken to be half the difference between the charge and discharge OCV measurements, and the parameter values can be found in Appendix A.2. Although the EC model parameters depend on the battery's SOC and temperature, in this study, we do not take this dependency into consideration. The constant parameters of the EC model can be found in Table 6.1. The dynamic equations developed for charge/discharge as well as the measurements in Equations (6.2) and (6.6) is used to simulate the battery behavior, and it is numerically discretized with a time step of $T_s = 1$ s.

Table 6.1: Battery Equivalent Circuit Parameters and its values.

Parameters	Values
R	1.5 mohms
R_1	1.4 mohms
C_1	13,014 farad
R_2	2.7 mohms
C_2	143,000 farad
γ_h	0.00054

6.4 Voltage Model Parameterization

Before using our model for SOC estimation, the average Force–SOC and OCV–SOC needs to be obtained and model parameterization of the equivalent circuit parameters is required using a pulsed

current profile such as the Hybrid Pulse Power Characterization (HPPC) [57]. The pulse current was obtained and the nonlinear programming solver `fmincon` was used to find the parameters provided in Table 6.1. To verify that the parameters are correct, different initialization values were used. From the different initialization values used, `fmincon` converged to the parameters provided in Table 6.1.

6.5 SOC Estimation Model

The linear quadratic estimator (LQE) also known as the steady-state Kalman filter is used for state estimation. The goal of the observer is to find a gain K that converges the initial state to the true state of the system using linear filter equation with measurement error feedback

$$\hat{x}_{t+1} = A\hat{x}_t + Bu_t + K(y_t - \hat{y}_t) \quad (6.12)$$

where the estimated output equation is given by

$$\hat{y}_t = C(\hat{x}_t)\hat{x}_t - C_0(\hat{x}_t) - Du_t \quad (6.13)$$

with $C(\hat{x}_t)$ the slope of the estimated measurement and $C_0(\hat{x}_t)$ the affine parameter based on our model and shown in Figure 6.3. The matrix D is the direct transition (or feedthrough) term. The error dynamics are governed by the eigenvalues of $A - KC$, which depends on the chosen gain K so that it is stable and achieves fast convergence of the SOC estimation error $e = z - \hat{z}$. We use the Discrete Algebraic Riccati Equation (DARE) to find our gain K on all our developed observers. The DARE is defined as

$$P = APA^T - APC^T [CPC^T + R]^{-1} CPA^T + Q \quad (6.14)$$

and solved for the estimation error covariance matrix P . In this equation, Q is the process noise covariance matrix (size $n \times n$) and $R \in \mathbb{R}^{n_y}$ is the measurement noise covariance matrix (size $m \times m$). The values of the diagonal elements of R are chosen based on actual sensor measurement noise variance and Q is tuned so that the desired transient is achieved. The solution of the estimation error covariance (P) for the Kalman filter converges to the solution of Equation (6.14) for $t \rightarrow \infty$ if (A, C) is detectable. In this case, the asymptotically stable observer gain is then computed [77] as

$$K = [CPC^T + R]^{-1} CPA. \quad (6.15)$$

6.5.1 Voltage Only Observer Design

In the case of voltage only estimation, we neglect the hysteresis dynamic term. This represents a typical model mismatch in voltage measurements. The states of the observer are $\hat{x}_t = [\hat{V}_1, \hat{V}_2, \hat{z}]^T$ given by the discretized version of Equations (6.8)–(6.10) and the PWL approximation of the nonlinearities in voltage measurement \hat{y}_t is given by the equations in Appendix A.3. The values of the parameters in the voltage and force models can be found in Appendix A.4. The gain K for this observer is given as

$$K_V = \begin{bmatrix} K_1 & K_2 & K_3 \end{bmatrix}^T \quad (6.16)$$

The values for the gains K_i with $i = 1-3$ are obtained by tuning the Q matrix. The gain K_V is found for the eight regions in which the voltage is divided: $R_1: z \in [0, c_0]$, $R_2: z \in (c_0, c_1]$, $R_3: z \in (c_1, c_2]$, $R_4: z \in (c_2, c_3]$, $R_5: z \in (c_3, c_4]$, $R_6: z \in (c_4, c_5]$, $R_7: z \in (c_5, c_6]$, and $R_8: z \in (c_6, 1]$.

The main challenge in this system is the slow convergence of the estimation error due to the almost zero output gain (in C) especially the C(1,3) that corresponds to the $\frac{dV}{dz}$ in Equation (6.18). Increasing the K_v gain to compensate for the low state to output gain C governed by $\frac{dV}{dz}$ will amplify voltage sensor noise. Therefore, another observer is developed that uses voltage and force measurement since SOC and bias in the force signal are unobservable by force measurement only.

6.5.2 Voltage and Force Observer Design

In the case of force and voltage estimation, the states of the observer are $\hat{x}_t = [\hat{V}_1, \hat{V}_2, \hat{z}]^T$ and $\hat{y} = [\hat{V}_T, \hat{F}]^T$ given by the equations in Appendix A.3. The gains for the V&F observer have the following format

$$K_{VF} = \begin{bmatrix} K_{11} & K_{21} & K_{31} \\ K_{12} & K_{22} & K_{32} \end{bmatrix}^T \quad (6.17)$$

and the gain K_{VF} is found for the eight regions of the voltage, as explained in the previous subsection. The modeled force used for the state estimator, \hat{F} , is given by

$$\hat{F}_{sim}(\hat{z}) = \hat{C}_{dF}(\hat{z})\hat{z} + \hat{C}_0(\hat{z}) = \begin{cases} \alpha_m \hat{z} + \alpha_{m0}, & \text{if } \hat{z} \leq \hat{b}_L \\ \beta_m \hat{z} + \beta_{m0}, & \text{if } \hat{b}_L < \hat{z} \leq \hat{b}_H \\ \gamma_m \hat{z} + \gamma_{m0}, & \text{otherwise} \end{cases} \quad (6.18)$$

where \hat{z} is the estimated SOC from our observer and \hat{b}_L and \hat{b}_H are the inflection points that are shifted by -10% , as shown by the dashed black lines in Figure 6.3 to emulate model uncertainty and aging. In the case of a “perfect” model, $\hat{b}_L = b_L$ and $\hat{b}_H = b_H$.

6.5.2.1 Switching Logic in Observer Design

The gain (K) of the LQE depends on the relationship between the estimated state and the slope of the measurement. In the case of a monotonic function, the estimated state will converge to the true state value when the estimator gain is chosen so that the error dynamics are stable. In the case of a non-monotonic function, the estimated state and the true state can have different slopes in the force output depending on the operating region. Therefore, the estimator gain would have a wrong sign which would lead to the divergence of the estimated state of charge from the true state. This is due to the traditional LQE using the modeled slope at the region of the estimated state. For example, consider the case where the model initialization occurs in the middle section of the SOC range (force decreases and cell contracts as SOC increases), whereas the actual SOC is in the high SOC range (force increases and cell swells as SOC increases); the traditional approach will lead to divergence of the estimated SOC state from the actual SOC due to the difference in slope. To address this difficulty, an algorithm was developed that uses a window of past measurements force data to identify the slope of the non-monotonic F–SOC. The observer gain will need to switch based on a judicious combination of the information at hand, namely

- (a) the modeled slope \hat{C}_{dF} from Equation 6.18 of the F–SOC relation based on the estimated state \hat{z} ; and
- (b) the estimation of the slope by using the measured force with respect to the Coulomb counting based SOC, $\frac{d\tilde{F}}{dz}$ (DFDZ).

Therefore, the output error injection gain K is a function of the state estimate and the estimated force derivative, e.g., $K(\hat{z}, \frac{d\tilde{F}}{dz})$, using two sources of information due to its importance in the convergence of the estimation error. The DFDZ is computed as a line fitting problem based on the moving window of past force measurements and the Coulomb counting based SOC integration (\tilde{z}) over the moving window. The fitted DFDZ line $\tilde{F} = \frac{d\tilde{F}}{dz}\tilde{z} + \tilde{F}_0$ parameters are computed using the least-squares estimation as

$$\begin{bmatrix} \frac{d\tilde{F}}{dz} \\ \tilde{F}_0 \end{bmatrix}_k = (\mathbb{L}_k^T \mathbb{L}_k)^{-1} \mathbb{L}_k^T \mathbb{F}_k \quad (6.19)$$

where \tilde{F}_0 is the affine parameter in Equation (6.18). The moving window of force measurements and the design matrix respectively are defined as follows

$$\mathbb{F}_k = \begin{bmatrix} F_{k-n} \\ F_{k-n+1} \\ \vdots \\ F_k \end{bmatrix}, \quad \mathbb{L}_k = \begin{bmatrix} \tilde{z}_{k-n} & 1 \\ \tilde{z}_{k-n+1} & 1 \\ \vdots & \vdots \\ \tilde{z}_k & 1 \end{bmatrix} \quad (6.20)$$

where k represents the discrete-time measurement index and n is the number of past samples. The Coulomb counting based SOC integration is computed as

$$\tilde{z}_k = \tilde{z}_{k-1} - \frac{I_{k-1}T_s}{C_b}. \quad (6.21)$$

The integration is initialized with $\tilde{z}_{k-n} = 0$. The moving window provides the $\frac{d\hat{F}}{dz}$ computation as the average slope in a window of n prior values of force which causes a delay δ in the switching logic as a function of the window size n , as shown in Figure 6.5d. We can see that for $n = 150$ the δ is smaller compared to $n = 450$, but, with smaller n , the estimated slope is more susceptible to noise. We chose n here to be 150 samples with a discretized time of 1 s. The reasoning behind choosing this window size is explained in Section 6.5.3. Due to this delay and the fact that during this time the actual and the estimated state can be in different segments of the SOC, which could cause divergence, the gain is set to zero when the estimated slope $\frac{d\hat{F}}{dz}$ has a different sign from the modeled slope. Therefore, the system will run open loop for both voltage and force when there is slope mismatch. This is done in order to avoid instability issues.

The switching logic for our gain ($K(\hat{z}, \frac{d\hat{F}}{dz})$) is given by the following rules:

$$K_{VF}(3, 2) = \begin{cases} K_{R_I} & \text{if } \frac{d\hat{F}}{dz} > 0 \quad \text{and} \quad \hat{z} < \hat{b}_L \\ K_{R_{II}} & \text{if } \frac{d\hat{F}}{dz} < 0 \quad \text{and} \quad \hat{b}_L < \hat{z} < \hat{b}_H \\ K_{R_{III}} & \text{if } \frac{d\hat{F}}{dz} > 0 \quad \text{and} \quad \hat{z} > \hat{b}_H \\ 0 & \text{otherwise.} \end{cases} \quad (6.22)$$

Note that the gains K_{R_I} , $K_{R_{II}}$, and $K_{R_{III}}$ are not constant. The set of gains K_{R_I} consists of the four gains that correspond to the four regions in voltage in region R_I , $K_{R_{II}}$ consists of the two gains that correspond to the two regions in voltage in region R_{II} , and $K_{R_{III}}$ consists of the two gains that correspond to the two regions in voltage in region R_{III} , as shown in Figure 6.3. The gains are therefore a function of \hat{z} and $\frac{d\hat{F}}{dz}$ and they switch to the corresponding region depending on the value of the estimated slope and estimated SOC.

6.5.3 SOC Estimation Error during Switching

Going open loop, during the time interval when there is a slope mismatch, is not sufficient to avoid divergence of the estimated state of charge with high feedback gain. To verify this, we analyze the Luenberger Observer for the SOC state using the measured force only. The goal of this analysis is to determine the impact of the gain K on divergence of the state estimate when the true model and state estimate are operating on opposite regions of the output non-linearity. Using Equations (6.12) and (6.13), we can write the error dynamic ($e = z - \hat{z}_t$) for the observer assuming

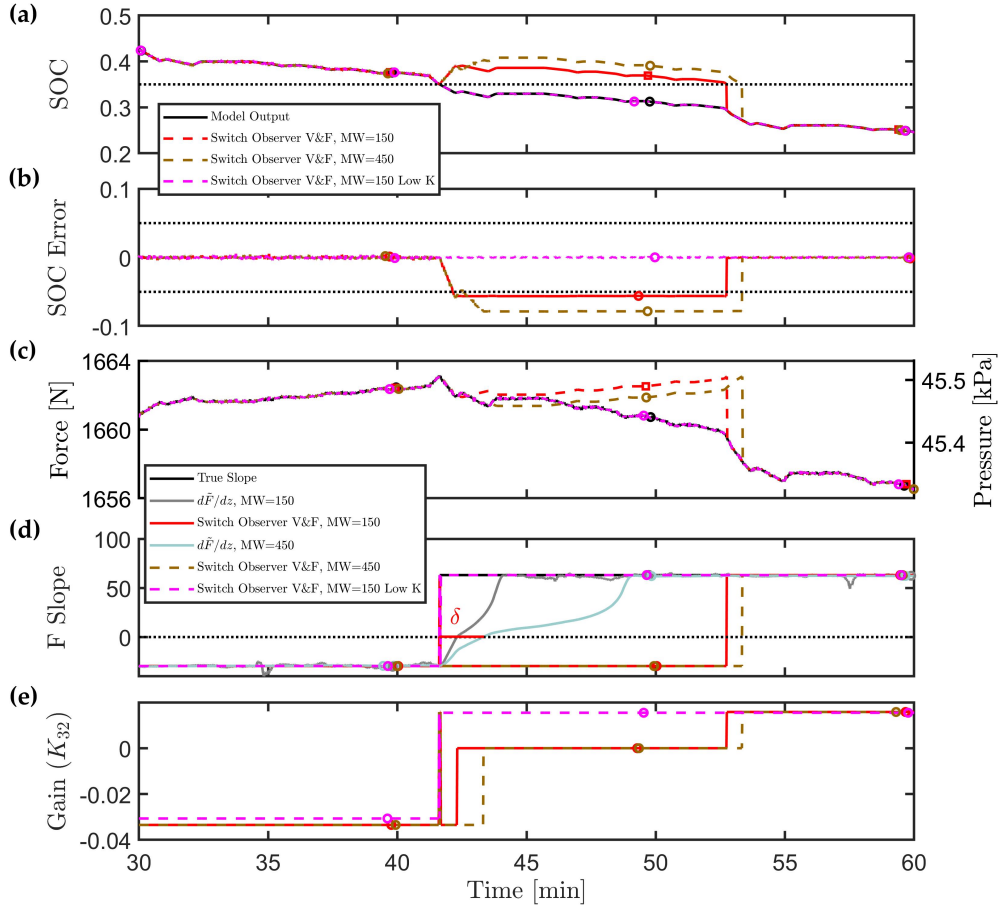


Figure 6.5: Simulation (without bias in the force measurement) for the Switch Observer V&F developed in our previous work [119]. This figure shows the impact of high gains corresponding to solution of the linear quadratic estimator using $Q_1 = \text{diag}([2, 0.1, 0.1])$ and $R = \text{diag}([1, 1])$ with moving windows of length (MW) = 150 and MW = 450. If the gain is lowered by using $Q_2 = \text{diag}([2, 0.1, 1e-2])$, as shown by the purple dashed line, the error is decreased by 5% with same 150pt moving window length. **(a)** Comparison of the simulated state of charge (SOC). **(b)** Comparison of the state of charge (SOC) error with the dashed lines representing the target $\pm 5\%$ bound. **(c)** Comparison of the simulated force. For generalization of the results to the other cell sizes, the pressure is shown. **(d)** Comparison of the true slope with the estimated slope $\frac{d\tilde{F}}{dz}$ and observer output. Due to the greater delay (δ) before applying the zero gain for the MW = 450 case, a higher error in SOC estimation occurs during the transition from R_{II} to R_I . **(e)** Comparison of the feedback gain K_{32} from force to SOC based on the switching logic. When the observer and estimated slopes mismatch, the gain is set to zero.

\hat{x} is in R_I and x is in R_{II} as:

$$\hat{e}_{t+1} = A\hat{e}_t - K(y_t - \hat{y}_t) = A\hat{e}_t - K(\beta_m x + \beta_{m0} - \alpha_m \hat{x} - \alpha_{m0} + \alpha_m x - \alpha_m \hat{x}) \quad (6.23)$$

$$\hat{e}_{t+1} = (A - K\alpha_m)\hat{e}_t - K((\beta_m - \alpha_m)x + \beta_{m0} - \alpha_{m0}). \quad (6.24)$$

From this error dynamic equation, we notice the error converges to a non-zero quantity so that e tends toward zero only when $x = b_L$, and the steady state error $e_{ss} = ((\beta_m - \alpha_m)x + \beta_{m0} - \alpha_{m0})/\alpha_m$ is independent of the gain K . In the case, where the sign of the model is updated based on the measured slope of the force signal ($\frac{d\tilde{F}}{dz}$), the growth in SOC estimation error is bounded by the number of samples in the filter or the moving window size (MW). If the current is bounded (which it is in our case), then the divergence in the state estimate is bounded by the integral of the current and the switching time δ . When the estimator model is updated to the correct slope, the observer begins to converge again. However, noise in the measurement of force could still result in divergence of the estimate if the gain K is too high. This is shown in Figure 6.5. We can see that just by changing the $MW = 150$ to $MW = 450$ by using the same gains given by $Q = \text{diag}([2, 0.1, 0.1])$ and $R = \text{diag}([1, 1])$. This is because the gain is large and the delay in $\frac{d\tilde{F}}{dz}$ crossing zero is 1 min greater than $MW = 150$. Therefore, the divergence in SOC, because of the slope mismatch, will grow for a longer period of time with increasing filter length and a higher error is achieved due to the delay in switching the gain to zero.

Now, if we decrease the gain by using $Q = \text{diag}([2, 0.1, 1 \times 10^{-2}])$ and $R = \text{diag}([1, 1])$ without bias estimation and $n = 150$, we notice that at the same region the error decreases by 5%. Therefore, low gains should be used to avoid the divergence and a window size of 150 is chosen since this is the lowest window that provides sufficient noise rejection. The previous error dynamic analysis can be done for the other mismatch slope areas to determine the minimum SOC state estimation error.

6.5.4 Bias Influence in SOC Estimation

In this section, the proposed estimation is tested under biased force measurements. In Figure 6.6, the simulated force data have a bias or drift of 3 N present in the force measurement. This drift in force affects the SOC estimation, as shown in Figure 6.6. Application of the switched model observer based on voltage and the force measurements based on previous work [119] without taking into account the bias estimation results in error larger than 5%. Therefore, we assumed a constant bias state ($\hat{f}_{d,t}$) that is given by

$$f_{d,t+1} = f_{d,t} \quad (6.25)$$

where $f_{d,t}$ is the constant bias or drift term that augments the electrical states. The estimator now estimated the electrical states (except hysteresis) and the force drift with $\hat{x}_t = [\hat{V}_1, \hat{V}_2, \hat{z}, \hat{f}_{d,t}]^T$. Therefore, the gains for the V&F Bias observer have the following format

$$K = \begin{bmatrix} K_{11} & K_{21} & K_{31} & K_{14} \\ K_{12} & K_{22} & K_{32} & K_{24} \end{bmatrix}^T \quad (6.26)$$

The values for K_{1i} and K_{2i} with $i = 1-4$ are obtained by tuning the Q and R matrices.

6.6 Simulation Results without Model Mismatch in F–SOC and OCV–SOC

The standard Dynamic Stress Test (DST) profile is repeated back to back and modified by adding a constant current to periodically recharge the battery at 1/6 C rate, exercising a wider range of SOC, as shown in Figure 6.4a. A measurement noise variance of 5 mV for voltage and 0.05 N for force was chosen based on the variance of the experimental data. As for the drift value, we chose a value of 3 N based on the monthly drift observed between repeated characterization experiments. Our observer works if the initial error in bias is within 3 N. The LQE estimator is initialized with an SOC error of $\pm 10\%$ in order to evaluate convergence. In the case of the DST cycle, the true SOC state may be approaching the estimated value or diverging from the true SOC value depending on the initial SOC estimation error. The objective is to stay within the $\pm 5\%$ estimation error bound (EEB) for SOC denoted by the dashed lines in the Figure 6.6b . We chose to simulate initial conditions around 60%–80% and the SOC swing of the whole cycle around 20%–80% SOC. This range was chosen due to the challenge associated with flat OCV–SOC profile present for voltage (around 40%–60%) and the negative slope in F–SOC (around 35%–70%). Therefore, the simulated “measured” data are initialized at 61% SOC. The weights chosen to obtain the gains K_{1i} with $i = 1-4$ and K_{2i} with $i = 1-4$ are shown in Table 6.2. The gain K_{32} is shown in Figure 6.6f to illustrate when the algorithm uses the estimated slope mismatch to zero the observer gain and run open loop.

Table 6.2: Control weights for the different sensors using the simulated data. V, terminal voltage; V&F, fusion of both sensors; V&F Bias, fusion of both sensors with bias state.

Models	Q	R
V	diag(2, 10, 2)	50
V&F	diag(2, 0.01, 0.01)	diag(50, 10, 000)
V&F Bias	diag(2, 0.1, 0.01, 4)	diag(50, 10, 000)

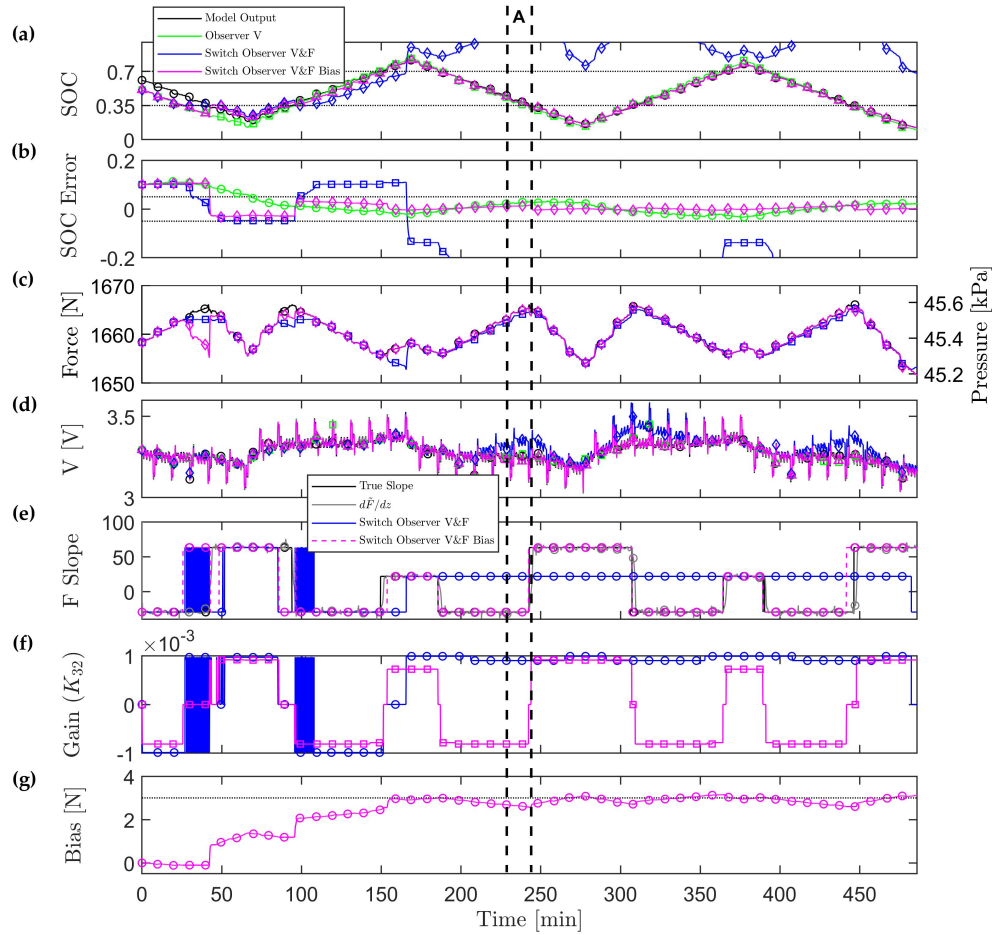


Figure 6.6: Simulation assuming accurate modeling using Switch Observer V&F Bias observer with an emulated bias of 3 N and 10 % (0.1) initial SOC error. **(a)** Comparison of the simulated state of charge (SOC). It is clear from the results that Switch Observer V&F without bias estimation diverges from the simulated SOC. Therefore, bias estimation is needed in the developed observer. **(b)** Comparison of the state of charge (SOC) error with the dashed lines representing the target $\pm 5\%$ bound. SOC errors greater than 20% are obtained with the Switch Observer V&F without bias estimation. It is shown that with bias estimation the SOC error is within the 5% estimation error bound (EEB). **(c)** Comparison of the simulated force and observer outputs. The bias state permits deviation in the force output, without compromising SOC estimation. For generalization of the results to the other cell sizes, the pressure is shown. **(d)** Comparison of the simulated terminal voltage. **(e)** Comparison of the true slope with the estimated slope $\frac{d\tilde{F}}{dz}$ and observer output. **(f)** Comparison of the feedback gain K_{32} from force to SOC based on the switching logic. As shown in region A, denoted by the black dashed horizontal lines, when the observer and estimated slopes mismatch, the gain is set to zero. **(g)** The observer estimates the bias state which converges to the true bias as shown by the black horizontal dashed lines.

The SOC estimation using the V measurement and V&F measurement with and without the bias state estimation are shown in Figure 6.6a. In all three cases, a 10% initial estimation error is assumed. The inflection points in the force with respect to SOC are denoted by the dotted horizontal lines in Figure 6.6a. In this case, the correct values for b_L and b_H are used for the simulated data and the observer. The switched model applies zero gain (as shown in Figure 6.6f in Region A) when the model slope (based on \hat{z}) does not agree with the estimated slope using the least squares on the moving window with Equations (6.19)–(6.20). Using the previously developed V&F observer without bias estimation [119], the SOC error does not remain within the $\pm 5\%$ bound with a 3 N bias in the measurement, even though the error in the force signal is small, as shown in Figure 6.6a and 6.6c. For the proposed switching force-and voltage-based LQE with bias (Switch Observer V&F Bias) before $t = 50$ min there is an SOC estimation error of 10%, even though the force estimation is matching our simulated data, due the error in bias state estimation shown in Figure 6.6g. Between $t = 25$ and $t = 42$ min, there is a slope mismatch in $\frac{d\hat{F}}{dz}$ due to the delay of our moving window. After $t = 42$ min, the slopes match again, and the correct non-zero feedback gain is applied and the state of charge estimation error convergences within our $\pm 5\%$ EEB, as shown in Figure 6.6b. Even though both the proposed switching force and voltage based LQE (Switch Observer V&F Bias) and the LQE based on voltage (Observer V) estimate voltage accurately (as shown in Figure 6.6d, it can be observed that the Switch Observer V&F Bias has faster convergence than the estimate based on V alone, as shown in Figure 6.6b. The faster convergence is due to the addition of the force signal that produces a lower output error injection gain from V to SOC in the regions where the voltage signal has flat slope. It can be appreciated from Figure 6.6g that the bias term is able to estimate the drift value slowly in our force measurement. The slow convergence of the bias estimate to the 3 N value denoted by the dotted black line can be seen in Figure 6.6g. Therefore, as time progresses, the estimated force converges to the modeled data, as shown in Figure 6.6c. This is due to the chosen inflection points in F–SOC function being the same as the modeled data ($\hat{b}_L = b_L = c_3$ and $\hat{b}_H = b_H = c_5$). We can observe that the estimated bias value oscillates around the true bias value. The model error is being attributed to the bias state by the estimation algorithm. The Switch Observer V&F Bias has lower root mean square error (RMSE), faster time convergence to the denoted SOC EEB (referred to as Time to 5% EEB in Table 6.3), and reduced maximum absolute SOC error after the force measurement has converged to an SOC error (referred to as Max SOC Error in Table 6.3) compared to Observer V as shown in Table 6.3. Therefore, the advantage of Switch Observer V&F Bias is the fast convergence in the region of 40%–60% SOC while having more accurate SOC estimation due to the low RMSE values.

Table 6.3: Comparison of the RMSE index for different initial estimate error and different sensors using the simulated data. V, terminal voltage; V&F Bias, fusion of both sensors with bias state.

Initial SOC Error	Parameters	Observer V	Switch Observer V&F Bias
+10%	Time to 5% EEB [min]	67.81	42.44
	Max SOC Error [%]	3.32	3.22
	RMSE	0.0394	0.0337
-10%	Time to 5% EEB [min]	41.33	7.86
	Max SOC Error [%]	5.15	1.54
	RMSE	0.0321	0.0185

6.7 Simulation Results with Inflection Point Mismatch in F–SOC and OCV–SOC

In reality, we do not have a “perfect” model that captures the battery data. Moreover, during aging, the capacity loss shifts the inflection points as compared with the fresh cell. Therefore, to simulate a more realistic application model mismatch is included in the F–SOC and OCV–SOC observer by shifting the inflections points b_L and b_H of by -10% (\hat{b}_L and \hat{b}_H) to represent capacity loss on the negative electrode [100]. During capacity loss, these inflections points shift for both functions of F–SOC and OCV–SOC because they correspond to the electrochemical and mechanical model having the same phase transitions. The aging effect on the swelling as the battery is cycled is that the inflection points will shift by approximately 10%. The proposed V&F bias SOC method will work if the initial unknown bias is within 3 N. The bias estimator will converge to the true value, when the SOC is outside the middle region (where there is a multiplicity of state of charge). A larger error in the initial bias will be “corrected” by visiting 100% or 0% SOC based on the cell voltage feedback. In the middle region (R_{II}), the feedback of force error is split between the SOC and bias in the middle region without a strong feedback from the terminal voltage and therefore can have a persistent SOC error. Checking the observer performance under inflection points mismatch due to capacity loss is important since it captures the robustness needed as the battery ages. Therefore, we want to check the performance of the developed Switching Observer V&F Bias under this model mismatch and both voltage and force have -10% inflections points shift. We initialize our simulated “measured” data at 61% SOC. The weights chosen to obtain the gains K_{1i} with $i = 1-4$ and K_{2i} with $i = 1-4$ are shown in Table 6.4. The gain K_{32} for feedback of the force error to the SOC state is shown in Figure 6.7f. The results from the “perfect” model observer (Switch V&F Bias), as shown in Figure 6.6, are compared with the observer with inflection mismatch (Switch V&F Bias Mismatch).

The SOC estimation using the V measurement and V&F Bias measurement with 10% initial

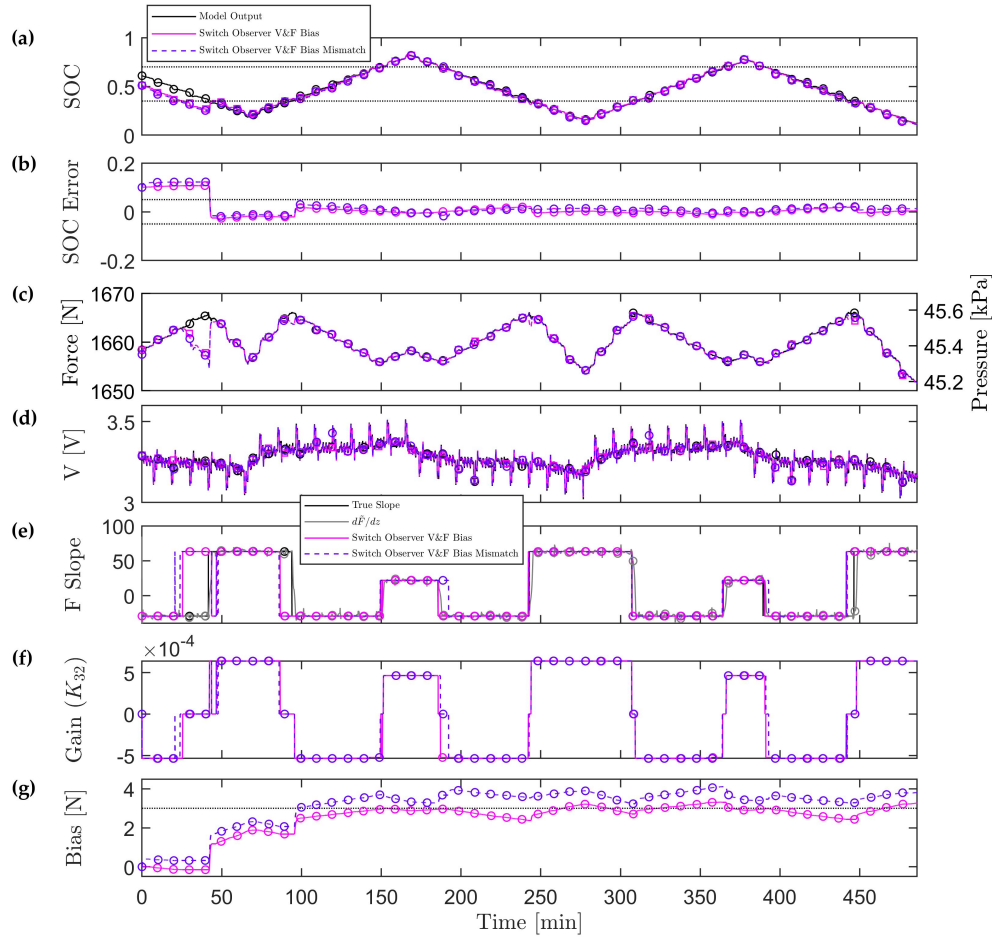


Figure 6.7: Simulation of the impact of model mismatch in the inflection points of the force vs. SOC curve. A 10% error in \hat{b}_L and \hat{b}_H is tested for the observer (Switch Observer V&F Bias) with an emulated bias of 3 N and 10% (0.1) initial SOC error. **(a)** Comparison of the simulated state of charge (SOC). **(b)** Comparison of the state of charge (SOC) error with the dashed lines representing the target $\pm 5\%$ bound. The SOC error converges to within the $\pm 5\%$ error bound. The largest SOC errors are observed near the switching points denoted by the horizontal dashed lines in 6.7a. **(c)** Comparison of the simulated force and observer output. For generalization of the results to the other cell sizes, the pressure is shown. **(d)** Comparison of the simulated terminal voltage and observer output. **(e)** Comparison of the true slope with the estimated slope $\frac{d\tilde{F}}{dz}$ and observer output. **(f)** Comparison of the feedback gain K_{32} from force to SOC based on the switching logic. The gain is set to zero when there is mismatch in the estimated slope and that based on the observer SOC. **(g)** The Bias state estimate converges slowly. The impact of model mismatch in the inflection points of the force vs. SOC curve can be seen by comparing the (Switch Observer V&F Bias Mismatch) and (Switch Observer V&F Bias) which uses the correct value. The accurate observer converges to the true value of 3 N, denoted by the dashed horizontal line whereas mismatch leads to a constant over-estimate of about 1 N.

Table 6.4: Estimation Weights for the different sensors using the simulated data with and without model mismatch. V&F Bias fusion of both sensors without mismatch; V&F Bias Mismatch, fusion of both sensors with model mismatch.

Models	Q	R
V&F Bias	diag(9, 0.01, 0.005, 3)	diag(50,10,000)
V&F Bias Mismatch	diag(9, 0.01, 0.005, 3)	diag(50,10,000)

estimation error are shown in Figure 6.7a. The inflection points in the force with respect to SOC are denoted by the dotted horizontal lines in Figure 6.7a. As shown in Table 6.5, we obtain lower RMSE, faster convergence to the desired SOC estimation error bound (EEB), and smaller absolute SOC error after the force measurement has converged to an SOC error value for the V&F Bias observer compared to V&F Bias Mismatch observer when initialized at 10%. For -10% SOC initialization, the V&F Bias Mismatch observer has lower RMSE and lower time convergence to the desired SOC estimation error bound (EEB) compared to V&F Bias, as shown in Figure 6.7b. The force bias estimate for V&F Bias Mismatch converges faster to the constant bias value of 3N. Due to this faster convergence, the RMSE and the convergence to the desired SOC estimation error bound (EEB) is lower for the model with mismatch due to the initial condition. In both -10% and 10% SOC initialization, the maximum absolute SOC error after the force measurement has converged to an SOC error lower for V&F Bias than V&F Bias Mismatch. The non-zero state estimation error is due to the mismatch present in the F–SOC and OCV–SOC function ($b_L \neq c_3$ and $b_H \neq c_5$). To understand this, we need to analyze the error dynamics equation. We know from Section 6.3 the form of our model and the observer form is given in Equation (6.12). Therefore, denoting our error as $e = x - \hat{x}$ and using our model and observer model equations, we obtain the dynamic error equation as

$$\dot{e} = (A - KC)e - K\Delta C\hat{x} - K\Delta C_0 \quad (6.27)$$

where $\Delta C = C - \hat{C}$ and $\Delta C_0 = C_0 - \hat{C}_0$. From the dynamic error equation, we notice that the bias error and the SOC error will not converge to 0 due to the terms $-K\Delta C_0$. Therefore, the bias will converge to a value that is not the true value of the drift due to this error, as shown in Figure 6.7g. The SOC error will converge to a value but it will not converge to 0, as shown in Figure 6.7b, due to the model mismatch. The magnitude of the estimation error varies depending on the force region we are operating in. The SOC estimation error, due to model mismatch, will grow as the force sensor drift increases due to the terms $-K\Delta C_0$. For the given model tuning and 10% shift in the force curve with respect to SOC, the force-based observer only achieves better SOC estimation than the voltage only case if the uncorrected force sensor drift is less than 3 N initially.

Table 6.5: Comparison of the RMSE index for different initial estimate error and different sensors using the simulated data with and without model mismatch. V, terminal voltage; V&F Bias, fusion of both sensors; V&F Bias Mismatch, fusion of both sensors with model mismatch.

Initial SOC Error	Parameters	Observer V&F Bias	Switch Observer V&F Bias Mismatch
+10%	Time to 5% EEB [min]	42.5	42.55
	Max SOC Error [%]	2.79	3.01
	RMSE	0.0327	0.0377
-10%	Time to 5% EEB [min]	8.38	5
	Max SOC Error [%]	2.38	4.31
	RMSE	0.0200	0.0177

6.8 Experimental Data Results Using F-SOC and OCV-SOC

Table 6.6: Control Weights for the different sensors for data validation: V, terminal voltage; V&F Bias, fusion of both sensors.

Models	Q	R
V	diag(5, 0.1, 0.1)	50
V&F Bias	diag(1, 1×10^{-2} , 0.09, 50)	$R = \text{diag}(50, 10, 000)$

With a 10% initial error in our SOC estimate, we obtain the results shown in Figure 6.8. The observer was initialized to 51% SOC, whereas the true state was 61% SOC, to highlight the performance in the middle SOC region where voltage based techniques are less effective. The current waveform discussed in Section 6.2 was applied to the battery and the observer. As in the simulated results, the proposed Switch Observer V&F Bias has faster convergence than the SOC estimation based on V alone as shown in Figure 6.8b. The V&F Bias observer exhibits lower RMSE, faster time convergence to the denoted SOC estimation error bound (EEB), and reduced maximum absolute SOC error, as shown in Table 6.7 compared to V observer. The bias term oscillates around the estimated bias value of 6.8 N, as shown in Figure 6.8g. These larger oscillations in the bias could be due to our force data having additional dynamics besides the bias term. According to [98], the force has a dynamic term that is temperature dependent, and the ambient chamber temperature may oscillate within ± 1 °C. Therefore, this dynamic term should be added to our force model. There are some large errors in SOC estimation (approximately around 15%) at low SOC. This is due to our piecewise linear (PWL) fit.

In the area near 20% SOC, the PWL fit is less accurately, as shown in Figure 6.1, which results in increased SOC estimation error of around 10%. To better capture the non-linearity, the piecewise linear approximation could be further divided into more regions to provide a better fit. The weights

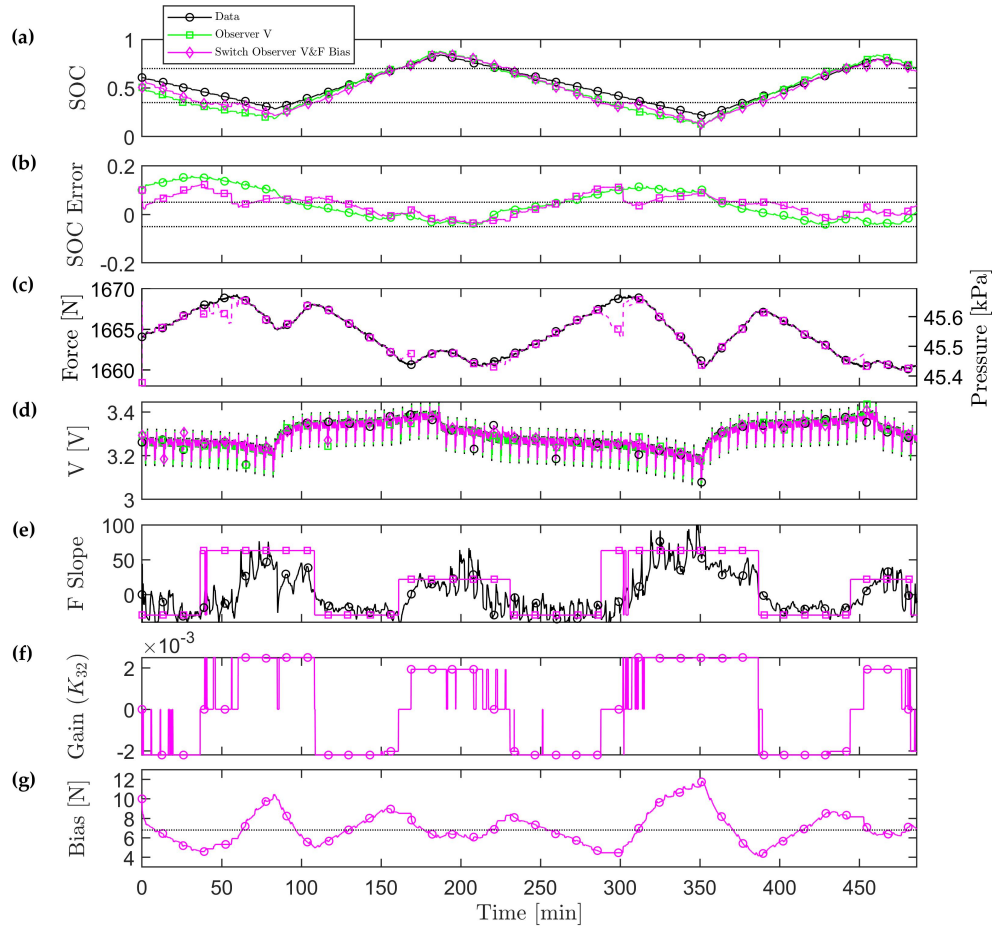


Figure 6.8: Experimental validation of the developed observer (Switch Observer V&F Bias) with 10% (0.1) initial SOC error. The offline experimentally measured current, voltage, and force data were fed into the model to assess performance. **(a)** Comparison of high accuracy coulomb counting based state of charge (SOC) with observer estimates. **(b)** Comparison of the state of charge (SOC) error with the dashed lines representing the target $\pm 5\%$ bound. The observer with force bias state estimation demonstrates better performance. The large error at low SOC for both observers is due to model mismatch the piecewise linear OCV–SOC fit at low SOC. **(c)** Comparison of measured and estimated force. **(d)** Comparison of the experimental and observer modeled terminal voltage. **(e)** Comparison of the estimated slope $\frac{d\tilde{F}}{dz}$ and observer model. **(f)** Comparison of the feedback gain K_{32} from force to SOC based on the switching logic. **(g)** The Bias state estimate fluctuates around the average value (denoted by the horizontal dashed line). This could be due model mismatch, where the force error is exciting the bias state estimate.

Table 6.7: Comparison of the RMSE index for different initial estimate error and different sensors for data validation. V, terminal voltage; V&F Bias, fusion of both sensors.

Initial SOC Error	Parameters	Observer V	Switch Observer V&F
+10%	Time to 5% EEB [min]	95.5	0.18
	Max SOC Error [%]	11.89	11.79
	RMSE	0.0741	0.0611
-10%	Time to 5% EEB [min]	6.95	6.54
	Max SOC Error [%]	11.89	11.79
	RMSE	0.0594	0.0574

chosen to obtain the gains K_{1i} with $i = 1-4$ and K_{2i} with $i = 1-4$ are shown in Table 6.6. The gain K_{32} that satisfies sign or is zero is shown in Figure 6.8f. The bias estimation state is initialized at 10 N.

6.9 Conclusions

LFP batteries have low resistance and thus can be used for load leveling in hybrid FCVs. A new switching estimator design for a battery with the lithium ion LFP chemistry that integrates the non-monotonic F-SOC relation is proposed, verified by simulation, and validated using experimental data with respect to the SOC estimation accuracy. The estimator is based on switching PWL models that are scheduled according to the identified slope of the F-SOC operating point with a bias state in order to capture the drift exerted by the fixture and battery in our force measurement. Two different sensor scenarios, namely V and V&F Bias fusion, are compared, where it is concluded that the V&F Bias sensor improves the rate of SOC estimator convergence. This is due to the information added from the steeper, hence more informative, F-SOC characteristic than OCV-SOC relation despite large errors in the voltage and force models. The bounds on SOC estimation accuracy depend on the chosen inflection points of the F-SOC function. If they are correct, then the accuracy is better for the observer with both F and V than V only. Our future work will focus on determining if the drift on our force measurement is due to creep exerted by the poron and thermal expansion of the fixture or due to creep exerted by a degraded battery influenced by compressive stresses [114], or a combination of both. The thermal expansion term and swelling dynamic as a function of temperature will be considered. Data from an aged swelling cell will be used with the developed SOC estimator and the State of Health of the battery (SOH) will be estimated through the capacity fade. The inflection point model mismatch on the F-SOC function will be further studied in an aged cell since the inflection points change as the battery degrades or fades. Due to the tight manufacturing tolerances, the variability in thickness should not be a significant con-

tributor to force measurement uncertainty. In terms of aging, the expected variability in the cell expansion is a subject of future studies. Cell-to-cell variability due to aging in the resulting force should also be investigated in future work based on initial findings from [100, 130]. Finally, the measured force is the result of all cell's expansion (summation) in a constrained module, therefore different levels of degradation for individual cells when charged in series would result in smoothing (convolution) of the force sensed on the module-level.

CHAPTER 7

Conclusion and Future Work

7.1 Results and Conclusions

Alternative vehicle configurations that transition from internal combustion engines and fossil fuels to alternative power sources with low-carbon intensity fuel are pursued to achieve zero tailpipe emission and reduce the overall carbon emissions. For vehicles with heavy duty cycle and continuous operations fuel cell vehicles are viable candidates and their performance and durability has improved in the last decade. From the different available fuel cells, the polymer electrolyte membrane fuel cell (PEMFC) is the most promising in the automotive sector due to its high efficiency, high power density, low operating temperature, and rapidly decreasing cost. As the cost of the material in the fuel cell (FC) membrane electrode assembly (MEA) is rapidly decreasing, a significant fraction of the cost is occurring due to the balance of plant (BOP) hardware. The BOPs large cost in turn arises from the thermal management system and the airflow systems. Fuel cells produce significant heat that can lead to fuel cell degradation if it is not adequately dissipated. Therefore, the challenge of what cooling system (also known as balance of plant components) should be used with the fuel cell, the influence of fuel cell temperature in the performance of the fuel cell, and the connection to the BOP to maintain the temperature arises. Modeling techniques with empirical maps can be efficiently used for BOP studies and system efficiency. Automatic sizing of the BOP components is much harder and requires a lot of experience or more work. Special attention could be applied to the airpath and compressor. In this thesis, the cooling system was modeled for an aircooled system since it affects the FC efficiency in a significant and complex way. The power split was emulated between the fuel cell stack and a battery for both systems.

An empirical fan model is developed for the Ballard 1200 ACS stack, while the liquid cooled uses an empirical model for the air compressor. The cooling BOP is not considered for the liquid cooled stack due to its low power demand compared to the whole fuel cell system. It was concluded that the cooling system could not be neglected for air cooled fuel cells. Meanwhile, for liquid cooled fuel cells, it can be assumed that the cooling system can be neglected in the fuel cell system

analysis. Determining at what power and energy density the liquid cooling system is cost effective or reduces the total cost of ownership will be important in the future.

The question of what control strategy should be used for real-time implementation while achieving the optimal power split between the energy sources in the fuel cell vehicle and minimizing the fuel consumption is formulated in this thesis. A comparison between an optimal control strategy (using pseudospectral methodology from Matlab called GPOPS) and proportional-integral (PI) controllers were developed for a Packbot robot operated by fuel cells and a lithium ion battery pack. The first PI controller loop consists of controlling the airflow through a fuel cell temperature reference, while the second loop consists of controlling the fuel cell current through state of charge (SOC) reference. The PI controllers use a temperature setpoint suggested by the optimal FC temperature and a linear reference for the SOC. The two PI controllers' performance using the simple reference derived from the offline optimal results can achieve 96% of the fuel savings of the optimum hydrogen consumption with full preview information.

Military vehicles range from 300 W robots to 250 kW armored medium duty vehicles. These vehicles also need to operate efficiently in varying environmental conditions affecting fuel cell operation, such as, the power split strategy, sizing, battery chemistry, and fuel cell vehicle conditions should be investigated. In this thesis, two approaches for the power split are compared. The strategies include dynamic programming (DP) and equivalent consumption minimization strategy (ECMS) for a plug-in hybrid fuel cell medium-sized military vehicle over three different drive cycles (two military drive cycles one emulating a high pulsed power and a commercial drive cycle obtained from actual driving data). For the performance comparison, first, the size of the battery and fuel cell is fixed. Then, different battery sizes and chemistries are considered to study their impacts on fuel consumption and, consequently, on the control strategies. From the obtained results from DP and ECMS for all drive cycles, it is concluded that ECMS is a good candidate for real-time implementation since it performs similarly to DP once a rough mission is known and the SOC trajectory can be determined in advance. The similarity in performance is due to our problem formulation being convex in fuel cell hydrogen consumption and concave with the state of charge time derivative. For the same battery and fuel cell size, the commercial drive cycle (highway cycle) barely used the fuel cell. As for the battery sizing results using Churchville B (the most demanding military cycle), it is demonstrated that there is an ideal battery sizing for the vehicle. For our case study, it seems 28 KWh is the ideal battery size. Taking into account the battery chemistry, lithium ion iron phosphate (LFP) seems to be preferable to lithium-nickel-manganese-cobalt-oxide (NMC) since LFP has lower battery losses and uses less the fuel cell than NMC.

Additional to the power split problem, the optimization of vehicle dynamics and the power split has been a focus for the automotive industry. For military missions there are more reasons for autonomous operation, where, the co-optimization of vehicle dynamics (speed) and powertrain

operation is achieved and the computational complexity added. Consequently, studies have performed sequential optimization where the optimization problem is split in two. First, the optimal speed problem formulation is solved, and then the optimal speed is used to find the vehicle's power for each component. This thesis compares co-optimization and sequential optimization in terms of energy consumption by each powertrain component, operating modes, and computational cost for a hybrid liquid-cooled fuel cell with battery Small Multipurpose Equipment Transport (SMET) vehicle. The calculations for co-optimization are simplified by using Pontryagin's Minimum Principle (PMP) to find a discrete variable describing vehicle operation and another continuous variable for power distribution. We use DP to solve the co-optimization and sequential optimization formulations with two driving cycles (one represents aggressive driving on hilly terrain while the other represents driving on a relatively flat road). It is shown that co-optimization outperforms sequential optimization. The hilly terrain improvements range from 5% to 24% by using co-optimization in total energy savings, while a maximum of 5% was achieved on the flat road. The work was published in [68].

Lastly, even though LFP is promising for fuel cell vehicles due to their ability for fast charging, high power, and long cycle life, it suffers from having a relatively flat (low slope) open circuit voltage OCV-SOC relationship, making it hard to estimate the SOC from the classical voltage measurements. In this thesis, the force expansion is leveraged as an extra measurement to estimate the SOC. The force has a non-monotonic F-SOC relationship making it challenging for the traditional linear quadratic estimator (LQE) to find the correct SOC. Therefore, a novel switching estimation gain is used to determine the gain by the operating region that corresponds to the current SOC. Additionally, a drift in the measured force associated with a shift of the cell SOC-expansion behavior over time is addressed with a biased estimator for the force signal. The performance of our voltage and force-based (V&F) SOC estimation algorithm is compared against the traditional voltage-based (V) using a dynamic stress test protocol. The obtained results show that the V&F Bias sensor improves the rate of SOC estimator convergence compared with the classical voltage-based (V). The work was published in [37].

7.2 Future Work

In this thesis a 0-D model was used to capture the behavior of a liquid cooled fuel cell (15kW Hydrogenics stack HD 15) stack. In the future, the same 0-D model should be used for the air cooled fuel cell (Ballard 1200 ACS) stack and validated against transient temperature and voltage data for both liquid cooled and air cooled stack. That way the same model would capture the behavior of both fuel cells and simplify the modeling analysis.

The PI controller loop consisting of controlling the airflow through a fuel cell temperature

reference, while the second loop consists of controlling the fuel cell current through a state of charge (SOC) reference, was developed. It was corroborated in this thesis that the controllers can perform similarly to an optimal control strategy if the reference is derived from the optimal control results. Therefore, next steps should involve the use of adaptive reference control and validate the controllers in real-time using the hybrid electric vehicle to verify that the appropriate gains are used for each cycle.

It would be interesting if, for the medium size military vehicle, the thermal analysis of the battery is included in the battery sizing analysis between NMC and LFP. The nonlinear LFP open-circuit voltage should also be considered to obtain a more realistic comparison. Including fuel cell sizing in the analysis will be ideal since it will change the weight of the vehicle and power requirements. More battery sizing and fuel cell sizing cases will be considered to validate that the sizing is optimal. The influence of power electronics system (such as DC/DC converter) should also be included in the problem formulation.

For the co-optimization and sequential optimization formulations, future work will concentrate on enforcing a terminal SOC constraint properly for sequential optimization and obtain results that can approximate the co-optimization result [24]. The influence of thermal systems and power electronics systems (such as DC/DC converter) should be included in the vehicle formulation for a more realistic modeling configuration. The effects of battery degradation and fuel cell durability should also be included [167]. Machine learning techniques can be used to deal with a system with many states and uncertainties in the co-optimization problem formulation with the degraded fuel cell and battery models.

Lastly, our voltage and force-based (V&F) SOC estimation algorithm should include a thermal expansion term and swelling dynamic as a function of temperature. The drift present on our force measurements should also be determined. Data from an aged swelling cell should be used with the developed SOC estimator, and the State of Health of the battery (SOH) should be estimated through the capacity fade to improve the performance of the developed estimator under battery cell degradation. The inflection point model mismatch on the F-SOC function will be studied in an aged cell since the inflection points change as the battery degrades or fades. In terms of aging, the expected variability in cell expansion is a subject of future studies. Cell-to-cell variability due to aging in the resulting force should also be investigated.

APPENDIX A

Supplemental Material

A.1 Detailed Computation for DP Implementation

For each of the five control actions in OCPs (5.24) and (5.28), the following equations are used to compute the corresponding acceleration, velocity, and force for a given distance of Δs :

Mode 1, Full Propulsion

$$\begin{aligned}\tilde{a} &= \min \left\{ \bar{a}, \frac{u_1^{\max} - \kappa(s, \xi_2)}{M} \right\}, \\ \xi_{2,k+1} &= \sqrt{\xi_{2,k}^2 + 2\tilde{a}\Delta s}, \\ f_e &= M\tilde{a} + \kappa(s, \xi_2), \\ f_f &= 0,\end{aligned}$$

Mode 2, Coasting

$$\begin{aligned}\tilde{a} &= \frac{-f_r - f_g}{M}, \\ \xi_{2,k+1} &= \sqrt{\xi_{2,k}^2 + 2\tilde{a}\Delta s}, \\ f_e &= 0, \\ f_f &= 0,\end{aligned}$$

Mode 3, Regenerative braking

$$\begin{aligned}\tilde{a} &= \max \left\{ \underline{a}, \frac{f_{\min} - f_r - f_g}{M} \right\}, \\ \xi_{2,k+1} &= \sqrt{\xi_{2,k}^2 + 2\tilde{a}\Delta s}, \\ f_e &= M\tilde{a} + f_r + f_g, \\ f_f &= 0,\end{aligned}$$

Mode 4, Full braking

$$\begin{aligned}\tilde{a} &= \underline{a}, \\ \xi_{2,k+1} &= \sqrt{\xi_{2,k}^2 + 2\tilde{a}\Delta s}, \\ f_e &= \max \{f_{\min}, M\tilde{a} + f_r + f_g\}, \\ f_f &= \min \{M\tilde{a} + f_r + f_g - f_e, 0\},\end{aligned}$$

Mode 5, Cruising

$$\begin{aligned}\tilde{a} &= 0, \\ \xi_{2,k+1} &= \xi_{2,k}, \\ f_e &= f_r + f_g, \\ f_f &= 0,\end{aligned}$$

In the equations above, the larger magnitude of the resisting force, f_r , or grade force, f_g , in addition to whether the grade is positive or negative, determines whether the force applied to the vehicle is a propulsion force or braking force. Thus, the force in cruising mode can be either positive or negative depending on the grade and its dominance over the other resisting forces.

A.2 Voltage Hysteresis State H Function

$$\begin{aligned}H(z, \text{sign}(I)) &= \text{sign}(I)(a_{12}z^{12} + a_{11}z^{11} + a_{10}z^{10} + a_9z^9 + a_8z^8 + a_7z^7 + a_6z^6 + a_5z^5 \\ &\quad + a_4z^4 + a_3z^3 + a_2z^2 + a_1z + a_0)\end{aligned}\tag{A.1}$$

where a_i with $i = 0-12$ are the tuned parameters and their values are found in Table A.1.

Table A.1: Voltage hysteresis state H function parameters and its values.

Parameters	Values	Parameters	Values	Parameters	Values
a_{12}	8662.54	a_8	319201.70	a_4	9255.46
a_{11}	-57,939.63	a_7	-234698.07	a_3	-1381.64
a_{10}	170,685.13	a_6	117809.10	a_2	127.23
a_9	-291398.86	a_5	-40316.61	a_1	-6.53
				a_0	0.16

A.3 Discrete Terminal Voltage Model

The discrete terminal voltage measurement equation is defined as

$$V_{T,t} = \tilde{V}_{oc}(z_t) - IR - V_{1,t} - V_{2,t} + v_{V,t} \quad (\text{A.2})$$

where $v_{V,t}$ is the V measurement noise. The piecewise linear (PWL) approximation of the OCV characteristic is modeled as

$$\tilde{V}_{oc}(z_t) = \begin{cases} \zeta z_t + \zeta_0 & \text{if } z_t \leq c_0 \\ \eta z_t + \eta_0 & \text{if } c_0 < z_t \leq c_1 \\ \theta z_t + \theta_0 & \text{if } c_1 < z_t \leq c_2 \\ \kappa z_t + \kappa_0 & \text{if } c_2 < z_t \leq c_3 \\ \sigma z_t + \sigma_0 & \text{if } c_3 < z_t \leq c_4 \\ \mu z_t + \mu_0 & \text{if } c_4 < z_t \leq c_5 \\ \varphi z_t + \varphi_0 & \text{if } c_5 < z_t \leq c_6 \\ \lambda z_t + \lambda_0 & \text{if } z_t \geq c_6 \end{cases} \quad (\text{A.3})$$

where $\zeta, \eta, \theta, \kappa, \sigma, \mu, \varphi,$ and λ are the slope parameters; ζ_0 is the minimum voltage sensed at fully discharged state; and $c_0, c_1, c_2, c_3, c_4, c_5,$ and c_6 are the piecewise point parameters. The parameters $\eta_0, \theta_0, \kappa_0, \sigma_0, \mu_0,$ and λ_0 are uniquely determined from the other parameters via constraints of piecewise continuity.

$$\eta_0 = (\zeta - \eta)c_0 + \zeta_0 \quad (\text{A.4})$$

$$\theta_0 = (\eta - \theta)c_1 + (\zeta - \eta)c_0 + \zeta_0 \quad (\text{A.5})$$

$$\kappa_0 = (\theta - \kappa)c_2 + (\eta - \theta)c_1 + (\zeta - \eta)c_0 + \zeta_0 \quad (\text{A.6})$$

$$\sigma_0 = (\kappa - \sigma)c_3 + (\theta - \kappa)c_2 + (\eta - \theta)c_1 + (\zeta - \eta)c_0 + \zeta_0 \quad (\text{A.7})$$

$$\mu_0 = (\sigma - \mu)c_4 + (\kappa - \sigma)c_3 + (\theta - \kappa)c_2 + (\eta - \theta)c_1 + (\zeta - \eta)c_0 + \zeta_0 \quad (\text{A.8})$$

$$\varphi_0 = (\mu - \varphi)c_5 + (\sigma - \mu)c_4 + (\kappa - \sigma)c_3 + (\theta - \kappa)c_2 + (\eta - \theta)c_1 + (\zeta - \eta)c_0 + \zeta_0 \quad (\text{A.9})$$

$$\lambda_0 = (\varphi - \lambda)c_6 + (\mu - \varphi)c_5 + (\sigma - \mu)c_4 + (\kappa - \sigma)c_3 + (\theta - \kappa)c_2 + (\eta - \theta)c_1 + (\zeta - \eta)c_0 + \zeta_0 \quad (\text{A.10})$$

The OCV characteristic and its PWL approximation are shown in Figure 6.3. Note that c_3 and c_5 also correspond to the inflection points in the PWL approximation of the force. The reason for this is that both functions of F–SOC and OCV–SOC have the same inflection points due to the electrochemical and mechanical model having the same phase transitions.

A.4 Force and OCV Function Values That Represent Average Data

Table A.2: Parameter values for the PWL OCV–SOC function in Equation (A.3) without model mismatch. Same values are used with model mismatch except for $c_3 = 0.34$ and $c_5 = 0.69$.

Parameters	Values	Parameters	Values	Parameters	Values
ζ	9.232	μ	0.02836	c_3	0.35
ζ_0	2.622	φ	2.264	c_4	0.6511
η	0.3899	λ	0.03506	c_5	0.7
θ	0.4922	c_0	0.06	c_6	0.9767
κ	0.2724	c_1	0.1516		
σ	0.5515	c_2	0.2528		

Table A.3: Parameter values for the OCV–SOC function in Equation (6.7).

Parameters	Values	Parameters	Values	Parameters	Values
V_0	-2.4354	$a_{v,1}$	0.0206	$a_{v,3}$	0.0166
d	0.1162	$b_{v,1}$	0.2321	$b_{v,3}$	0.6799
f	5.7469	$c_{v,1}$	0.0626	$c_{v,3}$	0.0306
h	1.2942	$a_{v,2}$	5.6185		
k	3.0014×10^{-4}	$b_{v,2}$	-0.0513		
g	-0.0098	$c_{v,2}$	0.0406		

Table A.4: Parameter values for the F–SOC function that represent average data. This model is also used for PWL F–SOC without model mismatch (b_L and b_H) and with model mismatch (\hat{b}_L and \hat{b}_H).

Parameters	Values	Parameters	Values	Parameters	Values
α_m	63.11	γ_m	21.78	\hat{b}_L	0.34
α_{m0}	1641	b_L	0.35	\hat{b}_H	0.69
β_m	-29.53	b_H	0.7		

BIBLIOGRAPHY

- [1] Aeristech electric fuel cell compressor data sheet.
- [2] Ballard fcgen-1020acs product data sheet.
- [3] Gt-suite overview. <https://www.gtisoft.com/gt-suite/gt-suite-overview/>.
- [4] Hymn hd 15 Installation and operation manual.
- [5] Poron 4701-30 polyurethane. <https://rogerscorp.com/elastomeric-material-solutions/poron-industrial-polyurethanes/poron-4701-30>.
- [6] Usabc electric vehicle battery test procedures manual, appendix j-detailed procedure. https://www.uscar.org/guest/article_view.php?articles_id=74.
- [7] Mark1020 acs fuel cell stack product manual and integration guide. Technical report, Ballard, 2009.
- [8] *Electric Vehicles Modelling and Simulations*. InTech, 2011.
- [9] Technology assessment of a fuel cell vehicle: 2017 toyota mirai. Technical report, Argonne National Laboratory, 2018.
- [10] Hadi Abbas, Youngki Kim, Jason B. Siegel, and Denise M. Rizzo. Synthesis of pontryagin’s maximum principle analysis for speed profile optimization of electrified vehicles. *Journal of Dynamic Systems, Measurement and Control*, 141(7):071004–071004–10, 2019.
- [11] Frano Barbir. *PEM fuel cells theory and practice*. Elsevier/Academic Press, 2013.
- [12] Félix Barreras, Ana M. López, Antonio Lozano, and José E. Barranco. Experimental study of the pressure drop in the cathode side of air-forced open-cathode proton exchange membrane fuel cells. *International Journal of Hydrogen Energy*, 36:7612–7620, 2011.
- [13] Ameen M. Bassam, Alexander B. Phillips, Stephen R. Turnock, and Philip A. Wilson. An improved energy management strategy for a hybrid fuel cell/battery passenger vessel. *International Journal of Hydrogen Energy*, 41(47):22453–22464, 2016.
- [14] B. Bendjedia, N. Rizoug, M. Boukhniifer, and F. Bouchafaa. Hybrid fuel cell/battery source sizing and energy management for automotive applications. *IFAC-PapersOnLine*, 50(1):4745–4750, 2017.

- [15] Kevin Boice et al. Baseline field testing of bb-2590 lithium-ion batteries using an irobot fastac 510 robot. Technical report, TARDEC, 2010.
- [16] Tatenda J. Bvumbe, Piotr Bujlo, Ivan Tolj, Kobus Mouton, Gerhard Swart, Sivakumar Pasupathi, and Bruno G. Pollet. Review on management, mechanisms and modelling of thermal processes in pemfc. *Hydrogen and Fuel Cells*, 1:1–20, 2016.
- [17] S. Di Cairano, W. Liang, I. V. Kolmanovsky, M. L. Kuang, and A. M. Phillips. Power smoothing energy management and its application to a series hybrid powertrain. *IEEE Transactions on Control Systems Technology*, 21(6):2091–2103, Nov 2013.
- [18] John Cannarella, Collen Z. Leng, and Craig B. Arnold. On the coupling between stress and voltage in lithium-ion pouch cells. In *In Proceedings of SPIE Sensing Technology + Applications Energy Harvesting and Storage: Materials, Devices, and Applications*, 2014.
- [19] Zachary P. Cano, Dustin Banham, Siyu Ye, Andreas Hintennach, Jun Lu, Michael Fowler, and Zhongwei Chen. Batteries and fuel cells for emerging electric vehicle markets. *Nature Energy*, 3:279–289, 2018.
- [20] Edoardo Catenaro, Denise M. Rizzo, and Simona Onori. Experimental analysis and analytical modeling of enhanced-ragone plot. *Applied Energy*, 291:116473, 2021.
- [21] Andrew Chapman et al. A review of four case studies assessing the potential for hydrogen penetration of the future energy system. *International Journal of Hydrogen Energy*, 44:6371–6382, 2019.
- [22] Denver Cheddie and Norman Munroe. Review and comparison of approaches to proton exchange membrane fuel cell modeling. *Journal of Power Sources*, 147:72–84, 2005.
- [23] Boli Chen, Simos A. Evangelou, and Roberto Lot. Series hybrid electric vehicle simultaneous energy management and driving speed optimization. *IEEE/ASME Transactions on Mechatronics*, pages 1–11, 2019.
- [24] Di Chen, Youngki Kim, and Anna G. Stefanopoulou. Predictive equivalent consumption minimization strategy with segmented traffic information. *IEEE Transactions on Vehicular Technology*, 69(12):14377–14390, 2020.
- [25] Di Chen, Niket Prakash, Anna G. Stefanopoulou, Mike Huang, Youngki Kim, and Scott R. Hotz. Sequential optimization of velocity and charge depletion in a plug-in hybrid electric vehicle. In *14th International Symposium on Advanced Vehicle Control*, July 2018.
- [26] Y. Chen, X. Li, C. Wiet, and J. Wang. Energy management and driving strategy for in-wheel motor electric ground vehicles with terrain profile preview. *IEEE Transactions on Industrial Informatics*, 10(3):1938–1947, 2014.
- [27] Zheng Chen, Yuhong Fu, and Chunting Chris Mi. State of charge estimation of lithium-ion batteries in electric drive vehicles using extended kalman filtering. *IEEE Transactions on Vehicular Technology*, 62(3):1020–1030, 2013.

- [28] K. W. E. Cheng, B. P. Divakar, Hongjie Wu, Kai Ding, and Ho Fai Ho. Battery-management system (bms) and soc development for electrical vehicles. *IEEE Transactions on Vehicular Technology*, 60(1):76–88, 2011.
- [29] Hydrogen Council. Hydrogen Scaling Up. Technical report, Hydrogen Council, 2017.
- [30] Kevin Davis and John G. Hayes. Fuel cell vehicle energy management strategy based on the cost of ownership. *IET Electrical Systems in Transportation*, 9(4):226–236, 2019.
- [31] Mohamed Derbeli, Maissa Farhat, Oscar Barambones, and Lassaad Sbita. Control of proton exchange membrane fuel cell (pemfc) power system using pi controller. In *2017 International Conference on Green Energy Conversion Systems (GECS)*, 2017.
- [32] Mohamed Derbeli, Maissa Farhat, Oscar Barambones, and Lassaad Sbita. Control of proton exchange membrane fuel cell (pemfc) power system using pi controller. In *2017 International Conference on Green Energy Conversion Systems (GECS)*, 2017.
- [33] Domenico Di Domenico, Giovanni Fiengo, and Anna Stefanopoulou. A decoupled controller for fuel cell hybrid electric power split. *International Journal of Systems Science*, 41(4):447–456, 2010.
- [34] Domenico Di Domenico, Anna Stefanopoulou, and Giovanni Fiengo. Lithium-ion battery state of charge and critical surface charge estimation using an electrochemical model-based extended kalman filter. *Journal of Dynamic Systems, Measurement, and Control*, 132(6):061302, 2010.
- [35] Dima Fares, Riad Chedid, Ferdinand Panik, Sami Karaki, and Rabih Jabr. Dynamic programming technique for optimizing fuel cell hybrid vehicles. *International Journal of Hydrogen Energy*, 40:7777–7790, 2015.
- [36] Huckleberry Febbo. *Real-time Trajectory Planning to Enable Safe and Performant Automated Vehicles Operating in Unknown Dynamic Environments*. PhD thesis, The University of Michigan, 2019.
- [37] Miriam A. Figueroa-Santos, Jason B. Siegel, and Anna G. Stefanopoulou. Leveraging cell expansion sensing in state of charge estimation: Practical considerations. *Energies*, 13(10):2653, 2020.
- [38] Miriam A. Figueroa-Santos and Anna G. Stefanopoulou. *Fuel Cell Vehicle Optimization and Control*, pages 1–9. Springer London, London, 2020.
- [39] S. Fish and T.B. Savoie. Simulation-based optimal sizing of hybrid electric vehicle components for specific combat missions. *IEEE Transactions on Magnetics*, 37(1):485–488, 2001.
- [40] Tom Fletcher, Rob Thring, and Martin Watkinson. An energy management strategy to concurrently optimise fuel consumption & pem fuel cell lifetime in a hybrid vehicle. *International Journal of Hydrogen Energy*, 41:21503–21515, 2016.

- [41] Joel C. Forman, Scott J. Moura, Jeffrey L. Stein, and Hosam K. Fathy. Genetic parameter identification of the doyle-fuller- newman model from experimental cycling of a lifepo4 battery. In *2011 American Control Conference*, 2011.
- [42] Huizhong Gao, Zhijie Wang, Shaoping Yin, Jun Lu, Zhaoyuan Guo, and Weifeng Ma. Adaptive real-time optimal energy management strategy based on equivalent factors optimization for hybrid fuel cell system. *International Journal of Hydrogen Energy*, 46(5):4329–4338, 2021.
- [43] Phanikrishna Gomatam and Ward Jewell. Fuel parameter and quality constraints for fuel cell distributed generators. In *Proceedings of the 2003 IEEE Transmission and Distribution Conference*, 2003.
- [44] Alireza Goshtasbi and Tulga Ersal. Degradation-conscious control for enhanced lifetime of automotive polymer electrolyte membrane fuel cells. *Journal of Power Sources*, 457:227996, 2020.
- [45] C. Guardiola, B. Pla, S. Onori, and G. Rizzoni. A new approach to optimally tune the control strategy for hybrid vehicles applications*. *IFAC Proceedings Volumes*, 45(30):255 – 261, 2012.
- [46] Tianyou Guo. *Power Consumption Models for Tracked and Wheeled Small Unmanned Ground Vehicles on Deformable Terrains*. PhD thesis, UM, 2016.
- [47] Jaeyoung Han, Sangseok Yu, and Sun Yi. Oxygen excess ratio control for proton exchange membrane fuel cell using model reference adaptive control. *International Journal of Hydrogen Energy*, 44(33):18425–18437, 2019.
- [48] Jihun Han, Ardalan Vahidi, and Antonio Sciarretta. Fundamentals of energy efficient driving for combustion engine and electric vehicles: An optimal control perspective. *Automatica*, 103:558 – 572, 2019.
- [49] Mahammad A. Hannan, Farid Arafat Bin Azidin, and Azah Mohamed. Hybrid electric vehicles and their challenges: a review. *Renewable and Sustainable Energy Reviews*, 29:135–150, 2014.
- [50] Liang Hao, Koji Moriyama, Wenbin Gu, and Chao-Yang Wang. Three dimensional computations and experimental comparisons for a large-scale proton exchange membrane fuel cell. *Journal of The Electrochemical Society*, 163(7):F744–751, 2016.
- [51] Hongwen He, Shengwei Quan, Fengchun Sun, and Ya-Xiong Wang. Model predictive control with lifetime constraints based energy management strategy for proton exchange membrane fuel cell hybrid power systems. *IEEE Transactions on Industrial Electronics*, 67(10):9012–9023, 2020.
- [52] Gunter Heppeler, Marcus Sonntag, and Oliver Sawodny. Fuel efficiency analysis for simultaneous optimization of the velocity trajectory and the energy management in hybrid electric vehicles. *IFAC Proceedings Volumes*, 47(3):6612 – 6617, 2014.

- [53] Gunter Heppeler, Marcus Sonntag, Uli Wohlhaupter, and Oliver Sawodny. Predictive planning of optimal velocity and state of charge trajectories for hybrid electric vehicles. *Control Engineering Practice*, 61:229–243, 2017.
- [54] Zhihu Hong, Qi Li, Ying Han, Weilin Shang, Yanan Zhu, and Weirong Chen. An energy management strategy based on dynamic power factor for fuel cell/battery hybrid locomotive. *International Journal of Hydrogen Energy*, 43(6):3261–3272, 2018.
- [55] Roy Chaoming Hsu, Shi-Mao Chen, Wen-Yen Chen, and Cheng-Ting Liu. A reinforcement learning based dynamic power management for fuel cell hybrid electric vehicle. In *2016 Joint 8th International Conference on Soft Computing and Intelligent Systems and 2016 17th International Symposium on Advanced Intelligent Systems*, 2016.
- [56] Liang Hu, Jing Dong, Zhenhong Lin, and Jie Yang. Analyzing battery electric vehicle feasibility from taxi travel patterns: The case study of new york city, usa. *Transportation Research Part C: Emerging Technologies*, 87:91–104, 2018.
- [57] Xiaosong Hu, Shengbo Li, and Huei Peng. A comparative study of equivalent circuit models for li-ion batteries. *Journal of Power Sources*, 198:359–367, 2012.
- [58] Xiaosong Hu, Changfu Zou, Xiaolin Tang, Teng Liu, and Lin Hu. Cost-optimal energy management of hybrid electric vehicles using fuel cell/battery health-aware predictive control. *IEEE Transactions on PowerElectronics*, 35(1):382–392, 2020.
- [59] Wangxin Huang and Jaber A. Abu Qahouq. Energy sharing control scheme for state-of-charge balancing of distributed battery energy storage system. *IEEE Transactions on Industrial Electronics*, 62(5):2764–2776, 2015.
- [60] Brian D. James. 2020 DOE Hydrogen and Fuel Cells Program Review Presentation Fuel Cell Systems Analysis. 2020.
- [61] Brian D James et al. Mass Production Cost Estimation of Direct H2 PEM Fuel Cell Systems for Transportation Applications: 2018 Update. Technical report, Strategic Analysis Inc., 2018.
- [62] Brian D. James, Cassidy Houchins, Jennie M. Huya-Kouadio, and Daniel A. DeSantis. Final report: Hydrogen storage system cost analysis. Technical report, Strategic Analysis Inc., 2016.
- [63] E.M.C. Jones, M.N. Silberstein, S.R. White, and N.R. Sottos. In situ measurements of strains in composite battery electrodes during electrochemical cycling. *Experimental Mechanics*, 54:971–985, 2014.
- [64] M. Kandidayenia, A. Maciasa, L. Boulona, and S. Kelouwanic. Investigating the impact of ageing and thermal management of a fuel cell system on energy management strategies. *Applied Energy*, 274:115293, 2020.
- [65] H. J. Kelley. A second variation test for singular extremals. *AIAA Journal*, 2:1380–1382, August 1964.

- [66] Namwook Kim, Seungbum Ha, Jongryeol Jeong, and Suk Won Cha. Sufficient conditions for optimal energy management strategies of fuel cell hybrid electric vehicles based on pontryagin's minimum principle. *Proceedings of the Institution of Mechanical Engineers, Part D: Journal of Automobile Engineering*, 230(2):202–214, 2015.
- [67] Taesic Kim, Wei Qiao, and Liyan Qu. A series-connected self-reconfigurable multicell battery capable of safe and effective charging/discharging and balancing operations. In *2012 Twenty-Seventh Annual IEEE Applied Power Electronics Conference and Exposition (APEC)*, 2012.
- [68] Youngki Kim, Miriam Figueroa-Santos, Niket Prakash, Stanley Baek, Jason B. Siegel, and Denise M. Rizzo. Co-optimization of speed trajectory and power management for a fuel-cell/battery electric vehicle. *International Journal of Precision Engineering and Manufacturing*, 260:1–17, 2020.
- [69] Youngki Kim, Nassim A. Samad, Ki-Yong Oh, Jason B. Siegel, Bogdan I. Epureanu, and Anna G. Stefanopoulou. Estimating state-of-charge imbalance of batteries using force measurements. In *2016 American Control Conference (ACC)*, 2016.
- [70] Matjaz Knez, Gašper Kozelj Zevnik, and Matevz Obrecht. A review of available chargers for electric vehicles: United states of america, european union, and asia. *Renewable and Sustainable Energy Reviews*, 109:284–293, 2019.
- [71] Aaron Knobloch, Chris Kapusta, Jason Karp, Yuri Plotnikov, Jason B. Siegel, and Anna G. Stefanopoulou. Fabrication of multimeasurand sensor for monitoring of a li-ion battery. *Journal of Electronic Packaging*, 140(3):031002, 2018.
- [72] Andrei A. Kulikovskiy. *Analytical modelling of fuel cells*. Elsevier, 2010.
- [73] Trevor Hocksun Kwan, Yongting Shen, and Qinghe Yao. An energy management strategy for supplying combined heat and power by the fuel cell thermoelectric hybrid system. *Applied Energy*, 251:113318, 2019.
- [74] Ainhoa De las Heras, Francisco José Vivas, Fracisca Segura, Manuel Joaquín Redondo, and Jose Manuel Andujar. Air-cooled fuel cells: Keys to design and build the oxidant/cooling system. *Renewable Energy*, 125:1 – 20, 2018.
- [75] Suhak Lee, Peyman Mohtat, Jason B. Siegel, and Anna G. Stefanopoulou. Beyond estimating battery state of health: Identifiability of individual electrode capacity and utilization. In *2018 Annual American Control Conference (ACC)*, 2018.
- [76] Jonathan R. LeSage and Raul G. Longoria. Characterization of load uncertainty in unstructured terrains and applications to battery remaining run-time prediction. *J. Field Robot.*, 30(3):472–487, 2013.
- [77] Frank L. Lewis. *Optimal Estimation: With an Introduction to Stochastic Control Theory*. Wiley, 1986.

- [78] Huan Li, Alexandre Ravey, Abdoul N'Diaye, and Abdesslem Djerdir. Online adaptive equivalent consumption minimization strategy for fuel cell hybrid electric vehicle considering power sources degradation. *Energy Conversion and Management*, 192:133–149, 2019.
- [79] Chan-Chiao Lin, Min-Joong Kim, Huei Peng, and Jessy W. Grizzle. System-level model and stochastic optimal control for a pem fuel cell hybrid vehicle. *Journal of Dynamic Systems, Measurement, and Control*, 1284(4):878–890, 2006.
- [80] Changhong Liu and Lin Liu. Optimal power source sizing of fuel cell hybrid vehicles based on pontryagin's minimum principle. *International Journal of Hydrogen Energy*, 40:8454–8464, 2015.
- [81] Shiqi Liu, Yang Bin, Yaoyu Li, and Birgit Scheppat. Hierarchical mpc control scheme for fuel cell hybrid electric vehicles. *IFAC-PapersOnLine*, 51(31):646–652, 2018.
- [82] Xuan Liu, Kang Li, and Xiang Li. The electrochemical performance and applications of several popular lithium-ion batteries for electric vehicles - a review. In Kang Li, Jianhua Zhang, Minyou Chen, Zhile Yang, and Qun Niu, editors, *Advances in Green Energy Systems and Smart Grid*, pages 201–213, Singapore, 2018. Springer Singapore.
- [83] Yonggang Liu, Junjun Liu, Datong Qin, Guang Li, Zheng Chen, and Yi Zhang. Online energy management strategy of fuel cell hybrid electric vehicles based on rule learning. *Journal of Cleaner Production*, 260:121017, 2020.
- [84] Xueqin Lü, Yinbo Wu, Jie Lian, Yangyang Zhang, Chao Chen, Peisong Wang, and Lingzheng Meng. Energy management of hybrid electric vehicles: A review of energy optimization of fuel cell hybrid power system based on genetic algorithm. *Energy Conversion and Management*, 205:112474, 2020.
- [85] D. Maamria, K. Gillet, G. Colin, Y. Chamailard, and C. Nouillant. Computation of eco-driving cycles for hybrid electric vehicles: Comparative analysis. *Control Engineering Practice*, 71:44 – 52, 2018.
- [86] J. Macedo-Valencia, J.M. Sierra, S.J. Figueroa-Ramírez, S.E. Díaz, and M. Meza. 3d cfd modeling of a pem fuel cell stack. *International Journal of Hydrogen Energy*, 41(48):23425–23433, 2016.
- [87] Chaima Mahjoubi, Jean Christophe Olivier, Sondes Skander-Mustapha, Ilhem Slama-Belkhodja, and Mohamed MaChmoum. An improved open cathode proton exchange membrane fuel cell control ensuring a simultaneous regulation of temperature and air flow. In *2018 9th International Renewable Energy Congress (IREC)*, 2018.
- [88] Chaima Mahjoubi, Jean Christophe Olivier, Sondes Skander-Mustapha, Ilhem Slama-Belkhodja, and Mohamed MaChmoum. An improved open cathode proton exchange membrane fuel cell control ensuring a simultaneous regulation of temperature and air flow. In *2018 9th International Renewable Energy Congress (IREC)*, 2018.
- [89] T. Maiyalagan and Sivakumar Pasupathi. Components for pem fuel cells: An overview. *Materials Science Forum*, 657:143–189, 2010.

- [90] Rahul Malik, Aziz Abdellahi, and Gerbrand Ceder. A critical review of the li insertion mechanisms in lifepo4 electrodes. *The Electrochemical Society*, 160(5):A3179, 2013.
- [91] Neigel Marz, Daniel Hissel, Frédéric Gustin, Loïc Boulon, and Kodjo Agbossou. On the sizing and energy management of an hybrid multistack fuel cell-battery system for automotive applications. *International Journal of Hydrogen Energy*, 42:1518–15126, 2017.
- [92] A. Masrur, R. Smith, and A. Nedungadi. Quantitative analysis of a hybrid electric hmmwv for fuel economy improvement. 2012.
- [93] Buz A. McCain, Anna G. Stefanopoulou, and Ilya V. Kolmanovsky. A dynamic semi-analytic channel-to-channel model of two-phase water distribution for a unit fuel cell. *IEEE Transactions on Control Systems Technology*, 17(5):1055–1068, 2009.
- [94] Hua Meng. Multi-dimensional liquid water transport in the cathode of a pem fuel cell with consideration of the micro-porous layer (mpl). *International Journal of Hydrogen Energy*, 34(13):5488–5497, 2009.
- [95] F. Mensing, R. Trigui, and E. Bideaux. Vehicle trajectory optimization for application in eco-driving. In *2011 IEEE Vehicle Power and Propulsion Conference*, pages 1–6, Sept 2011.
- [96] Felicitas Mensing, Eric Bideaux, Rochdi Trigui, Julien Ribet, and Bruno Jeanneret. Eco-driving: An economic or ecologic driving style? *Transportation Research Part C: Emerging Technologies*, 38:110 – 121, 2014.
- [97] Felicitas Mensing, Eric Bideaux, Rochdi Trigui, and Helene Tattegrain. Trajectory optimization for eco-driving taking into account traffic constraints. *Transportation Research Part D: Transport and Environment*, 18:55 – 61, 2013.
- [98] Shankar Mohan, Youngki Kim, Jason B. Siegel, Nassim A. Samad, and Anna G. Stefanopoulou. A phenomenological model of bulk force in a li-ion battery pack and its application to state of charge estimation. *Journal of the Electrochemical Society*, 161(4):A2222–A2231, 2014.
- [99] Shankar Mohan, Youngki Kim, and Anna G. Stefanopoulou. On improving battery state of charge estimation using bulk force measurements. In *In Proceedings of the ASME 2015 Dynamic Systems and Control Conference*, October 2015.
- [100] Peyman Mohtat, Suhak Lee, Jason B. Siegel, and Anna G. Stefanopoulou. Towards better estimability of electrode-specific state of health: Decoding the cell expansion. *Journal of Power Sources*, 427:101–111, 2019.
- [101] Geoff Morrison, John Stevens, and Fred Joseck. Relative economic competitiveness of light-duty battery electric and fuel cell electric vehicles. *Transportation Research Part C: Emerging Technologies*, 87:183–196, 2018.

- [102] Dominik Murschenhofer, Dominik Kuzdas, Stefan Braun, and Stefan Jakubek. A real-time capable quasi-2d proton exchange membrane fuel cell model. *Energy Conversion and Management*, 162:159–175, 2018.
- [103] Fredy Nandjou, Jean-Philippe Poirot-Crouvezier, Marion Chandesris, Jean Francois Blachot, Céline Bonnaud, and Yann Bultel. Impact of heat and water management on proton exchange membrane fuel cells degradation in automotive application. *Journal of Power Sources*, 326:182–192, 2016.
- [104] Paul A. Nelson, Kevin G. Gallagher, Shabbir Ahmed, Dennis W. Dees, Naresh Susarla, Ira D. Bloom, Joseph J. Kubal, Juhyun Song, and Zhe Liu. Batpac model software.
- [105] D. V. Ngo, T. Hofman, M. Steinbuch, and A. F. A. Serrarens. An optimal control-based algorithm for hybrid electric vehicle using preview route information. In *Proceedings of the 2010 American Control Conference*, pages 5818–5823, 2010.
- [106] Alexandros Nikolian, Joris Jaguemont, Joris de Hoog, Shovon Goutam, Noshin Omar, Peter Van Den Bossche, and Joeri Van Mierlo. Complete cell-level lithium-ion electrical ecm model for different chemistries (nmc, lfp, lto) and temperatures (-5c to 45c) - optimized modelling techniques. *International Journal of Electrical Power & Energy Systems*, 98:133–146, 2018.
- [107] U.S. Department of Transportation National Highway Traffic Safety Administration. Integrated vehicle-based safety systems field operational test final program report. Technical report, U.S. Department of Transportation National Highway Traffic Safety Administration, 2011.
- [108] Ki-Yong Oh, Jason B.Siegel, Lynn Secondo, Sun Ung Kim, Nassim A.Samad, Jiawei Qin, Dyche Anderson, Krishna Garikipati, Aaron Knobloch, Bogdan I.Epureanu, Charles, W.Monroe, and Anna Stefanopoulou. Rate dependence of swelling in lithium-ion cells. *Journal of Power Sources*, 267(1):197–202, 2014.
- [109] Ryan O’Hayre, Suk-Won Cha, Whitney Colella, and Fritz B. Prinz. *Fuel cell fundamentals*. John Wiley & Sons, 2016.
- [110] Simona Onori, Lorenzo Serrao, and Giorgio Rizzoni. *Hybrid Electric Vehicles Energy Management Strategies*. Springer, 2016.
- [111] G. P. Padilla, S. Weiland, and M. C. F. Donkers. A global optimal solution to the eco-driving problem. *IEEE Control Systems Letters*, 2(4):599–604, 2018.
- [112] Gino Paganelli, Thierry Marie Guerra, Sebastien Delprat, Yann G. Guezennec, and Giorgio Rizzoni. Optimal control theory applied to hybrid fuel cell powered vehicle. *IFAC Proceedings Volumes*, 35(1):253–258, 2002.
- [113] Michael A. Patterson and Anil V. Rao. Gpops-ii: A matlab software for solving multiple-phase optimal control problems using hp-adaptive gaussian quadrature collocation methods and sparse nonlinear programming. *ACM Transactions on Mathematical Software (TOMS)*, 41(1):1–37, 2014.

- [114] Christina Peabody and Craig B. Arnold. The role of mechanically induced separator creep in lithium-ion battery capacity fade. *Journal of Power Sources*, 196(19):8147–8153, 2011.
- [115] Fei Peng, Yuanzhe Zhao, Ting Chen, Xuexia Zhang, Weirong Chen, Donghua Zhou, and Qi Li. Development of robust suboptimal real-time power sharing strategy for modern fuel cell based hybrid tramways considering operational uncertainties and performance degradation. *Applied Energy*, 226:503 – 521, 2018.
- [116] Hector E. Perez, Jason B. Siegel, Xinfan Lin, Anna G. Stefanopoulou, Yi Ding, and Matthew P. Castanier. Parameterization and validation of an integrated electro-thermal cylindrical lfp battery model. In *ASME 2012 5th Annual Dynamic Systems and Control Conference Joint with the JSME 2012 11th Motion and Vibration Conference*, 2012.
- [117] Derek Pletcher. *Electrochemistry: Volume 8*. Royal Society of Chemistry, 2007.
- [118] Gregory L. Plett. *Battery Management Systems, Volume I: Battery Modeling*. Artech House, 2015.
- [119] Tomáš Polóni, Miriam Aileen Figueroa-Santos, Jason B. Siegel, and Anna G. Stefanopoulou. Integration of non-monotonic cell swelling characteristic for state-of-charge estimation. In *2018 Annual American Control Conference (ACC)*, 2018.
- [120] Jay T Pukrushpan, Huei Peng, and Anna G Stefanopoulou. Simulation and analysis of transient fuel cell system performance based on a dynamic reactant flow model. In *Proceedings of IMECE2002 ASME International Mechanical Engineering Congress & Exposition*, 2002.
- [121] Jay T. Pukrushpan, Huei Peng, and Anna G. Stefanopoulou. Control-oriented modeling and analysis for automotive fuel cell systems. *J. Dyn. Sys., Meas., Control.*, 126(1):14–25, 2004.
- [122] Jay T. Pukrushpan, Anna G. Stefanopoulou, and Huei Peng. *Control of fuel cell power systems: principles, modeling, analysis and feedback design*. Springer, 2005.
- [123] X. Qi, G. Wu, P. Hao, K. Boriboonsomsin, and M. J. Barth. Integrated-connected eco-driving system for phev with co-optimization of vehicle dynamics and powertrain operations. *IEEE Transactions on Intelligent Vehicles*, 2(1):2–13, 2017.
- [124] Shaolin Qiu, Lihong Qiu, Lijun Qian, and Pierluigi Pisu. Hierarchical energy management control strategies for connected hybrid electric vehicles considering efficiencies feedback. *Simulation Modelling Practice and Theory*, 90:1 – 15, 2019.
- [125] Habiballah Rahimi-Eichi, Unnati Ojha, Federico Baronti, and Mo-Yuen Chow. Battery management system: An overview of its application in the smart grid and electric vehicles. *IEEE Industrial Electronics Magazine*, 7(2):4–16, 2013.
- [126] Wan Ramli, Wan Daud, Ros Emilia Rosli, Edy Herianto Majlan, Siti Afiqah Abd Hamid, Ramizi Mohamed, and Husaini Teuku. Pem fuel cell system control: A review. *Renewable Energy*, 113:620–638, 2017.

- [127] Namireddy Praveen Reddy, David Padeloup, Mehdi Karbalaye Zadeh, and Roger Skjetne. An intelligent power and energy management system for fuel cell/battery hybrid electric vehicle using reinforcement learning. In *2019 IEEE Transportation Electrification Conference and Expo (ITEC)*, pages 1–6, 2019.
- [128] Etienne Rivard, Michel Trudeau, and Karim Zaghbi. Hydrogen storage for mobility: A review. *Materials*, 12(12):1–22, 2019.
- [129] Usman Salahuddin et al. Grid to wheel energy efficiency analysis of battery- and fuel-cell-powered vehicles. *International Journal of Energy Research*, 42(5):2021–2028, 2018.
- [130] Nassim A. Samad, Youngki Kim, Jason B. Siegel, and Anna G. Stefanopoulou. Battery capacity fading estimation using a force-based incremental capacity analysis. *Journal of The Electrochemical Society*, 163(8):A1584–A1594, 2016.
- [131] T. V. S. L. Satyavani, A. Srinivas Kumara, and P. S. V. Subba Rao. Methods of synthesis and performance improvement of lithium iron phosphate for high rate li-ion batteries: A review. *Engineering Science and Technology, an International Journal*, 19(1):178–188, 2016.
- [132] Katherine Sebeck, Jeremy Mange, Jamie MacLennan, and Denise Rizzo. Characterization of army ground vehicle drive cycles. In *NDIA Ground Vehicle Systems Engineering and Technology Symposium*, 2017.
- [133] Dale E. Seborg, Duncan A. Mellichamp, Thomas F. Edgar, and Francis J. Doyle III. *Process Dynamics and Control*. Wiley, 2011.
- [134] Mahmoud Shousha, Timothy McRae, Aleksandar Prodić, Victor Marten, and John Milios. Design and implementation of high power density assisting step-up converter with integrated battery balancing feature. *IEEE Journal of Emerging and Selected Topics in Power Electronics*, 5(3):1068–1077, 2017.
- [135] Jason Siegel. *Experiments and Modeling of PEM Fuel Cells for Dead-Ended Anode Operation*. Theses, University of Michigan, October 2010.
- [136] Jason B. Siegel, Anna G. Stefanopoulou, Denise Rizzo, and Niket Prakash. Cooling parasitic considerations for optimal sizing and powersplit strategy for military robot powered by hydrogen fuel cells. *SAE Technical Paper*, 2018.
- [137] Jacob Spendelow and Jason Marcinkoski. Fuel cell system cost - 2013. Technical report, DOE Fuel Cell Technologies Office, 2014.
- [138] T. E. Springer, T. Zawodzinski, and S. Gottesfeld. Polymer electrolyte fuel cell model. *Journal of The Electrochemical Society*, 138(8):2334–2342, 1991.
- [139] Kyung-Won Suh and Anna G. Stefanopoulou. Coordination of converter and fuel cell controllers. *International Journal of Energy Research*, 29:1167–1189, 2005.
- [140] N. Sulaiman, M. A. Hannah, A. Mohamed, P. J. Ker, E. H. Majlan, and W. R. Wan Daud. Optimization of energy management system for fuel-cell hybrid electric vehicles: Issues and recommendations. *Applied Energy*, 228:2061–2079, 2018.

- [141] Li Sun, Guanru Li, Qingsong Hua, and Yuhui Jin. A hybrid paradigm combining model-based and data-driven methods for fuel cell stack cooling control. *Renewable Energy*, 1471(1):1642–1652, 2020.
- [142] O. Sundstrom and L. Guzzella. A generic dynamic programming matlab function. In *2009 IEEE Control Applications, (CCA) Intelligent Control, (ISIC)*, pages 1625–1630, July 2009.
- [143] Olle Sundström and Anna Stefanopoulou. Optimum battery size for fuel cell hybrid electric vehicle-part i. *J. Electrochem. En. Conv. Stor*, 4(2):167–175, 2006.
- [144] Olle Sundström and Anna Stefanopoulou. Optimum battery size for fuel cell hybrid electric vehicle with transient loading consideration-part ii. *J. Electrochem. En. Conv. Stor*, 4(2):176–184, 2006.
- [145] Bahattin Tanc et al. Overview of the next quarter century vision of hydrogen fuel cell electric vehicles. *International Journal of Hydrogen Energy*, 44(20):10120–10128, 2019.
- [146] C. E. Thomas. Fuel cell and battery electric vehicles compared. *International Journal of Hydrogen Energy*, 34(15):6005–6020, 2009.
- [147] Toyota. 2021 toyota mirai brochure.
- [148] P. J. Tritschler, S. Bacha, E. Rullière, and G. Husson. Energy management strategies for an embedded fuel cell system on agricultural vehicle. In *The XIX International Conference on Electrical Machines - ICEM 2010*, 2010.
- [149] Rong-Jong Wai, Shih-Jie Jhung, Jun-Jie Liaw, and Yung-Ruei Chang. Intelligent optimal energy management system for hybrid power sources including fuel cell and battery. *IEEE Transactions on Power Electronics*, 28(7):3231–3244, 2013.
- [150] Rong-Jong Wai, Shih-Jie Jhung, Jun-Jie Liaw, and Yung-Ruei Chang. Intelligent optimal energy management system for hybrid power sources including fuel cell and battery. *IEEE Transactions on Power Electronics*, 28(7):3231–3244, 2013.
- [151] Bowen Wang, Kangcheng Wu, Zirong Yang, and Kui Jiao. A quasi-2d transient model of proton exchange membrane fuel cell with anode recirculation. *Energy Conversion and Management*, 171:1463–1475, 2018.
- [152] Jun-chang Wang, Wang Bin, Yi-fan Dai, and Zong-qi Han. Research on the strategy of gliding in eco-driving. *DEStech Transactions on Environment, Energy and Earth Science*, 04 2017.
- [153] Tianwei (Thomas) Wang, Amit Jagarwal, John R. Wagner, and Georges Fadel. Optimization of an automotive radiator fan array operation to reduce power consumption. *IEEE/ASME Transactions on Mechatronics*, 20(5):2359–2369, 2014.
- [154] Ya-Xiong Wang, Kai Ou, and Young-Bae Kim. Modeling and experimental validation of hybrid proton exchange membrane fuel cell/battery system for power management control. *International Journal of Hydrogen Energy*, 40:11713–11721, 2015.

- [155] Yongqiang Wang, Scott J. Mour, Suresh G. Advani, and Ajay K. Prasad. Optimization of powerplant component size on board a fuel cell/battery hybrid bus for fuel economy and system durability. *International Journal of Hydrogen Energy*, 44:18283–18292, 2019.
- [156] Yuanzhan Wang, Jason B. Siegel, and Anna G. Stefanopoulou. Control strategies for power quantized solid oxide fuel cell hybrid powertrains: In mobile robot applications. *SAE International Journal of Alternative Powertrains*, 5(1):58–67, 2016.
- [157] Yujie Wang, Zhendong Sun, and Zonghai Chen. Energy management strategy for battery/supercapacitor/fuel cell hybrid source vehicles based on finite state machine. *Applied Energy*, 254:113707, 2019.
- [158] Hao Wu, Peter Berg, and Xianguo Li. Steady and unsteady 3d non-isothermal modeling of pem fuel cells with the effect of non-equilibrium phase transfer. *Applied Energy*, 87:2778–2784, 2010.
- [159] Peng Wu, Julius Partridge, and Richard Bucknall. Cost-effective reinforcement learning energy management for plug-in hybrid fuel cell and battery ships. *Applied Energy*, 275:115258, 2020.
- [160] Duo Xiao and Qiuting Wang. The research of energy management strategy for fuel cell hybrid vehicle. In *2012 International Conference on Industrial Control and Electronics Engineering*, 2012.
- [161] Rui Xiong, Hongwen He, Fengchun Sun, and Kai Zhao. Evaluation on state of charge estimation of batteries with adaptive extended kalman filter by experiment approach. *IEEE Transactions on Vehicular Technology*, 62(1):108–117, 2013.
- [162] Qiangu Yan, Hossein Toghiani, and Heath Causey. Steady state and dynamic performance of proton exchange membrane fuel cells (pemfcs) under various operating conditions and load changes. *Journal of Power Sources*, 161(1):492–502, 2006.
- [163] Mingyao Yao, Bo Zhu, and Nong Zhang. Adaptive real-time optimal control for energy management strategy of extended range electric vehicle. *Energy Conversion and Management*, 234:113874, 2021.
- [164] Serhat Yesilyurt, Jason B. Siegel, and Anna G. Stefanopoulou. Modeling and experiments of voltage transients of polymer electrolyte membrane fuel cells with the dead-ended anode. *J. Electrochem. En. Conv. Stor*, 9(2):1–7, 2012.
- [165] Murat Yilmaz and Philip T. Krein. Review of battery charger topologies, charging power levels, and infrastructure for plug-in electric and hybrid vehicles. *IEEE Transactions on Power Electronics*, 28(5):2151–2169, 2013.
- [166] Toshihiko Yoshida and Koichi Kojima. Toyota mirai fuel cell vehicle and progress toward a future hydrogen society. *The Electrochemical Society Interface*, 24(2):44–49, 2015.

- [167] Meiling Yue, Samir Jemei, Rafael Gouriveau, and Nouredine Zerhouni. Review on health-conscious energy management strategies for fuel cell hybrid electric vehicles: Degradation models and strategies. *International Journal of Hydrogen Energy*, 44(13):6844–6861, 2019.
- [168] Bo Zhang, Fei Lin, Caizhi Zhang, Ruiyue Liao, and Ya-Xiong Wang. Design and implementation of model predictive control for an open-cathode fuel cell thermal management system. *Renewable Energy*, 154:1014–1024, 2020.
- [169] Caiping Zhang, Le Yi Wang, Xue Li, Wen Chen, George G. Yin, and Jiuchun Jiang. Robust and adaptive estimation of state of charge for lithium-ion batteries. *IEEE Transactions on Industrial Electronics*, 62(8):4948–4957, 2015.
- [170] Guangsheng Zhang and Satish G. Kandlikar. A critical review of cooling techniques in proton exchange membrane fuel cell stacks. *International Journal of Hydrogen Energy*, 37:2412–2429, 2012.
- [171] Rui Zhang, Yuxiang 2021and Ma, Dongdong Zhao, Yigeng Huangfu, and Weiguo Liu. A novel energy management strategy based on dual reward function q-learning for fuel cell hybrid electric vehicle. *IEEE Transactions on Industrial Electronics*, pages 1–1, 2021.
- [172] Wenbin Zhang, Jianqiu Li, Liangfei Xu, and Minggao Ouyang. Optimization for a fuel cell/battery/capacity tram with equivalent consumption minimization strategy. *Energy Conversion and Management*, 134:59–69, 2017.
- [173] Chen-Hong Zheng and Wei-Song Lin. Self-optimizing energy management strategy for fuel-cell/ultracapacitor hybrid vehicles. In *2013 International Conference on Connected Vehicles and Expo (ICCVVE)*, 2013.
- [174] Chunhua Zheng, C.E.Oh, Yeongil Park, and Suk Won Cha. Fuel economy evaluation of fuel cell hybrid vehicles based on equivalent fuel consumption. *International Journal of Hydrogen Energy*, 37(2):1790–1796, 2012.
- [175] Chunhua Zheng and Suk Won Cha. Real-time application of pontryagin’s minimum principle to fuel cell hybrid buses based on driving characteristics of buses. *International Journal of Precision Engineering and Manufacturing-Green Technology*, 4(2):199–209, 2017.
- [176] Chunhua Zheng, Suk Won Cha, Yeong il Park, Won Sik Lim, and Guoqing Xu. Pmp-based power management strategy of fuel cell hybrid vehicles considering multi-objective optimization. *International Journal of Precision Engineering and Manufacturing*, 14(5):845–853, 2013.
- [177] Wei Zhou, Lin Yang, Yishan Cai, and Tianxing Ying. Dynamic programming for new energy vehicles based on their work modes part ii: Fuel cell electric vehicles. *Journal of Power Sources*, 407:92–104, 2018.
- [178] Ghassan Zubi, Rodolfo Dufo-López, Monica Carvalho, and Guzay Pasaoglu. The lithium-ion battery: State of the art and future perspectives. *Renewable and Sustainable Energy Reviews*, 89:292–308, 2018.